Pentaquark Search in the Strange Sector at ALICE at the LHC

by
Jacob L. Martinez

A dissertation submitted to the Department of Physics,
College of Natural Sciences and Mathematics
in partial fulfillment of the requirements for the degree of

Doctor of Philosophy
in Physics

Committee Chair: Rene Bellwied
Committee Member: Claudia Ratti
Committee Member: Andrew Renshaw
Committee Member: Greg Morrison
Committee Member: Eric Bittner

University of Houston
August 2022

DEDICATION

To my wife and my children.

ACKNOWLEDGMENTS

First and foremost, I would love to thank my wife, Elya Franciscus, for the crazy amounts of support and love she has shown me throughout this long process and for giving us two beautiful children, Elliott and Desmond. There is nothing I can do to repay you.

I would like to thank Dr. Rene Bellwied for allowing me the opportunity to pursue my educational goals by joining his research group, showing me other-worldly patience, and giving me an incredible outlet to learn. I would also like to thank Dr. Anders Knospe who has answered more of my questions than anyone else in the world. This research is Dr. Bellwied's and Dr. Knospe's more than it is mine. I am very appreciative of all their guidance and help.

Thank you to my father and mother, Hector Martinez and Lisa Dennehy, as well as Robin Martinez and John Dennehy. Thank you to my brothers Josh and Matt for always being people I can rely on for anything. Thank you to Kenneth Franciscus for allowing me to explain my research to you, hopefully in an exciting way.

Thank you to the University of Houston for allowing me to return home to a wonderful school experience. I would also like to thank my committee for helping me along the way throughout my entire graduate school tenure. Thank you to my graduate school colleagues Frank Malatino, Eric Hoffman, Fernando Flor, and Sean Roubion for making sure I got enough help to pass every class and for letting me win almost every bowling game. To my office mates Oveis Sheibani and Negin Alizadeh for the wonderful conversations that keep work fun. Everyone in the ALICE/STAR research group has helped me in one way or another, so thank you.

Thank you to CERN and the ALICE collaboration. To the ALICE members that helped me fix all my mistakes and become a better scientist, Alberto Caliva, Anthony Timmins, Ryan Hannigan, Michael Weber, Maximiliano Puccio, Bong-Hwi Lim, and Neelima Agrawal. Thank you all for answering my questions at all hours of the day and making sure my data is run properly.

Thank you to all of my great friends who have supported me throughout the years, Vit Benton, Jeff Gomez, Nate Auchinleck, Max Goldstein, Dave Hernandez, and Justin Graffeo, for all the fun times skating and partying near gas stations off of Atlantic Ave at 2 in the morning.

I would also like to extend a special thank you to Dr. Korey Sorge from Florida Atlantic University for inspiring me to go to grad school. Without your support, I would not have even thought going to grad school would be a possibility. I am forever grateful.

ABSTRACT

The primary objective of the Large Hadron Collider (LHC) in Geneva, Switzerland is to collide nuclear matter to study its properties under extreme conditions. The LHC has been the leading facility in high energy physics with major discoveries, such as the Higgs boson and assisting with discovering the Quark Gluon Plasma (QGP), which is an extremely hot, dense soup of free quarks and gluons. The transition from the QGP phase to the hadronic phase sees free quarks and gluons transition into bound states of quarks and gluons. The typical hadron formation is to a $q\bar{q}$ meson state or to a qqq baryon state.

Multiquark states with more than three quarks had not been confirmed until 2015, when LHCb announced the discovery of several hidden charm pentaquarks $\mathrm{P_c}(4312)^+, \mathrm{P_c}(4440)^+$, and $\mathrm{P_c}(4457)^+$. These hidden-charm pentaquark states were observed as a peak in the $J/\psi p$ invariant mass spectrum. This discovery has reopened the question of whether any pentaquarks are able to exist in the strange sector. Past searches for pentaquarks with strangeness have yielded results that have not been replicated or resulted in no new states at all. Strangeness enhancement, measured by ALICE as a function of increasing charged particle multiplicity even in pp collisions, further adds to the likelihood of observing a strange pentaquark state. Following analogous decay channels for the $\mathrm{P_c^+}$ states into the strange sector, results for $\mathrm{P_s} \rightarrow \phi\mathrm{p}$, $\mathrm{P_s} \rightarrow \Lambda\mathrm{K}$, $\mathrm{P_s} \rightarrow \Lambda\mathrm{K}^*$, and $\mathrm{P_s} \rightarrow \Sigma^*\mathrm{K}$ through invariant mass analysis in minimum bias pp collisions at $\sqrt{\mathrm{s}} = 13$ TeV at ALICE are presented.

No pentaquark signal is observed for any decay channels in this analysis. Thermal model predictions for the yield of the P_s are obtained and compared to upper limit calculations produced from the ALICE data. Significant upper limits are set for the P_s for most of the decay channels that were analyzed.

TABLE OF CONTENTS

LIST OF TABLES

LIST OF FIGURES

1 Introduction

How is it that you have come to arrive here? How is it that the particles that make up your body were formed? The formation of nuclear matter can be traced back to the early stages of our universe, one microsecond after the Big Bang. At this point the universe is thought to have been in a state called a Quark-Gluon Plasma (QGP), which is a state of matter characterized by such extreme temperatures and pressures that quarks and gluons are asymptotically free. The expansion and cooling of the QGP has allowed the free quarks and gluons to form nuclear matter that can still be seen to this day. A sketch of the evolution of the universe can be seen in Figure 1.1

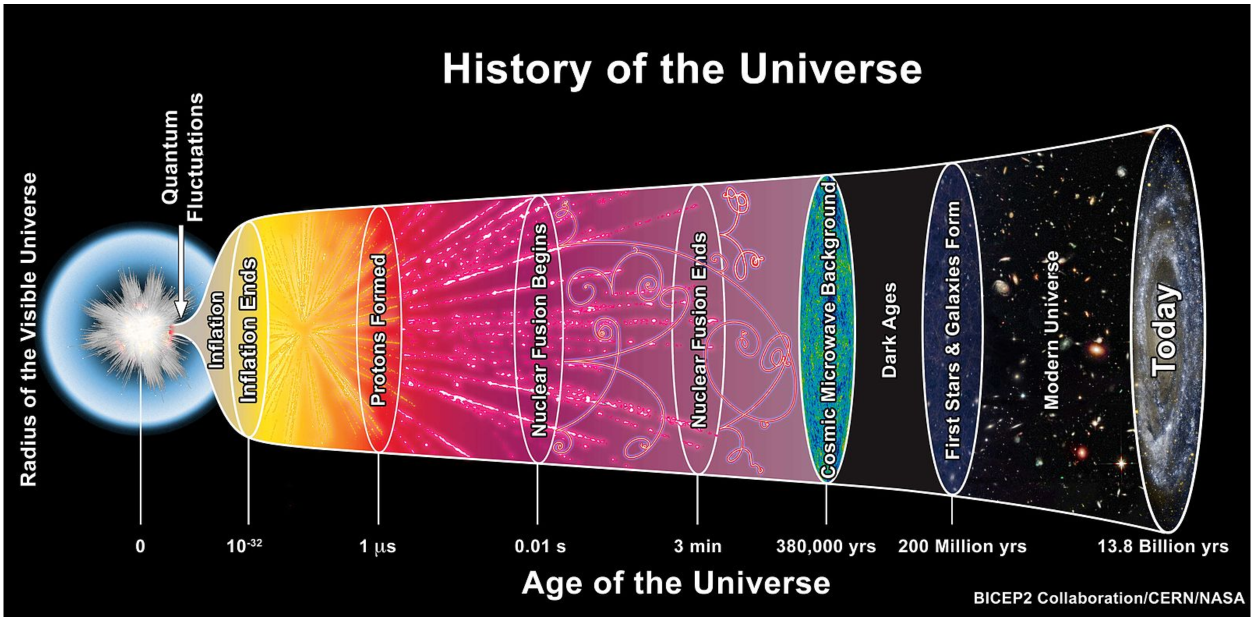

Figure 1.1: Time evolution of the universe after the Big Bang. The first protons formed from the quark-gluon plasma at 1 microsecond (μs) after the Big Bang [2].

1.1 The Standard Model of Particle Physics

The Standard Model of particle physics is a theory that classifies all known elementary particles and describes their behavior through three fundamental forces: electromagnetic, strong, and weak [3].

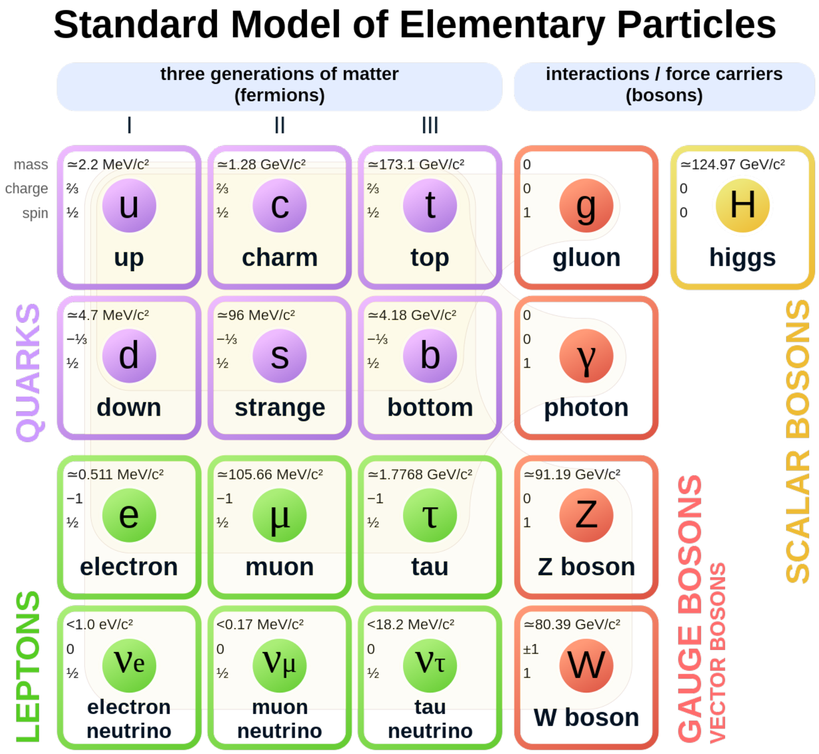

Figure 1.2: The elementary particles of the standard model [4].

The Standard Model lists six quarks and six leptons. The six quark flavors are: up (u), down (d), strange (s), charm (c), bottom (b), and top (t). Alternately, bottom and top may be referred to as beauty and truth, respectively. Leptons are divided into three generations: electron (e) and electron neutrino (ν_e), muon (μ) and muon neutrino (ν_μ), and tau (τ) and tau neutrino (ν_τ) [3].

Each fundamental force is mediated via an exchange of force carriers referred to as *gauge bosons*. The photon (γ) mediates the electromagnetic, EM, force between electrically charged particles. The $\mathrm{W}^{\pm}$ and Z bosons mediate the weak force and are involved in nuclear decays due to the ability to change the flavor of both quarks and leptons. The gluon (g) mediates the strong interaction which binds quarks and gluons with color charge into composite particles called *hadrons*. Finally, the Higgs boson (H) is responsible for explaining why all massive particles have mass (inertia) by interaction with a scalar Higgs field that permeates the entire Universe. A chart depicting the elementary particles and some of their characteristics can be seen in Figure 1.2.

1.2 Quantum Chromodynamics

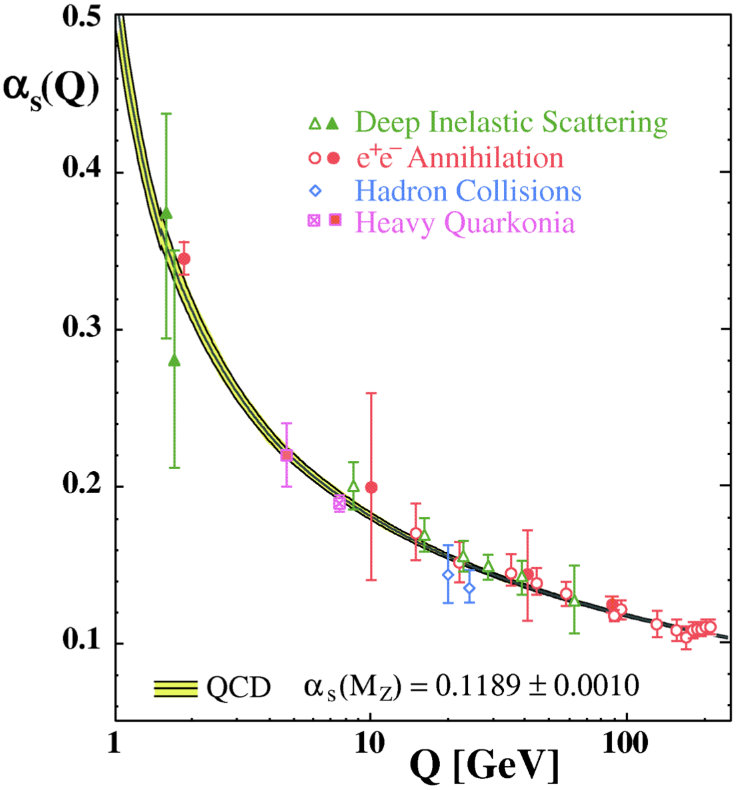

Figure 1.3: Summary of measurements of α_S(Q) as a function of momentum transfer Q. Open symbols indicate NLO and filled symbols indicate NNLO QCD calculations used in respective analyses. The curves are the QCD predictions [7].

Quantum Chromodynamics (QCD) is the theory that describes interactions between quarks and gluons via the strong force. Quarks and gluons are the fundamental particles that make up composite *hadrons* such as pions, protons, neutrons, kaons, etc. QCD is based on a non-abelian SU(3) gauge theory. Similar to electric charge, QCD has an analogous *color* charge. Color charge consists of red, green, blue, and their "anti" colors (anti-red, anti-green, anti-blue). It should be noted that these “colors” have no connection to the colors of the electromagnetic spectrum, they are just a convenient label. The force carriers for QCD are the gluons, just like the force carries for quantum electrodynamics (QED) are the photons. The six different flavors of quarks are spin 1/2 fermions and the eight massless, flavorless, colorful gluons (bosons) have spin 1. QCD is characterized by two main features, which are color confinement and asymptotic freedom [7]. Both of these features are characterized by the QCD coupling constant, α_S, which is approximated as:

$$\alpha_S \approx \frac{12\pi}{(11\mathrm{n} - 12f)\ln(|\mathrm{Q}^2|/\Lambda^2)} \tag{1}$$

where n is the number of colors, f is the number of flavors, Q^2 is the amount of momentum transferred and Λ is the QCD scale parameter that can range from 100 MeV to 500 MeV. Figure 1.3 shows experimental results of how the value of α_S changes with Q^2 and its comparison with results from perturbative QCD.

A single quark has never been confirmed to be isolated by any experiment. The absence of this observation suggests that interactions between quarks and gluons must be very strong on large distance scales. This phenomenon is what is called color confinement; particles that have a color charge are bound in color neutral states. In the opposite regime, the interaction strength between quarks and gluons becomes arbitrarily small when the distance between the particles becomes short. This phenomenon is known as asymptotic freedom.

1.3 Quark Gluon Plasma

The aim of the Large Hadron Collider (LHC) is to accelerate nuclei to nearly the speed of light, c, and have them collide with one another. This collision causes the nuclei to explode in a “fireball” that recreates the conditions of the early universe just after the Big Bang. This fireball results in a state of matter where the constituent quarks and gluons that make up the protons and neutrons in the nuclei are temporarily free from the hadrons in which they are normally bound.

As shown in Figure 1.4, the QCD phase diagram, matter that strongly interacts can experience

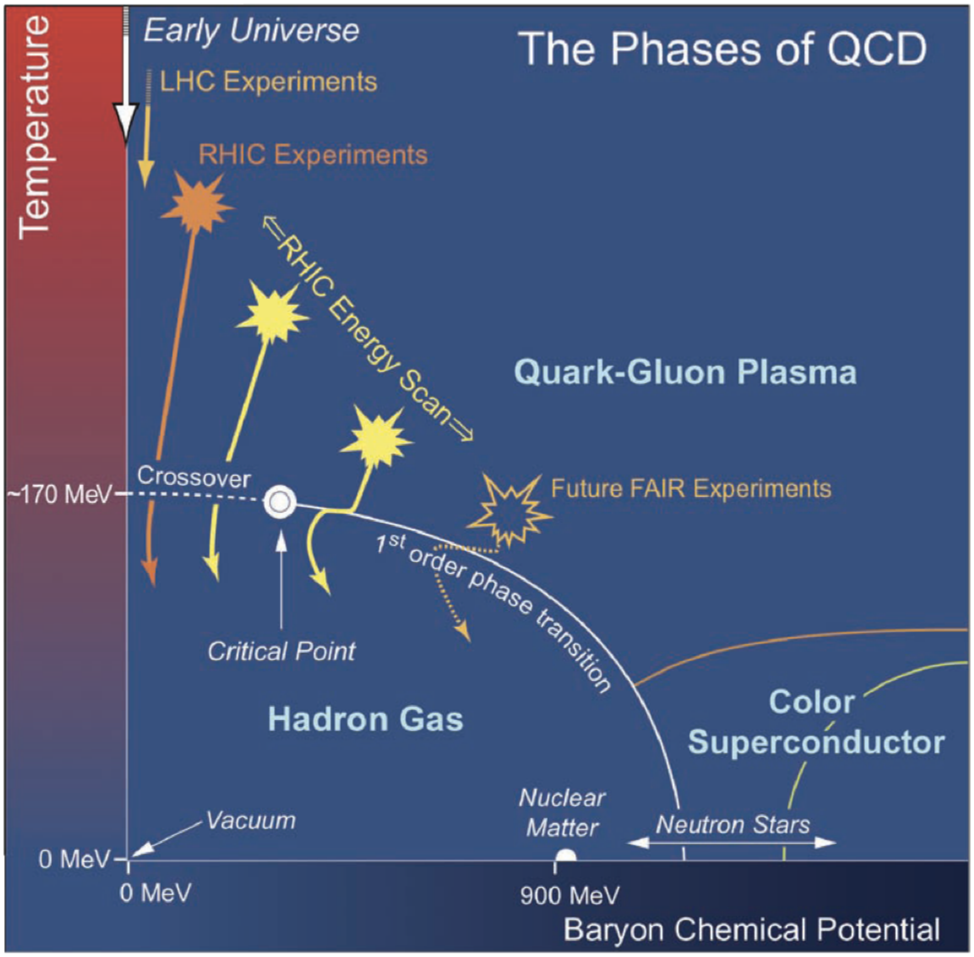

Figure 1.4: QCD Phase Diagram [6].

a phase transition from hadron gas to a QGP. Experiments such as ALICE at the LHC are high energy collision experiments, which means they are able to reach higher temperatures with very low baryon chemical potentials ($\sim$ 0 MeV). A QGP has been formed in heavy-ion collisions at the LHC and at the Relativistic Heavy Ion Collider (RHIC) at Brookhaven National Laboratory. Although RHIC experiments are also collider experiments, they have much lower collision energies than LHC experiments, which leads to partial stopping of colliding nuclei. This stopping increases the baryon chemical potential, and the lower energies lower the temperature as compared to LHC experiments.

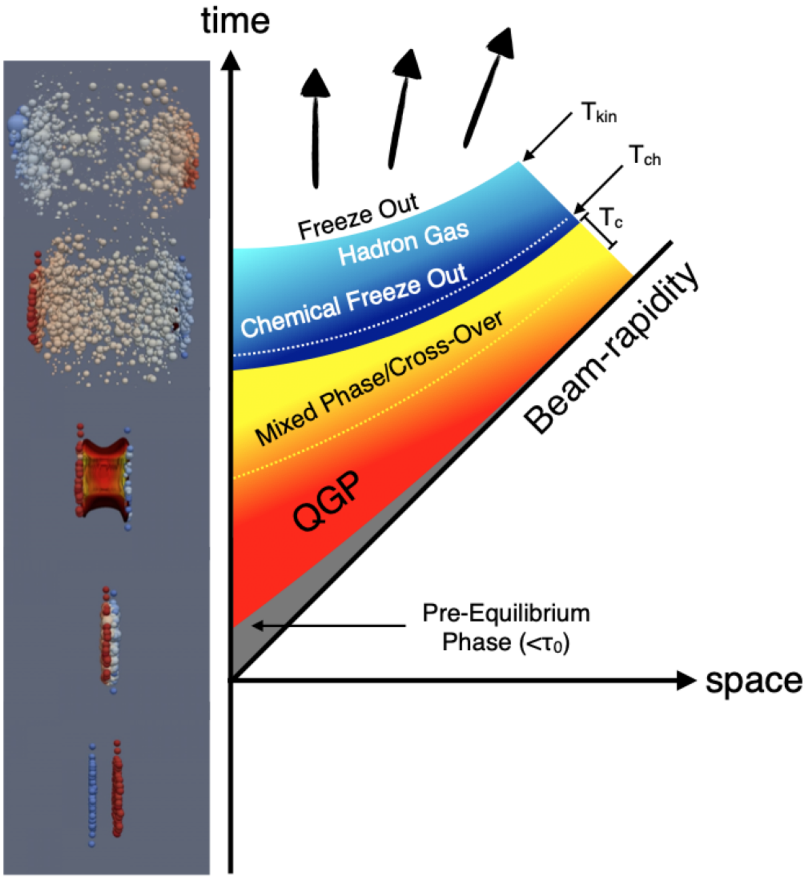

Figure 1.5: Time Evolution of a heavy ion collision [5].

As shown in Figure 1.5, the heavy nuclei involved in the collisions are accelerated to such high speeds that their normally spherical shapes appear to be flat disks just before the collision due to Lorentz contraction. Shortly after the collision, before 1 fm/c, quarks and gluons are produced in a quasi-free de-confined state system known as the pre-equilibrium stage. Quarks that are normally confined into two or three quark hadrons in order to remain color neutral are now free to interact with other quarks and gluons in this de-confined system. This system reaches equilibrium between quarks and gluons around 1 fm/c.

The QGP system continues to expand and reduce its temperature through elastic and inelastic collisions during the expansion stage from $1 < \tau < 10$ fm/c. As the QGP expands it also cools until it reaches a critical temperature, T_c. This occurs due to the internal pressure that is built up in the QGP from the shockwave caused by two heavy ions colliding. This is when the QGP will begin to hadronize, the point at which no more "free" quarks can remain so the quarks and gluons form hadrons. The chemical freeze-out temperature, $\mathrm{T}_{ch} \approx 155$ MeV, occurs during the mixed-phase/cross-over phase when the number of hadrons is fixed, inelastic collisions cease and relative particle abundances do not change[6]. After chemical freeze-out, elastic collisions continue to occur which can change a particle's momentum, but do not generate any new particles. Kinetic freeze-out, $T_{kin} \approx 100$ MeV, which occurs around 15 fm/c, happens when elastic collisions cease and the system has reached a point that the kinematic distributions of hadron species has been fixed. These particles are now free to be measured by ALICE or any other detector.

1.4 Resonant States

A resonance is an extremely short lived particle that has the exact same quark content as a stable ground state particle, but has different angular momentum and/or parity. Resonances decay strongly, which means that they conserve quantum numbers, including quark content, across their decay channels. Resonances typically have lifetimes on the order of just a few fm/c, which is comparable to the lifetime of the fireball created in a heavy-ion collision and makes them ideal to study the QGP [8]. Because of their short lifetimes, they can not be observed directly and must be observed by reconstruction of their decay daughters.

Resonances are not characterized by a Gaussian mass distribution that is typical of ground state particles. Resonances can be described by the Breit-Wigner formula:

$$f(E) \propto \frac{1}{(E-M)^2 + \Gamma^2/4} \tag{2}$$

where $f(E)$ is the probability density formula, M is the resonance mass, and Γ is the full-width half-max (FWHM). The FWHM is very important for determining the distribution around the peak resonance mass and is related to the lifetime of the particle by the equation:

$$\Gamma = \frac{\hbar}{\tau} \tag{3}$$

where $\hbar$ is the reduced Planck's constant and τ is the lifetime of the resonance particle. The FWHM represents the range of the Breit-Wigner distribution when the distribution has decreased to half of its peak value. Eq. 3 is very closely related to the Heisenberg uncertainty relation for energy and time:

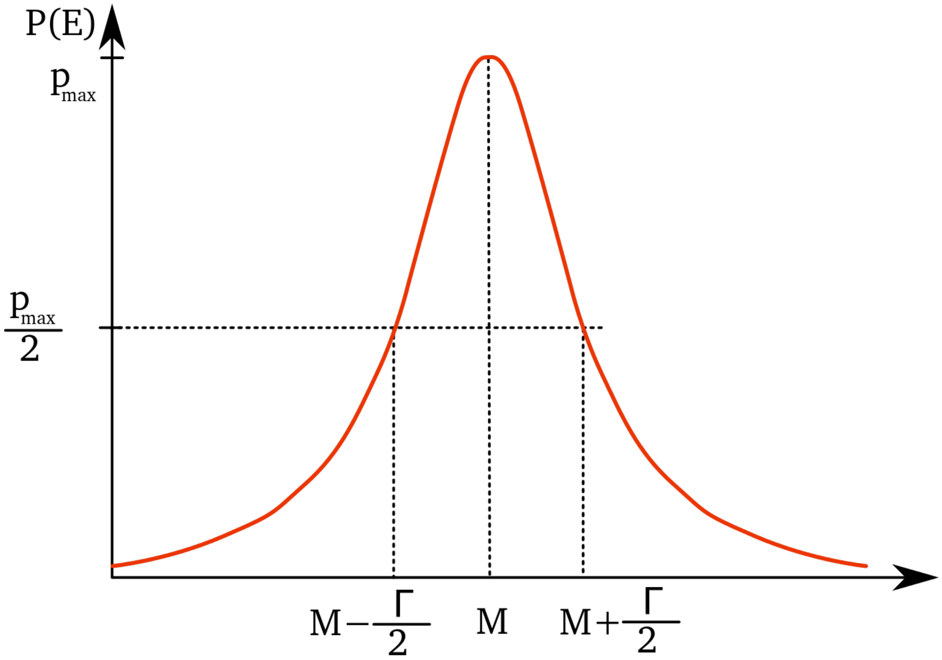

Figure 1.6: Breit-Wigner Distribution. The mean is shown as the mass of the resonance and Γ is shown as the full-width half-max (FWHM) [9].

$$\Delta E \Delta T \geq \hbar/2 \tag{4}$$

where ΔE is the uncertainty in energy and ΔT is the uncertainty in time. The uncertainty in energy can be thought of as being related to the FWHM ($\Delta E \approx \Gamma$) just as the uncertainty in time can be related to the lifetime of the resonance ($\Delta T \approx \tau$).

The characteristic of resonances that makes them ideal for studying the QGP is the fact that they have lifetimes on the order of 10^{-23} seconds. However, not all resonance have exactly the same lifetime. The resonance $\phi(1020)$ has a relatively long lifetime ($c\tau = 46$ fm/c) compared to the lifetime of the "fireball" created in a heavy-ion collision [38]. Other resonances, such as the $\mathrm{K}(892)^{\pm}$, have very short lifetimes ($c\tau = 4$ fm/c) so that they should almost completely decay inside the fireball [38]. The fact that different resonances decay with different lifetimes makes it possible to study the different temperatures of the QGP as it expands and cools by studying the resonances that decay in the same time frame that the system would be in for a given temperature. Certain resonances may be ideal for studying the chemical freeze-out temperature while other resonances may be better suited to study the kinetic freeze-out temperature. Thus, resonances constrain the hadronic lifetime of the system, such as the time between chemical and kinetic freeze-out.

1.5 Hadronic Matter

As mentioned previously, quarks and gluons interact strongly to form bound states in a hadronic gas phase. How these quarks and gluons arrange themselves when they hadronize is part of the aim of this dissertation. One of the driving factors that determines which combination of quarks can form a bound state is the color charge. According to QCD, composite particles found in nature must be color neutral, which means that either all three color charges must be present (red, green and blue), or that a color and its anti-color must be present. As an example, the proton has quark content uud. Each of the quarks has a different color charge, making the entire proton color neutral. Another example is the pion^{+}, π^{+}, which has quark content $\mathrm{u\bar{d}}$. The u quark has a color charge and the anti-down quark has the anti-color charge of the u quark, making it color neutral. Both of these types of particles are seen in nature and are very abundant.

When three quarks form a hadron, their individual color charges are all different. A three quark state is called a *baryon*, while a two quark state with one quark and one anti-quark is called a *meson*. A schematic of these particles can be seen in section a on Figure 1.7. Section b of Figure 1.7 shows states that have *not* been observed in nature, diquarks. The difference between diquarks

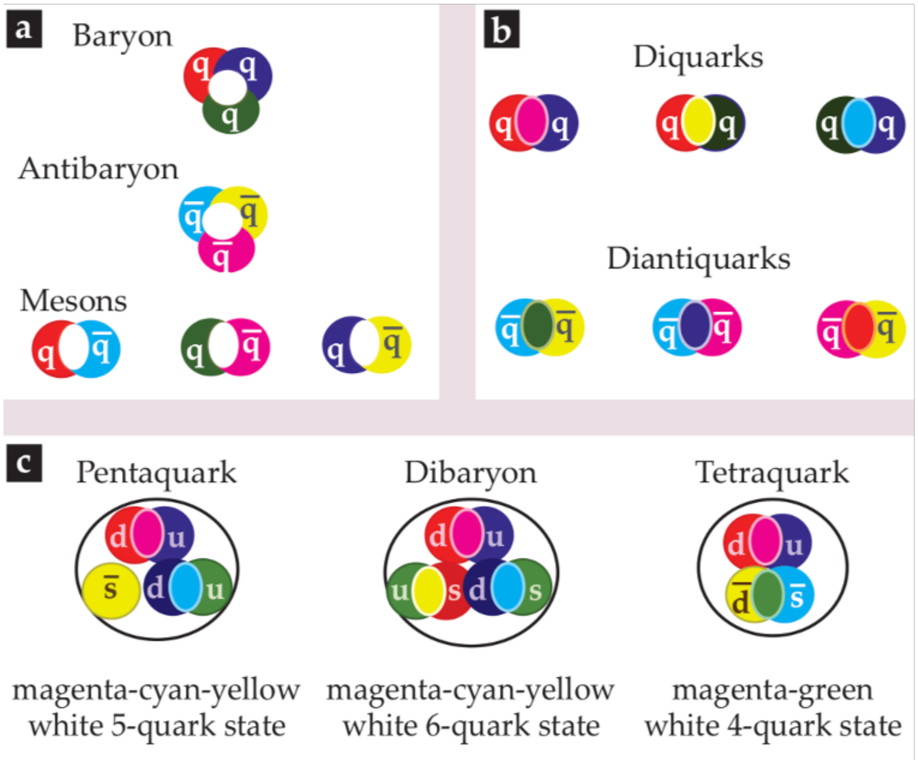

Figure 1.7: Conventional and Exotic quark combinations. (a) Three differently colored (anti)quarks form (anti)baryons. Quarks couple with anti-quarks of the corresponding anti-color to form mesons. (b) Two quarks combine to for an anti-colored diquark. (c) Any number of quarks and anti-quarks can combine as long as the state is colorless. Examples of a four, five, and six quark state are shown. [10].

and mesons is that diquarks do not contain and anti-quark, but contain two quarks. There is no combination of two quarks that would result in a color neutral particle (as shown in the overlap region in Figure 1.7), so this configuration is forbidden. It should also be noted that electric charge for each of these states needs to be an integer value. Any combination with non integer values for electric charge would also be forbidden.

Possible new states that are generally allowed are shown in section c of Figure 1.7. Baryons and mesons are seen in great abundance in nature, with many different combinations of quarks and anti-quarks. However, states with more than three quarks seem to be much less available. Theoretical predictions of four quark states (tetraquarks)[11], five quark states (pentaquarks)[12], and six quark states (hexaquarks/dibaryons)[13] have been around for decades. It stands to reason that, if two quarks can form a colorless bound state, then any even number of quarks can also form a colorless bound state. Similarly, the combination of a colorless baryon (three quarks) combined with any number combination of colorless mesons (two quarks) can lead to any odd number of quarks in a bound state. These states with more than three quarks would be considered "exotic" in the quark model, but are not necessarily forbidden by QCD. In 2003, the first tetraquark candidate was discovered [14] though not confirmed. Newer results from LHCb have confirmed tetraquark [15] and pentaquark [44] states, all containing at least one charm quark. No dibaryon states have been confirmed yet by any experiment.

During these heavy-ion collisions, many hadrons and resonances are produced. There are many different approaches to help describe the yields of the produced particles. The statistical hadronization model has been very successful in explaining yields of light hadrons in heavy-ion collisions. The number, N, of a given hadron species, h, produced in a collision is given by:

$$N_h^{stat} \approx \gamma_h g_h V_H \left(\frac{m_h T_H}{2\pi}\right)^{3/2} e^{-m_h/T_H} \tag{5}$$

where γ_h is the fugacity, g_h is the degeneracy of the hadron, V_H and T_H are the volume and temperature, respectively, of the source for the statistical production of the hadrons, and m_h is the mass of the hadron species [16][17]. For a light hadron at LHC energies, $\gamma_h = 1$.

Based on Eq. 5, it is apparent that the number of produced hadrons of a given species is heavily influenced by the mass of the particles, which scales with $m^{3/2}e^{-m/T_H}$ [18]. As mass increases, the yield of a particular hadron species decreases with a predictable trend as seen in Figure 1.8. The red circles show the data obtained from 0%-10% central Pb-Pb collisions at ALICE at $\sqrt{s_{NN}} = 2.76$ TeV, compared to the blue bars which are the statistical hadronization model combined with feed down decays from higher mass particles. For example, many Λ baryons are produced from the fireball, but more are also produced from the decays of other particles like the electromagnetic decay $\Sigma^0 \to \Lambda\gamma$ and the strong decay of the resonance $\Sigma^{*+} \to \Lambda\pi^+$. Particles with higher mass tend to have a lower feed down contribution than particles with lower mass because they have fewer particles that are heavier that will decay into them. Also, heavier particles are more rare and have a lower yield compared to lower mass particles, so the chance of being a decay daughter from another higher mass particle decay is less likely. When feed down decays are not taken into account and only primordial particles are accounted for, the dotted blue line is what the statistical hadronization model predicts. The data obtained from ALICE follows the trend very nicely. This predictive capability can act as a guide as to what the yields for exotic light baryons and mesons should be.

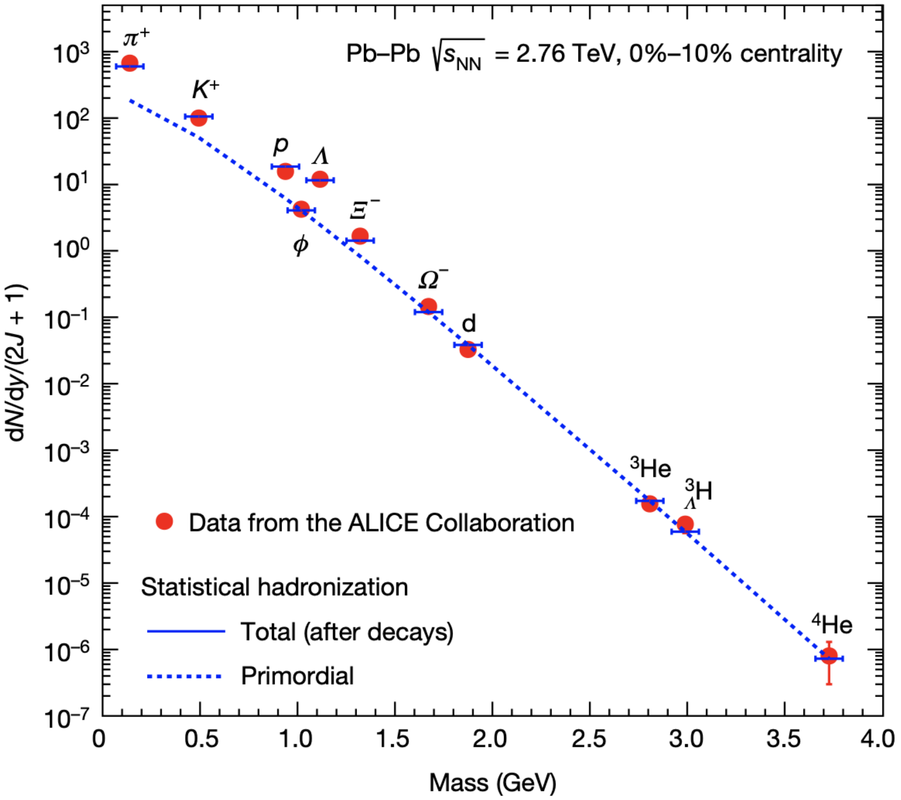

Figure 1.8: Mass dependence of light hadron yields with the predictions from the statistical hadronization model. Data from ALICE is shown as red circles for each particle species (no anti-particles). The 'total' yields are the blue bars, which include feed down from decays of higher mass particles. The primordial yields before strong and EM decays are shown as the dotted line [18].

1.6 Strangeness Enhancement

Production of a quark gluon plasma has been achieved at the Relativistic Heavy Ion Collider (RHIC) at Brookhaven National Laboratory as well as at the Large Hadron Collider (LHC) at CERN. Since this QGP is such short lived, direct detection is not possible so detection must be done by looking for other signatures, such as jet-quenching, J/ψ suppression, direct photons, etc. One particular signature is something known as *strangeness enhancement*.

The strange quark (s) is a second generation quark and is only present in the original nuclear matter before the collision in sea quarks and in very negligible numbers. After a collision, there are many particles produced that contain one or multiple strange quarks. The vast majority of this strangeness is produced by the collision. The small mass of the strange quark, which is close to the temperature of the QGP transition, allows for the thermal production of strange and anti-strange quarks through gluon pair annihilation in the QGP. The fast rate of thermalization is due to the abundant presence of gluonic excitations. When compared to a hadron gas phase, the QGP formation would lead to an overall enhancement of multi-strange hadrons as compared to non-strange hadrons. This strangeness enhancement was first proposed as a signature for the QGP in the 1980's by Rafelski and Muller [19].

The enhancement of multi-strange baryons was first observed in heavy ion collisions from the NA57 experiment at the Super Proton Synchrotron (SPS) ($\sqrt{s_{NN}}$= 13.7 GeV), followed by measurements at RHIC ($\sqrt{s_{NN}}$= 200 GeV), and the LHC ($\sqrt{s_{NN}}$= 2.76 TeV). Fig. 1.9 shows results from each experiment, displaying the yield of Ξ^- (with quark content dss) and Ω^- (with quark content sss) normalized by the mean number of nucleon participants in the collision, $\langle N_{part} \rangle$, relative to pp/p-Be as a function of $\langle N_{part} \rangle$ [20]. The increase of the production rate of multi-strange baryons is very clearly seen, with up to 20 more Ω per event for the most central events at NA57. Strangeness enhancement is observed by the upward trend of particle yield as a function of $\langle N_{part} \rangle$.

The increase of hyperon production with respect to multiplicity can be understood as the removal of canonical suppression. In smaller systems like pp, quantum number conservation is required, but in larger systems, like A-A, the larger volume allows for a quantum number like

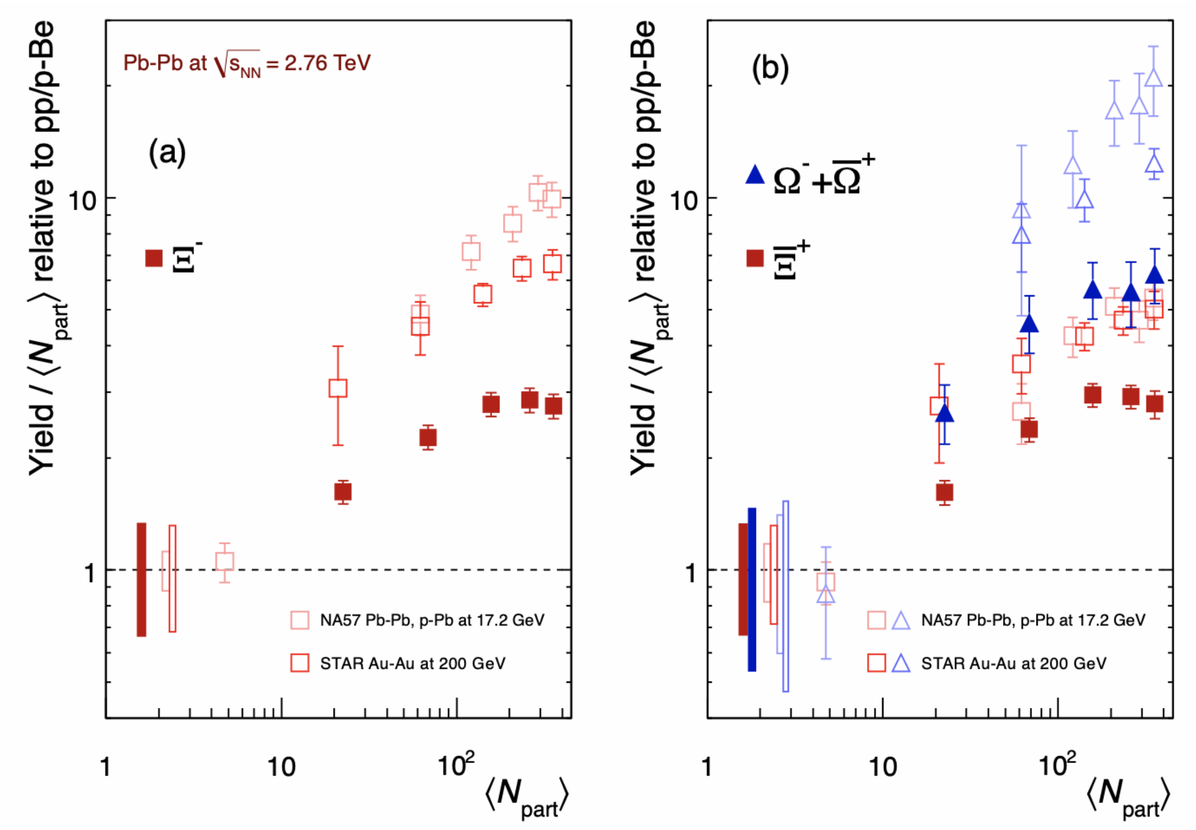

Figure 1.9: Enhancement of multi-strange baryons at mid rapidity ($|y| < 0.5$) as a function of the mean number of nucleon participants in a collision observed at the LHC (ALICE with closed markers), RHIC and SPS (open markers) [20].

strangeness to be implemented on the average by a chemical potential. The quantum number conservation in the smaller system is enforced by working in the canonical ensemble, which leads to a reduction in phase space for particle production. This is known as canonical suppression [21].

The phi meson, ϕ, is a special case in the context of strangeness enhancement and canonical suppression. Its quark content is one strange quark and one anti-strange quark, ($s\bar{s}$), which means it has no net strangeness and no net charge. The ϕ containing a strange quark but having no net strangeness is known as *hidden strangeness*. This means it should not be subject to the canonical suppression mechanism. But, the ϕ meson yield should increase with multiplicity through the strangeness enhancement mechanism. Being that the ϕ meson requires the production of two strangeness carrying strings to form a strange quark and a strange anti-quark, the expected enhancement should be similar to other particles with two strange quarks, namely the Ξ.

Fig. 1.10 shows the yields of certain particle species normalized by the yields of charged pions as a function of charged particle multiplicity [46]. From top to bottom, the particles and their quarks contents are: proton (uud), K_S^0 ($d\bar{s}$), Lambda (uds), phi ($s\bar{s}$), Xi (dss), Omega (sss) [38].

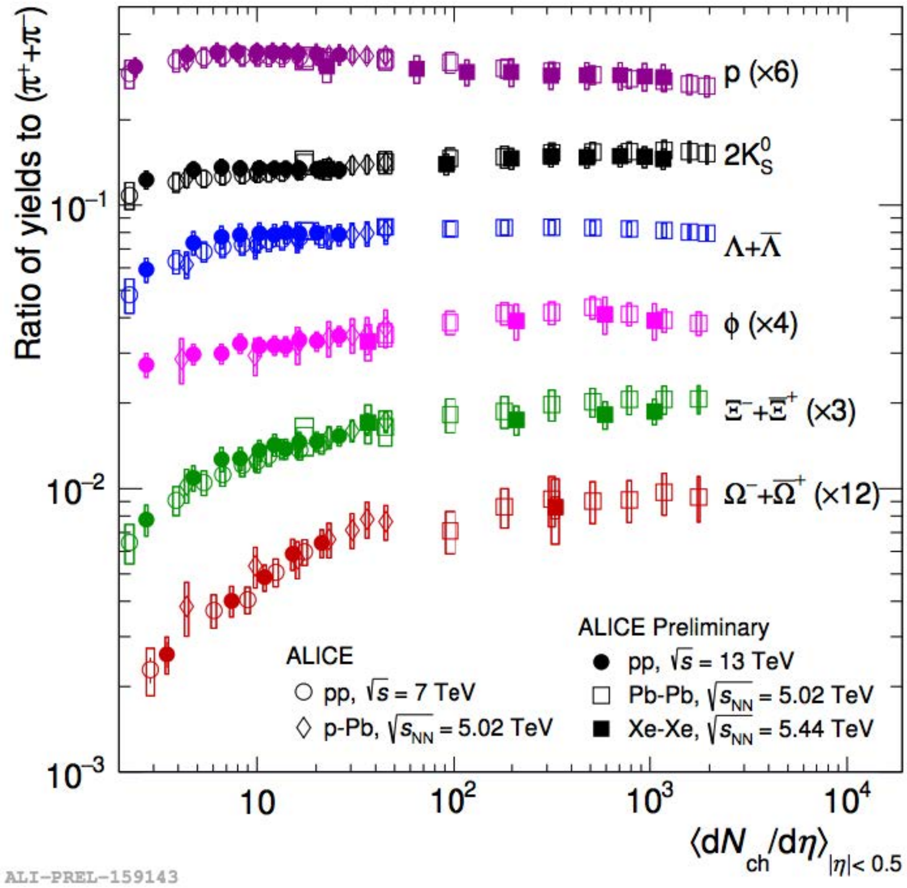

Figure 1.10: Yield ratios of hadron/$(\pi^+ + \pi^-)$ at different collisions energies and system sizes. The ratio of hadrons that contain at least one strange quark to pions increases as a function of $\langle dN_{ch}/d\eta \rangle$ at $|\eta| < 0.5$ [46].

Fig. 1.10 shows that a significant enhancement of strange to non-strange hadron production is observed with increasing charged particle multiplicity. This enhancement is observed for pp and p-Pb. The higher the strangeness content of a particle species, the stronger an enhancement that is observed. This effect seems to be due to enhancement and not due to the mass of the hadron. The ϕ meson, which has net strangeness of zero, shows behavior like a strange baryon with the enhancement somewhere between Λ with net strangeness of 1 and Ξ with net strangeness of 2. Strangeness enhancement will be discussed again in 3.3.

2 The ALICE Experiment at the Large Hadron Collider

The Large Hadron Collider (LHC) is the largest and most powerful particle accelerator and collider in the world. It is situated in the CERN accelerator complex, shown in Figure 2.1, on the French-Swiss border near Geneva, Switzerland. The LHC is 27 kilometers in circumference, sits an average depth of 100 meters underground, and houses four main experiments: ALICE, ATLAS, CMS, and LHCb.

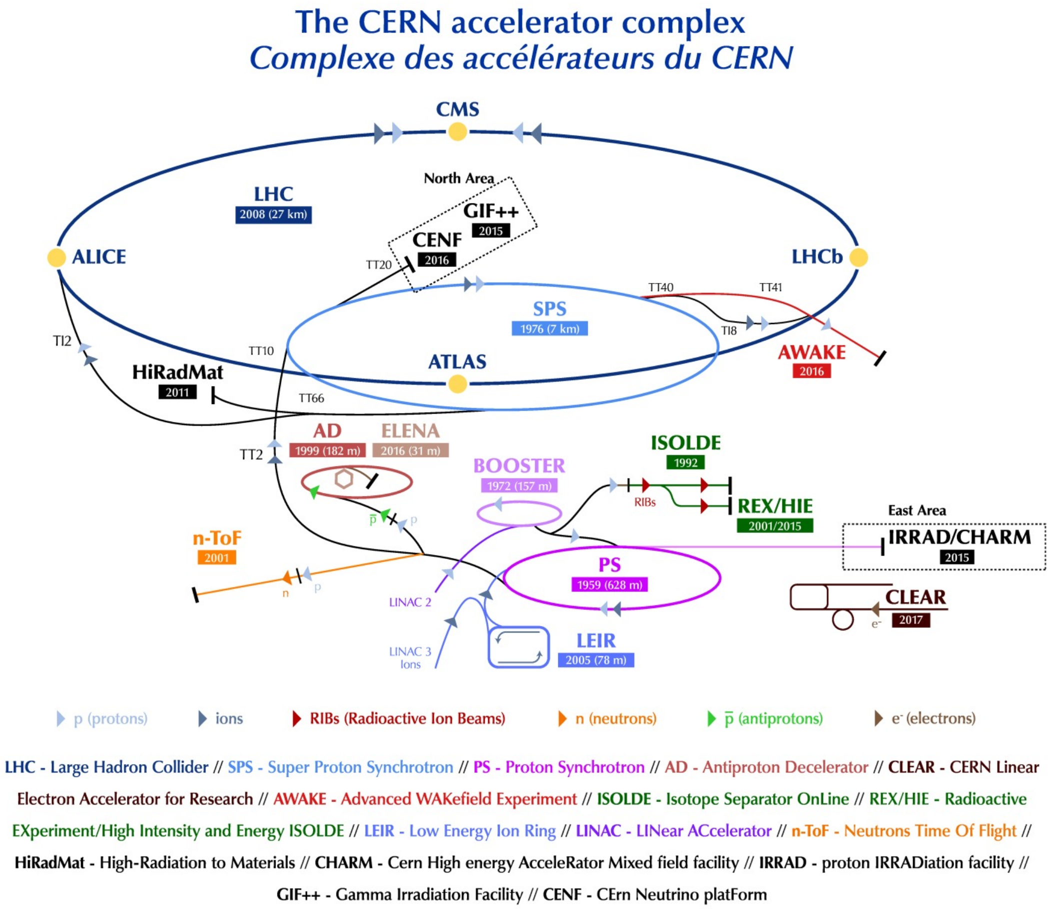

Figure 2.1: CERN accelerator complex

Each experiment has a different experimental setup and is built for different goals. The ATLAS and CMS experiments mainly analyze pp collisions for the detection of the Higgs boson and physics beyond the standard model. The LHCb experiment studies particles containing the b quark in order to investigate the slight difference between matter and antimatter. The main aim of the ALICE experiment is to study strongly interacting matter (QGP) and its phase transition to hadronic matter.

A proton, or heavy-ion, is accelerated to 99.9999991% the speed of light [24]. The center of mass energy, $\sqrt{s}$, is the total energy in a system in the center of mass frame. For two colliding particles, $s = (E_1 + E_2)^2$ which means that when $E_1 = E_2$, then $s = 2E^2$. This dissertation deals with an analysis of pp collisions with $\sqrt{s} = 13$ TeV.

2.1 ALICE Coordinate System

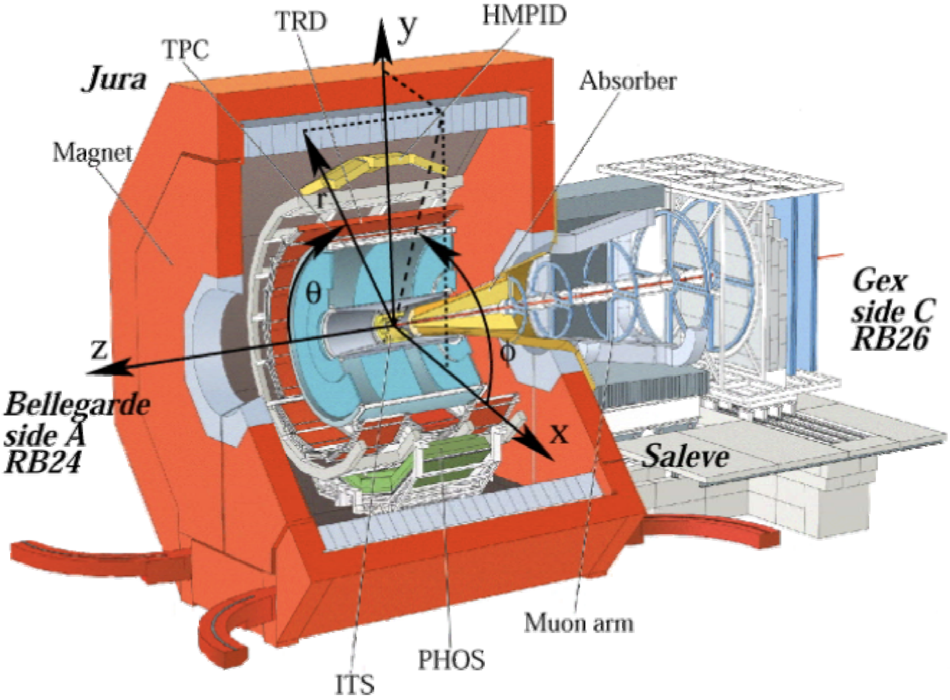

Figure 2.2: The ALICE Coordinate system

In order to have a better assessment of the detectors and data analysis, it is very important that the ALICE coordinate system is understood. The ALICE coordinate system is described in

Figure 2.2. The ALICE coordinate system is a right-handed Cartesian coordinate system with its point of origin (x, y, z) = (0,0,0) at the beams interaction point. The z-axis is defined to be along the beam direction with the $+z$ direction to be from the origin toward side A (ATLAS) and the -z direction points toward side C (CMS). The z-axis direction is known as the longitudinal direction.

The x-axis and y-axis both make up the transverse direction. The x-axis is perpendicular to the z-axis, starts from the origin (x, y, z) = (0,0,0), and points in the positive direction toward the center of the LHC. The -x direction points away from the center of the LHC. The y-axis is perpendicular to both the x-axis and z-axis. The $+y$ direction points upward while the -y direction points downward.

The azimuthal angle, ϕ, is measured with respect to the x-axis in the counter clockwise direction. The main particle identifying detectors at ALICE have an acceptance that covers a full 2π azimuthal angle. The polar angle, θ, is measured from the z-axis toward the x-y plane. The polar angle is related to *pseudorapidity* (η), which will be used throughout this dissertation. Pseudorapidity is defined as:

$$\eta \equiv -\ln\left[\tan\left(\frac{\theta}{2}\right)\right] \tag{6}$$

2.2 A Large Ion Collider Experiment (ALICE)

ALICE [23] is a detector dedicated to measuring and analyzing heavy-ion collisions at the LHC. The primary goal of ALICE is to study strongly interacting matter at extreme temperatures and densities. ALICE is designed to be able to handle the large particle multiplicities from Pb-Pb collisions while also analyzing as many observables associated with the QGP as possible. Its overall dimensions are 16m x 16m x 26m and it weighs approximately 10,000 tons [23]. The collaboration includes nearly 2000 scientists from 174 physics institutes in 40 different countries [25].

There are 18 different detector systems, shown in Figure 2.3, that are optimized to provide excellent particle identification (PID) and momentum resolution over a broad range of momentum.

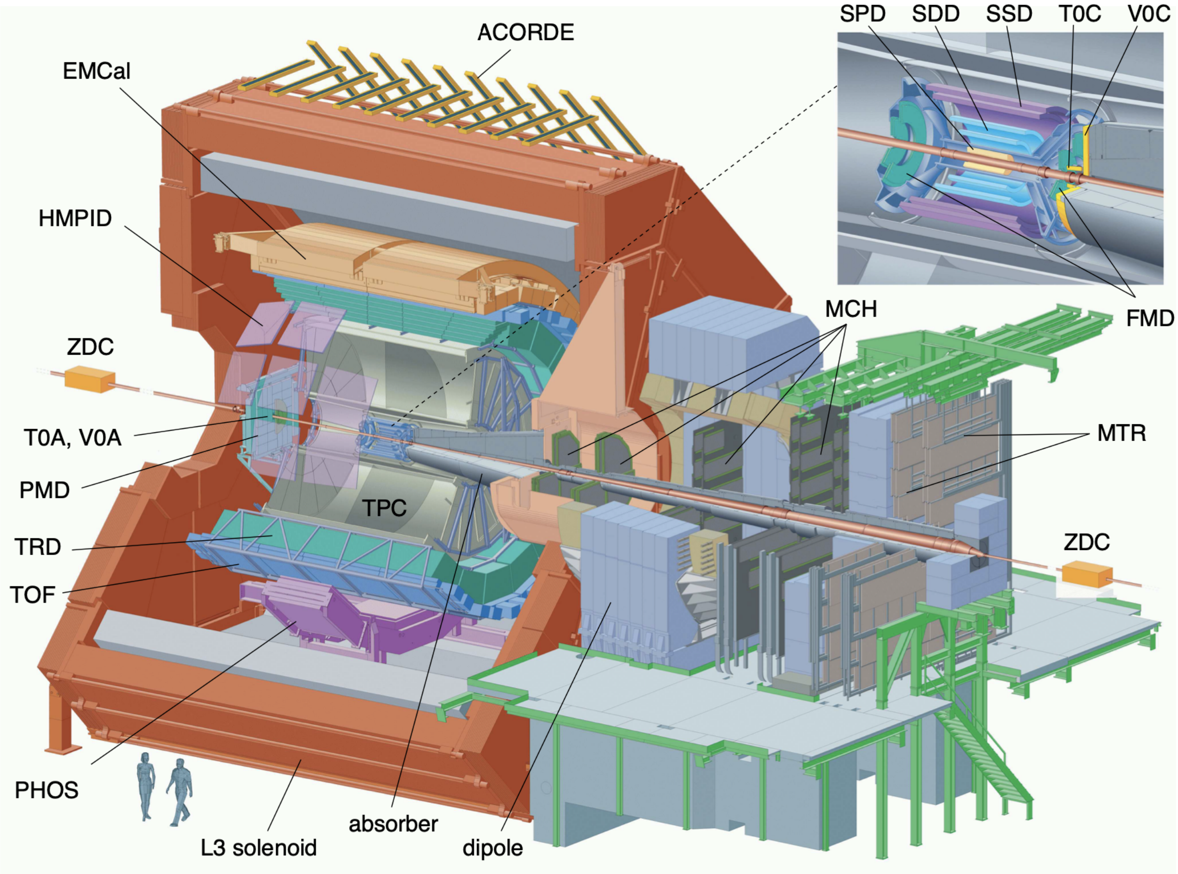

Figure 2.3: The ALICE Experiment. Figure taken from [23]

The detectors can be divided into two main components, the central-barrel and the forward detectors. The central-barrel includes detectors that are contained inside a large solenoid magnet that provides a constant 0.5 T magnetic field parallel to the beam direction (z-direction) and covers a pseudorapidity range of -0.9 $< \eta <$ 0.9.

The primary purposes of the central-barrel detectors are particle identification, tracking, vertexing, and momentum measurement. The innermost detector that is closest to the collision point is the Inner Tracking System (ITS), followed by the Time Projection Chamber (TPC). The ITS and the TPC are mainly dedicated to determining primary and secondary vertices and tracking low momentum particles. The ITS will be discussed in Section 2.3 and the TPC will be discussed in Section 2.4. The next detector is the Transition Radiation Detector (TRD), followed by the

Time of Flight (TOF). The TOF will be discussed in Section 2.5. The next three detectors are the High Momentum Particle Identification Detector (HMPID), Photon Spectrometer (PHOS), and Electromagnetic Calorimeter (EMCal). It should be noted that these outer three detectors (HMPID, PHOS, and EMCal) do not have a full azimuthal coverage like the other detectors in the central-barrel. This is because of spatial restrictions inside the central-barrel or due to budget limitations.

The forward muon spectrometer is located at a forward pseudorapidity of $-4.0 < \eta < -2.5$ and consists of a front absorber for background reduction, 10 tracking chambers (MCH), a dipole magnet, and a triggering chamber (MTR). The muon spectrometer can be seen in Figure 2.3 on the right side of the figure. This system is configured to measure $\mu^+\mu^-$ pairs from decays of light and heavy flavor vector mesons as well as single muon production from other heavy flavor hadron decays [23][26].

Other detectors are placed in areas with pseudorapidities near the beam pipe as well. These forward detectors are used to measure and to trigger on global event characteristics. The Time Zero (T0) measures the start time of events with a precision on the order of tens of picoseconds. The TOF uses the T0 to measure the start time of a collision. The VZERO detectors (VZERO-A and VZERO-C) are used to measure charged particle multiplicities, trigger minimum bias events, and reject background coming from the beam-gas interaction. The Forward Multiplicity Detector (FMD) gives information about the multiplicity of an event, the Photon Mulitplicity Detector (PMD) determines the spatial distribution of photons of an event, and the Zero Degree Calorimeter (ZDC) is used to measure and trigger on the impact parameter by measuring the energy of spectator nucleons in a heavy-ion collision [26].

The TPC and TOF are the main detectors used in this analysis due to their ability to efficiently track and reconstruct charged particles. The ITS will also be discussed for its ability to track and determine vertices. Other detectors such as the T0 and VZERO detectors will also be discussed.

2.3 Inner Tracking System (ITS)

The ALICE Inner Tracking System (ITS) is the innermost detector of ALICE, which is situated closest to the interaction point (IP). The main functions of the ITS are to determine the primary collision vertex to a resolution better than 100 μm, determine secondary vertices for hyperon decays ($\Lambda, \Xi^{-}, \Omega^{-}$, etc.) and heavy flavor decays, PID and tracking for particles at low p_{T} (<200 MeV/c), and to help improve resolution of p_{T} and angle from particles reconstructed by the TPC [26].

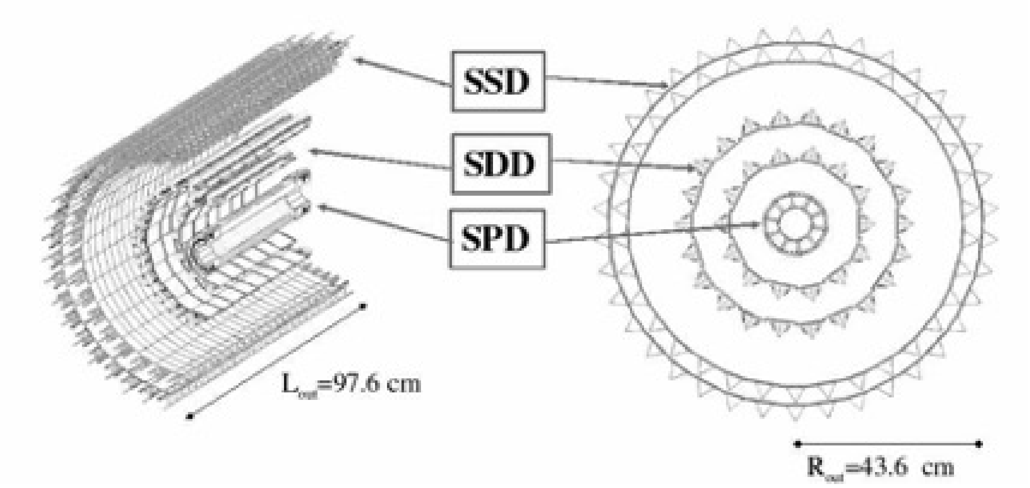

Figure 2.4: A schematic of the ALICE ITS [26]

As seen in Figure 2.4, the ITS is a cylindrical detector that is made up of six total layers of silicon detectors. These silicon detectors are located at radii from 4 cm to 43 cm away from the beam axis and cover a pseudorapidity in the interval of -0.9 $< \eta <$ 0.9 [26].

- Silicon Pixel Detectors (SPD) make up the first two innermost layers of the ITS. These layers are located at radii of 3.9 cm and 7.6 cm away from the beam axis. The main purpose of these layers is to help determine the position of the primary vertex as well as determine the impact parameter of tracks originating from weak decays of strange, charm, and bottom hadrons. [26]. Each cell has an area of 50 μm x 425 μm with a cumulative number of cells in the SPD being 9.84 x 10^6 cells. SPDs have an extended pseudorapidity coverage of -1.98 $< \eta <$ 1.98

in order to have uniform track matching with the FMD [26].

- Silicon Drift Detectors (SDD) make up the next two layers of the ITS and are located at radii of 15.0 cm and 23.9 cm away from the beam axis. These layers have excellent multi-particle tracking capabilities and provide energy loss (dE/dx) information for PID. The cells are larger than the SPD, with each cell having the area of 202 μm x 294 μm with a total of 23 x 10^6 cells.

- Silicon Strip Detectors (SSD) make up the two outermost layers of the ITS and are located at radii of 30.0 cm and 43.0 cm away from the beam axis. SDDs provide a two dimensional measurement of track position, which is very important in matching tracks from the ITS to the TPC. They also provide energy loss (dE/dx) information for PID for low momentum particles as well. The cells are even larger still than SDP and SDD, with an area of 95 μm x 40000 μm and a total of 2.6 x 10^6 cells.

2.4 Time Projection Chamber (TPC)

The ALICE Time Projection Chamber (TPC) is the main tracking and particle identification (PID) detector for ALICE. Combined with other detectors in the central-barrel, the TPC is optimized to provide momentum measurements for charged particles with good two-track separation, PID, and vertex determination [26]. The ALICE TPC is cylindrical in shape and is the largest TPC in the world, measuring a total volume of 90 m^3, an inner radius of $\sim$85 cm, and outer radius of $\sim$250 cm, and a length along the beam axis of 500 cm. The TPC volume is filled with a gas mixture of 90% neon and 10% CO_2. The TPC covers the full azimuth ($0 \rightarrow 2\pi$) and a pseudorapidity range of $|\eta| < 0.9$ ($|\eta| < 1.5$ for shorter tracks but with lower momentum resolution) [26].

A schematic for the ALICE TPC layout can be seen in Figure 2.5. The TPC is a large cylindrical chamber that surrounds the ITS that consists of a large field cage with a central high voltage electrode in the middle and two read-out endplates (one on each side of the TPC). When a charged particle from a collision enters the TPC, the particle traverses the gas chamber ionizing gas

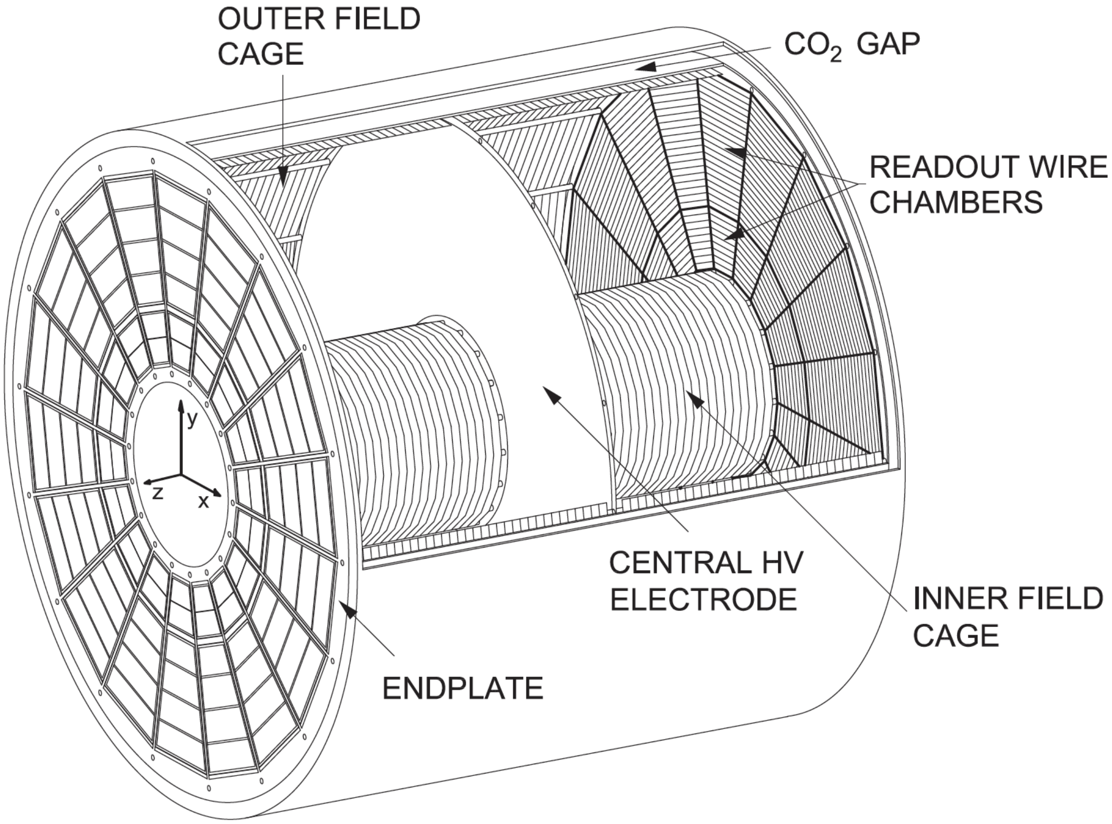

Figure 2.5: A schematic of the ALICE TPC [27]

molecules, which causes the electrons (and ions) to drift toward the endplates (central electrode) [26]. This drift is due to the fact that the central high voltage electrode has an electric potential of 100 kV, which creates a uniform electric field in the beam direction (z-direction) inside the gas chamber of 400 V/cm [26]. The endplate readout chambers are Multi Wire Proportional Chambers (MWPC) with cathode pad readout and a gated wire grid to block drifting charges when the TPC is untriggered [26][28]. The electrons interact with the grid of charged wires and cause the electrons to avalanche, resulting in a secondary production of electrons and ions. Since the drifting electrons originating from the initial gas ionization do not induce a large enough signal in the readout planes, this amplification process is necessary [29].

The amount of secondary produced electrons gives information about the number of primary induced electrons, which gives the energy loss of the charged particle as it traverses the TPC. Also, the secondary ions produced can give information about the spatial position of the charged particle in the xy-plane. The maximum drift time is on the order of 90 μs, which is how long the gating plane stays open to allow electrons to drift toward the pad planes. When closed, primary electrons do not reach the anodes and secondary ions do not enter the body of the TPC to distort the electric field [29]. A charged particle track with electrons drifting and the pad plane readout can be seen in Figure 2.6.

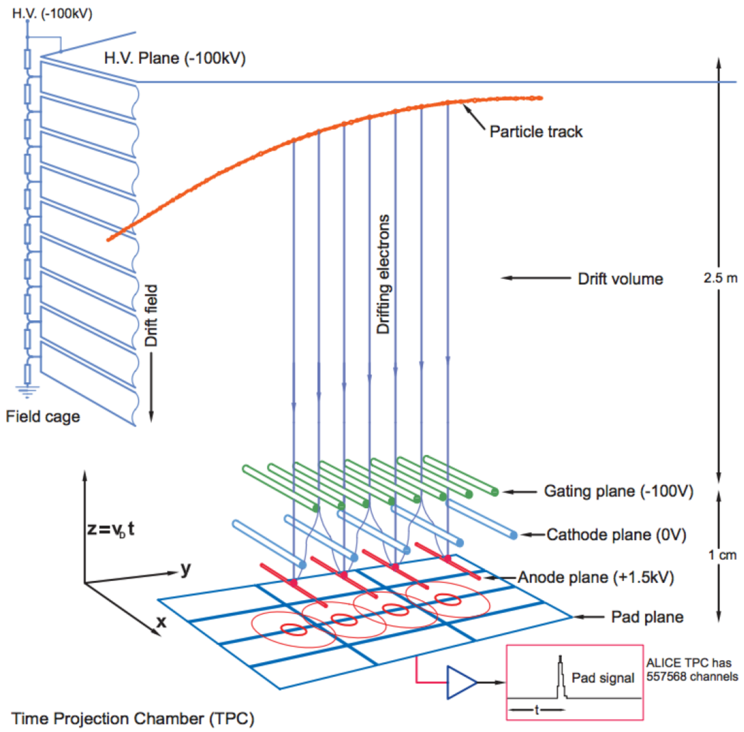

Figure 2.6: A charged particle track in the TPC drifting to readout [32]

The ALICE TPC and other central-barrel detectors sit inside a 0.5 T solenoidal magnetic field [26]. This constant magnetic field combined with the electric field from the TPC will cause charged particles moving through the chamber to have a curved path, or helical motion. The direction of the charged particle is determined by the initial kinematics after the collision and the electric field, but the magnetic field will cause the trajectory to have a circular motion component as dictated by the Lorentz force

$$\vec{F} = q\vec{E} + \vec{v}\,\mathrm{x}\,\tilde{\mathrm{B}}, \tag{7}$$

where $\vec{F}$ is the net Lorentz force on the charged particle, q is the charge, $\vec{E}$ is the external electric field, $\vec{v}$ is the linear velocity of the particle, and $\vec{B}$ is the external magnetic field. If we assume that the magnetic field is completely perpendicular to the momentum of the charged particle (thus velocity) in the TPC, the magnetic component of Eq. 7 becomes

$$qvB = \frac{\gamma m v^2}{r}. \tag{8}$$

The mass and velocity terms can be replaced by relativistic transverse momentum ($p_T = \gamma m v$) which then simplifies Eq. 8 even further to

$$qB = \frac{p_{\mathrm{T}}}{r}. \tag{9}$$

The curved nature of a charged particle track can be seen in Figure 2.6. The red path of the charged particle is bent, indicating it is in the presence of a magnetic field. It can be seen from Eq. 9 that there is a relationship between transverse momentum and radius of curvature. Since q is constant for a given particle species and B is constant at ALICE, charged particles with a large momentum will also have a large radius of curvature, meaning they are less impacted by the magnetic field. Charged particles with lower momenta will have a small radius of curvature, meaning they are greatly impacted by the magnetic field. Due to the fact that the magnetic field is very strong, lower momentum charged particles of $p_{\mathrm{T}} \leq 100$ MeV/c are curved to the point that they do not reach the majority of the central-barrel detectors [29].

The TPC uses energy loss per unit length (dE/dx) of the charged particle in the gas chamber in order to identify particles. The energy loss in the TPC can be theoretically described by the Bethe-Bloch paramaterization [31]

$$\left\langle \frac{dE}{dx} \right\rangle = \frac{4\pi N e^4}{m_e c^2} \frac{Z^2}{\beta^2} \left(\ln \frac{2\mathrm{m_e} c^2 \beta^2 \gamma^2}{\mathrm{I}} - \beta^2 - \frac{\delta(\beta)}{2} \right) \tag{10}$$

where N is the number density of electrons in the gas medium, e is the elementary electric charge, $m_e c^2$ is the rest energy of the electron, Z is the charge of the particle, β is the speed of the particle over the speed of light (v/c), γ is the Lorentz factor ($1/\sqrt{1-\beta^2}$), and I is the mean excitation energy of the atom.

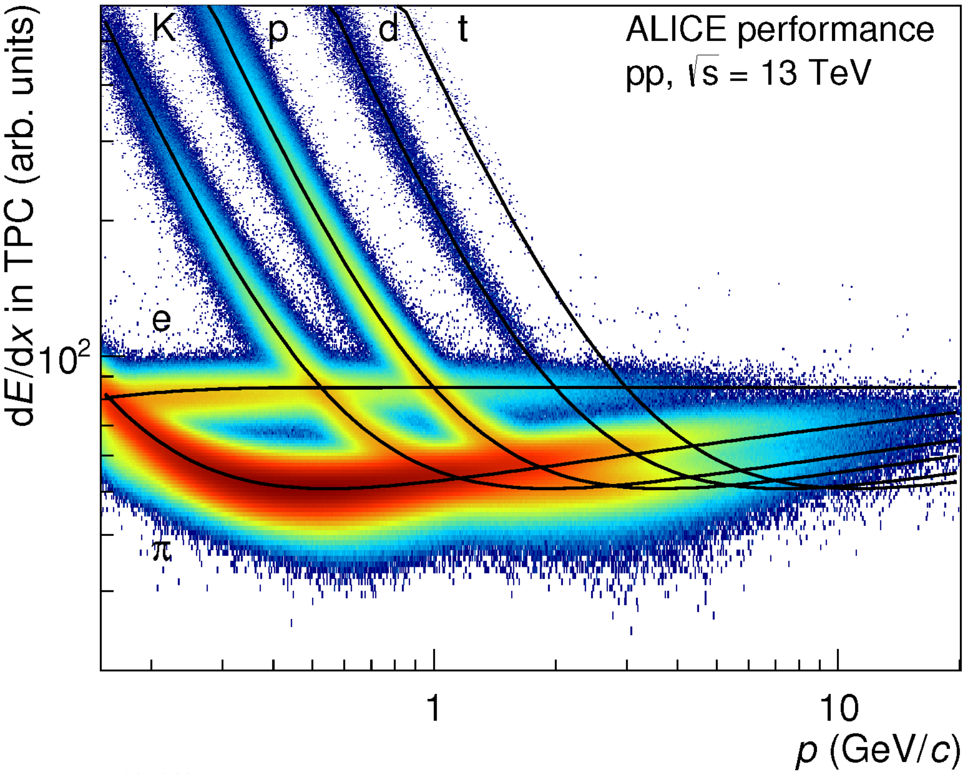

Figure 2.7: Specific energy loss (dE/dx) vs momentum in the TPC for 0.2 T for Run 2 pp collisions at $\sqrt{s} = 13$ TeV. Solid black lines indicate the signal calculated from the Bethe-Bloch formula for a particle species. Color intensity corresponds to the number of signals for dE/dx measured for a specific p value.

Different particle species tend to have a different dE/dx signature at different values of transverse momentum. This can be seen in Fig. 2.7. A parameter known as n_σ is used to match a track in the TPC to the signature of a specific particle species. The Bethe-Bloch function is a parameterization on the ionization energy loss data. Particle identification is done by considering n_σ to be the difference between the measured value of (dE/dx) and the theoretical value of (dE/dx) obtained by the Bethe-Bloch paramaterization divided by the resolution of the TPC

$$n_\sigma = \frac{(dE/dx)_{measured} - (dE/dx)_{Bethe-Bloch}}{\sigma_{TPC}}. \tag{11}$$

The closer n_σ is to zero, the closer the track is to the theoretical Bethe-Bloch value and the more certain the track is identified as the correct particle species.

Looking at the lower momentum range of Fig. 2.7, we can see that particles have a significant 3σ separation from one another and thus can be easier to identify. This allows for charged pions, protons, and kaons to be identified in the range of 0.25-0.70 GeV/c, 0.45-0.90 GeV/c, and 0.25-0.45 GeV/c respectively [32]. The TPC is not able to accurately separate these particles from one another in the range of 1.0 - 3.0 GeV/c due to the intersections of their dE/dx. In the higher momentum range, the TPC is once again able to resolve the separation between pions, protons, and kaons with a 1-3 σ separation in the ranges $p_T > 3.0$ GeV/c, $p_T > 4.0$ GeV/c, and $p_T > 4.0$ GeV/c, respectively. This region is known as the relativistic rise due to the increase in value from the Bethe-Bloch parameterization for each particle.

2.5 Time of Flight (TOF)

The Time of Flight (TOF) detector was designed and implemented to improve the capability of ALICE to identify charged particles. As explained at the end of Section 2.4, the TPC is not able to accurately identify charged particles in the intermediate momentum range. The TOF is able to cover this missing momentum range from around 0.4 GeV/c to 3 GeV/c. The ITS, TPC, and TOF can now cover a very wide range of transverse momentum, from 0.150 GeV/c to 20 GeV/c, for particle identification.

The ALICE TOF is a cylindrical detector that has a pseudorapidity coverage of $|\eta| < 0.9$ over

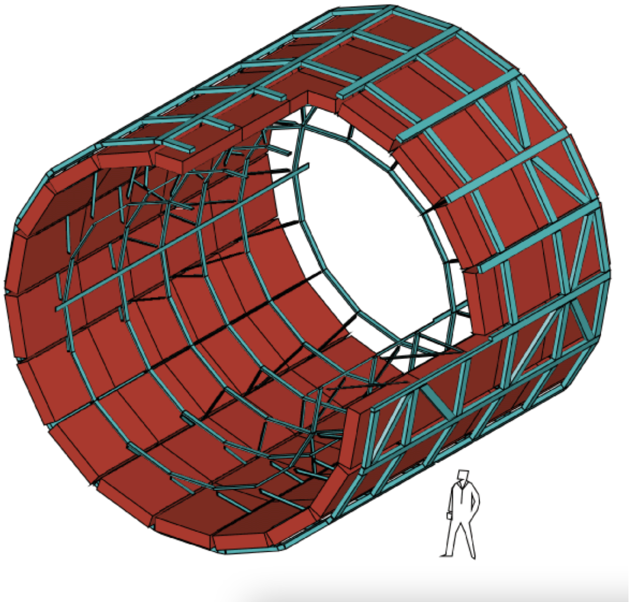

Figure 2.8: Schematic view of the ALICE Time Of Flight detector [34].

the full azimuth ($0 \rightarrow 2\pi$). The TOF has a modular structure that consists of 18 sectors in ϕ and 5 segments in the beam direction [23][26]. The entire TOF is inside a cylindrical shell with inner radius of 370 cm and outer radius of 399 cm away from the beam pipe [23][26]. A schematic showing the layout and relative size of the TOF is shown on Fig. 2.8.

The TOF contains 1638 Multigap Resistive Plate Chamber (MRPC) strips. Each MRPC strip is 122 cm long by 13 cm wide and consists of stacks of glass plates with a high voltage applied to its external surface [26]. When a charged particle traverses the TOF, it ionizes the gas molecules in between the gaps of the plates, which causes a gas avalanche. This means that the freed electrons will be accelerated by the electric field in the TOF, which causes them to bump into more gas molecules which will free even more electrons, which amplifies the electric signal [26]. The resistive glass plates are not only transparent to the signal produced, they also stop the avalanche in order to stop the amplification from sparking [26]. An illustration of a particle traversing the TOF can be seen in Fig. 2.9. The TOF is able to determine the time it takes for a charged particle to cross

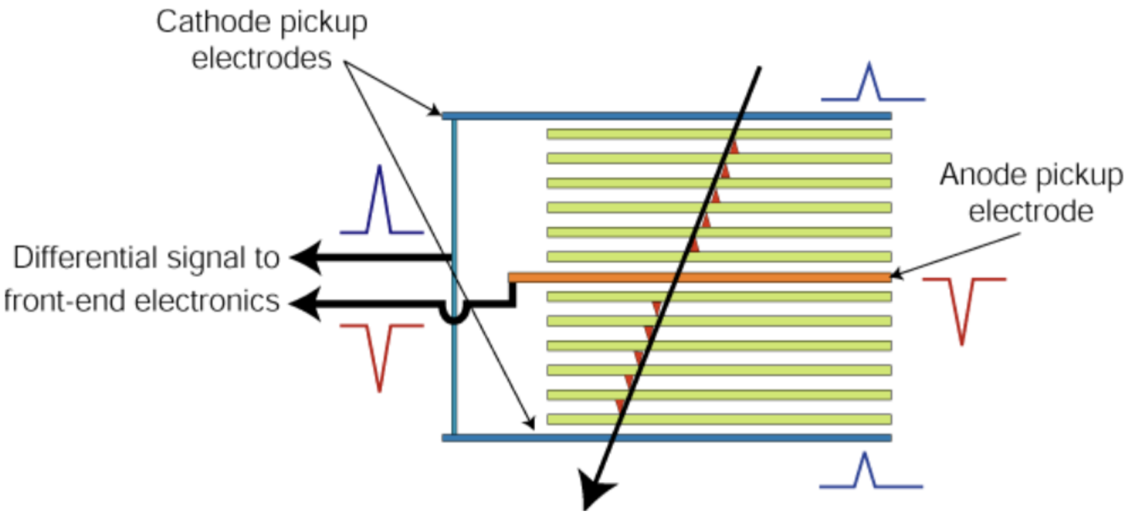

Figure 2.9: A charged particle passing through the TOF ionizing gas molecules and inducing an electric signal [33].

the TOF from the initial collision vertex. Using the timing information, the TOF can determine the mass of the particle by the equation

$$m = \frac{p}{c}\sqrt{\frac{c^2t^2}{l^2} - 1} \tag{12}$$

where m is the mass of the particle, p is its momentum as measured by the ITS/TPC, t is the time of flight, and l is the track length. The initial starting time of the particle at the primary vertex is determined by the T0 detector, which will be discussed in the next section (Section 2.6).

The main scope of the TOF is to find the time of flight of each particle from the primary vertex to the TOF detector. The timing obtained from the TOF signal combined with the distance the particle traveled will determine the velocity $\beta = v/c$. The values for β for a given charged particle as a function of p_T are shown in Fig. 2.10. The primary purpose of the TOF is to obtain a difference between the signals of $K - p$ and $K - \pi$. In order to achieve this, the TOF is optimized so that a 3σ separation between π and K is achievable at the higher end of the momentum range for a particle track of 4 meters. Misidentification of charged particles tends to occur in the higher momentum range for the TOF because the time difference between two high momentum particles is comparable to the time resolution of the TOF [35]. There is also a lower momentum threshold for the TOF of 300 MeV/c. Charged particles with p_T lower than 300 MeV/c have their tracks curved by the 0.5 T magnetic field so much that the particle is unable to reach the TOF [35].

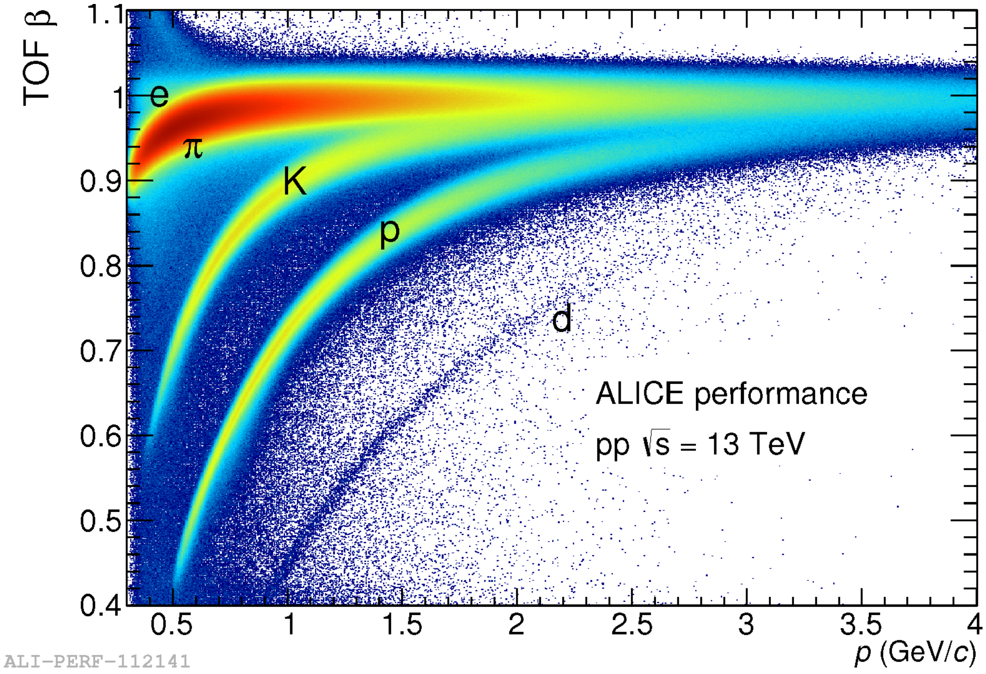

Figure 2.10: TOF β vs momentum performance plot in pp collisions at $\sqrt{s} = 13$ TeV.

2.6 T0 and VZERO Detectors

As previously mentioned, the ITS, TPC, and TOF are the main detectors used for this analysis. These detectors work in conjunction with other detectors to assist in the data taking process.

The V0 detector is a small angle detector that consists of two separate arrays of scintillator counters, named VZERO-A and VZERO-C, which are located on different sides of the interaction point [26]. This can be seen in Fig. 2.3. A sketch of the two VZERO detectors can be seen in Fig. 2.11. The VZERO-A is located 340 cm from the interaction point on the opposite side of the muon spectrometer and the VZERO-C is located 90 cm from the interaction point. The VZERO-A covers

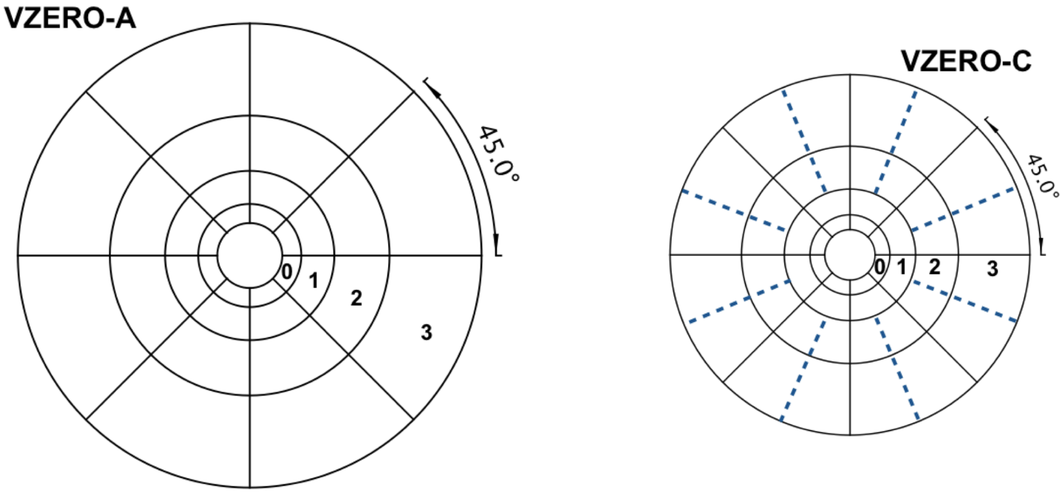

Figure 2.11: Sketches of VZERO-A and VZERO-C arrays with their segmentation [36].

a pseudorapidity range of 2.8 $\leq \eta \leq$ 5.1 while the VZERO-C covers a range of -3.7 $\leq \eta \leq$ -1.7. Tha main purpose of the VZERO detector is to provide a trigger to the central-barrel detectors for minimum-bias events in pp and A-A collisions. When a collision occurs, particles are emitted from the primary vertex which can activate the trigger. Secondary interactions in the vacuum chamber elements can also activate the trigger [26]. There is a linear dependence between the number of registered particles in the VZERO detector and the number of primary particles emitted, making the VZERO detector a good indicator of the centrality of a Pb-Pb collision via the recorded multiplicity in the event. The simplest trigger is a minimum-bias (MB) trigger, which occurs when an event produces any signal in the VZERO-A and the VZERO-C [26]. This will categorize the event as being part of the minimum-bias dataset with trigger kINT7. These triggers help determine whether an event truly did occur or if the observed signals in the central-barrel detectors came from beam-gas interactions [26].

The ALICE T0 detector consists of two arrays of Cherenkov counters. Similar to the VZERO detector, the T0 consists of two separate arrays that are located on different sides of the interaction point. This can be seen in Fig. 2.3 T0-C is located 72.7 cm away from the interaction point with a pseudorapidity range of -3.28 $\leq \eta \leq$ -2.97 while the T0-A is located 375 cm away from the interaction point with a pseudorapidity range of 4.61 $\leq \eta \leq$ 4.92 [26]. The main purpose of the T0 detector is to generate a start time for the TOF. The timing of the signal in the T0 serves as the real time of the collision, which is independent of the position of the collision vertex [26]. The T0 also helps with determining the location of the primary vertex and help discriminate against beam-gas interactions [26].

3 Pentaquarks

As mentioned previously, quarks and gluons that are not in a QGP are bound to other quarks and gluons via the strong force. These states are typically composed of a quark and anti-quark (a meson) or three quarks (a baryon). The search for particles beyond this standard has been ongoing since the acceptance of the quark model. This dissertation will focus on the search for pentaquarks, which contain a total of five quarks (four quarks and one anti-quark).

The structure of such a particle is another piece of the exotic hadron puzzle that is unknown.

Figure 3.1: Pentaquark structure illustrations. The image on the left shows a five quark bag structure, while the image on the right shows a molecular baryon-meson structure [37].

Fig. 3.1 shows an excellent illustration of the two different pentaquark structure predictions. When the five quarks form a bound state, do they all coalesce into a five quark bag? Or, do they first form the familiar baryon and meson before they form a molecular state of a baryon-meson? Yield predictions for heavy ion collisions from the ExHIC collaboration may help determine which structure is more likely. Using statistical hadronization models, yield predictions for the molecular state are higher than yield predictions for a tightly bound five quark state [16].

Determining a pentaquark yield experimentally and comparing to the models from ExHIC can help determine which structure better matches the data [16]. Fig. 3.2 shows a table of different

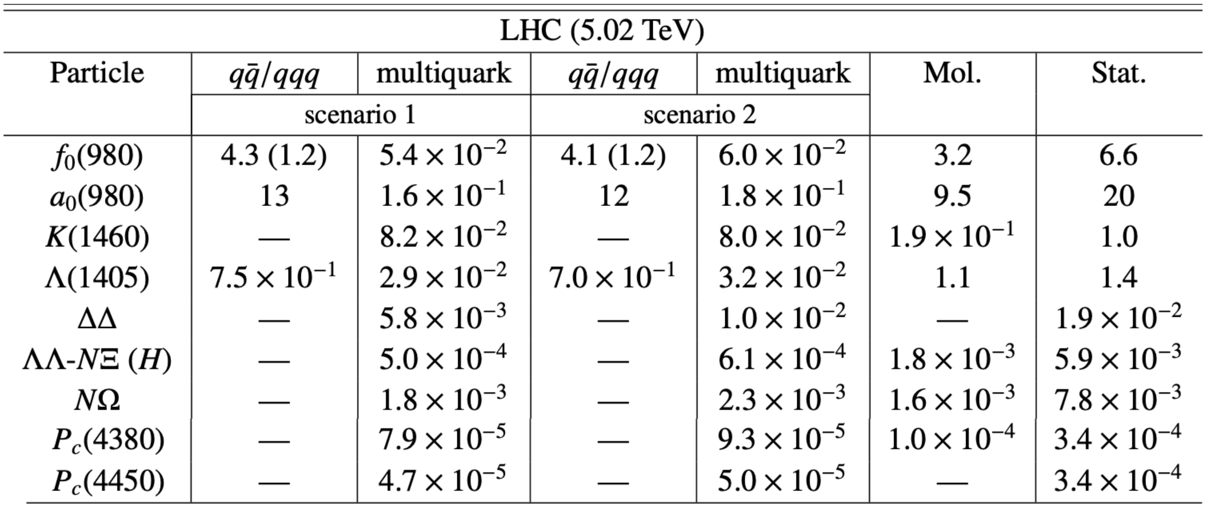

LHC (5.02 TeV)						
Particle	$q\bar{q}/qqq$	multiquark	$q\bar{q}/qqq$	multiquark	Mol.	Stat.
	scenario 1		scenario 2			
$f_0(980)$	4.3 (1.2)	5.4×10^{-2}	4.1 (1.2)	6.0×10^{-2}	3.2	6.6
$a_0(980)$	13	1.6×10^{-1}	12	1.8×10^{-1}	9.5	20
$K(1460)$	—	8.2×10^{-2}	—	8.0×10^{-2}	1.9×10^{-1}	1.0
$\Lambda(1405)$	7.5×10^{-1}	2.9×10^{-2}	7.0×10^{-1}	3.2×10^{-2}	1.1	1.4
$\Delta\Delta$	—	5.8×10^{-3}	—	1.0×10^{-2}	—	1.9×10^{-2}
$\Lambda\Lambda$-$N\Xi$ (H)	—	5.0×10^{-4}	—	6.1×10^{-4}	1.8×10^{-3}	5.9×10^{-3}
$N\Omega$	—	1.8×10^{-3}	—	2.3×10^{-3}	1.6×10^{-3}	7.8×10^{-3}
$P_c(4380)$	—	7.9×10^{-5}	—	9.3×10^{-5}	1.0×10^{-4}	3.4×10^{-4}
$P_c(4450)$	—	4.7×10^{-5}	—	5.0×10^{-5}	—	3.4×10^{-4}

Figure 3.2: Yield predictions from the ExHIC collaboration for hadrons with different quark structures [16].

particles with yield predictions based on different quark structures. The columns labeled “$q\bar{q}/qqq$” show yields based on a typical two or three quark bound state. The columns labeled “multiquark” show yields based on a tightly compact bag structure of more than 3 quarks. The last two columns, “Mol.” and “Stat.” show yields based on a molecular structure of meson-meson, baryon-meson, or baryon-baryon. The yields for the molecular structure are typically much higher and therefore preferred by theory. In order to determine a pentaquark yield experimentally, a signal for a pentaquark would first need to be observed.

3.1 Previous Pentaquark Searches

3.1.1 Early Searches

The first claim of a pentaquark discovery came from LEPS (Laser Electron Photon Experiment at SPring-8) in Japan in 2009. LEPS studied the reaction $\gamma n \to K^+K^-n$ by scattering photons off of a sample of ^{12}C and measuring both K^+ and K^- at forward angles. To ensure that the photon reaction with the proton inside the ^{12}C sample doesn’t contribute to the data, events with the recoiled proton detected by the experiment were eliminated. Fig. 3.3 shows the missing mass

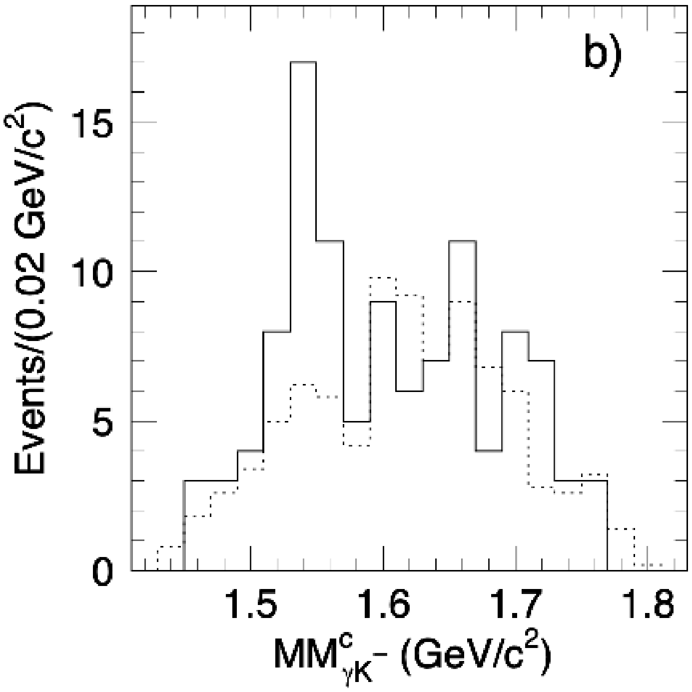

Figure 3.3: Missing Mass ($MM^c_{\gamma K^+}$) spectrum for K^+K^- productions for the signal sample (solid line) and for events from the LH_2 (dotted line). A peak in the signal sample histogram near 1.54 GeV/c^2 is visible [39].

spectrum for K^+K^- productions. The histograms show that, when the mass of the K^- is accounted for, the "missing mass" left over from the event is plotted. Only events with known pairs of K^+K^- are analyzed and only events with a neutron are allowed, so the missing mass must come from nK^+. A sharp baryon resonance peak is observed at 1.54 GeV/c^2. The quark content of such a resonance would be $udd u\bar{s}$, making this an open strangeness pentaquark known as $\Theta(1540)^+$. While the total set of events was 43 M, only 8,000 events had K^+K^- pairs. Even fewer events satisfied additional cuts [39].

Other experiments such as DIANA, CLAS, and SAPHIR corroborated the $\Theta(1540)^+$ peak using similar production mechanisms as LEPS [40]. Also similarly, each of these corroborative results were obtained using low statistics. Also, mass peak locations between the different experiments varied by more than expected for a narrow resonance. In 2006 with higher statistics, CLAS followed up its original result with new results that showed no peak for the $\Theta(1540)^+$. Several other experiments followed suit with higher statistics analyses and found no peak [40].

3.1.2 NA49

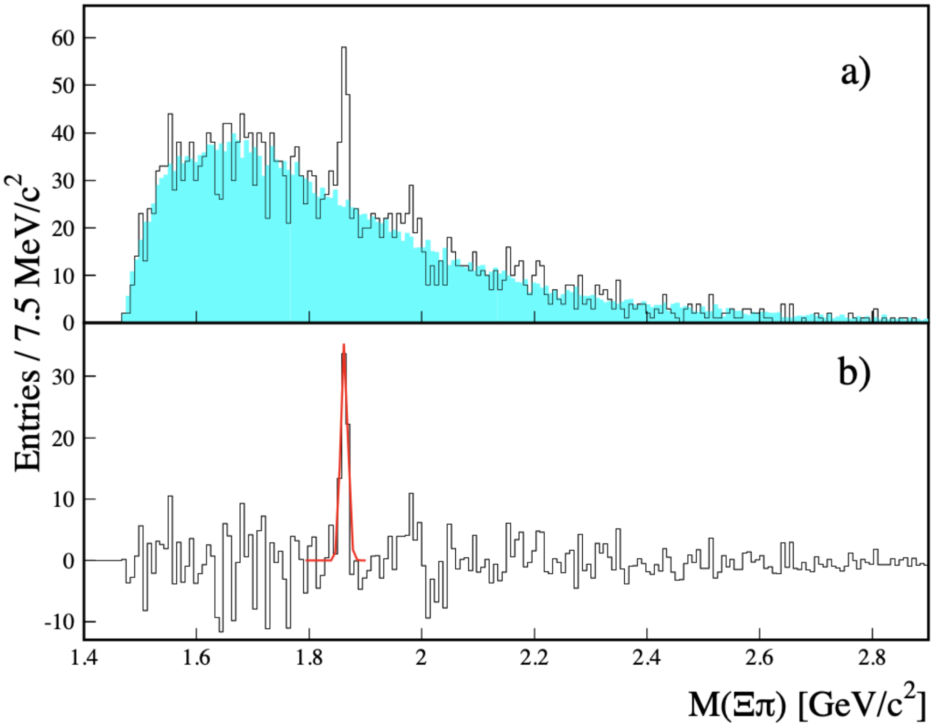

Figure 3.4: (a) The Invariant mass spectrum of the sum of $\Xi^-\pi^-$, $\Xi^-\pi^+$, $\bar{\Xi}^+\pi^-$, and $\bar{\Xi}^+\pi^+$. The shaded blue region is the normalized mixed-event background. (b) Background subtracted distribution with Gaussian fit to the peak [41].

In 2003, the NA49 fixed target experiment at the Super Proton Synchrotron (SPS) at CERN had claimed to observe another pentaquark state, $\phi(1860)$. NA49 searched for resonances in the $\Xi\pi$ channel invariant mass spectra in pp collisions at $\sqrt{s} = 17.2$ GeV [41]. The total number of events analyzed was about 6.5 million, but after event selection that number reduced to 2.75 million. After only selecting events with a Ξ^- or $\bar{\Xi}^+$, the number of events dwindled to ~2,200 [41]. Although the events that were used met rigorous selections and cuts, NA49 faced similar issues of low statistics that other experiments had faced.

Fig. 3.4 shows the invariant mass spectrum for the sum of $\Xi^-\pi^-$, $\Xi^-\pi^+$, $\bar{\Xi}^+\pi^-$, and $\bar{\Xi}^+\pi^+$. A very clear signal can be seen well above background centered at 1.86 GeV/c^2 [41]. The shaded blue mixed-event background is subtracted to leave a very nice peak which is then fit with a Gaussian. The majority of the peak contribution comes from the $\Xi^-\pi^-$ and $\Xi^-\pi^+$ distributions, which means that they claimed to observe $\phi(1860)^{--}$ with quark content $dssd\bar{u}$ and $\phi(1860)^0$ with quark content $dssu\bar{d}$ [41]. Observation of a pentaquark state with open strangeness is a remarkable achievement, but also to be doubly charged is something that grabbed attention. Other experiments attempted to replicate this mass peak with higher statistics but were unsuccessful [40][42].

3.1.3 ALICE

Even as late as 2014, the ALICE experiment had attempted to observe the $\phi(1860)$. ALICE analyzed ~250 million minimum bias pp collisions at $\sqrt{s} = 7$ TeV in order to study $\Sigma(1385)^{\pm}$, $\Xi(1530)^0$, and $\phi(1860)$ [42]. The same decay channels were searched, $\phi(1860)^0 \rightarrow \Xi^-\pi^+$ and $\phi(1860)^{--} \rightarrow \Xi^-\pi^+$.

Fig. 3.5 shows the invariant mass spectra for both decay channels. There is clearly a lack of evidence for a $\phi(1860)$ peak in either distribution. The $\Xi^-\pi^+$ distribution shows a clear peak at 1530, which is a well known resonance, $\Xi(1530)^0$.

The lack of any significant pentaquark signal in any high statistics analysis had caused the community to conclude that the $\Theta(1540)^+$ does not exist [40]. After the "discovery" of the $\Theta(1540)^+$ and a few subsequent experiments confirming the observation, the Particle Data Group (PDG) included it in its list of known particles in 2004. However, as previously mentioned, higher statistics analyses did not corroborate the mass peak, which caused the PDG to remove the $\Theta(1540)^+$ from the listing, and even going a step further saying "The conclusion that pentaquarks in general, and the Θ^+, in particular, do not exist, appears compelling" [40].

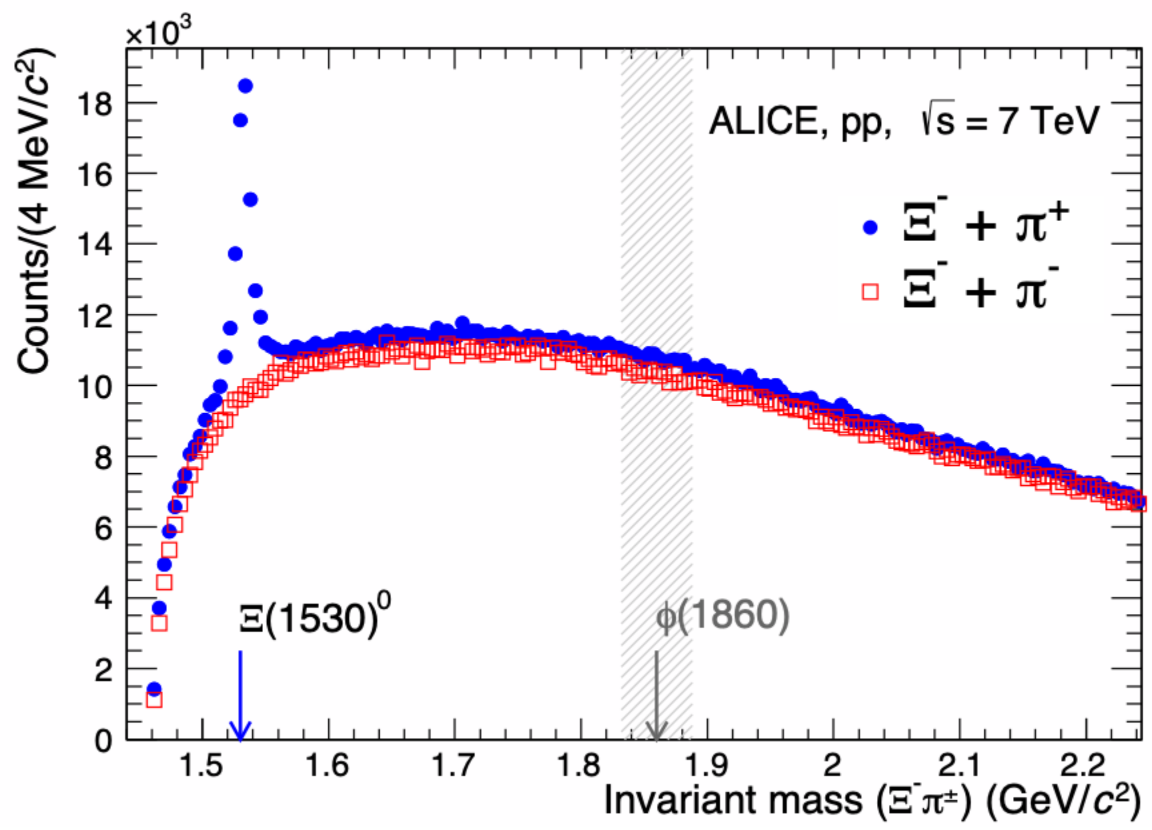

Figure 3.5: Invariant mass distributions of $\Xi^-\pi^+$ and $\Xi^-\pi^-$ at ALICE in pp collisions at $\sqrt{s} = 13$ TeV. The shaded area indicates the region at which the $\phi(1860)$ is expected [42].

3.2 LHCb discovery of P_c^+ states

In 2015, the LHCb collaboration at the LHC observed two exotic structures in the $J/\psi p$ channel in $\Lambda_b^0 \to J/\psi K^- p$ decays in pp collisions at $\sqrt{s} = 7$ TeV and 8 TeV [43]. LHCb was studying the decay of $\Lambda_b^0 \to J/\psi \Lambda^* \to J/\psi K^- p$, but noticed an inexplicable peak in the $J/\psi p$ invariant mass distribution. This hints at a different intermediate decay of $\Lambda_b^0 \to P_c^+ K^- \to J/\psi K^- p$. These intermediate decays are shown in Figure 3.6.

The invariant mass distribution reconstructing the Λ^* from $K^- p$ is very well understood. The data can be reproduced from an amplitude fit with contributions from 14 different Λ^* states. The peaks that are visible in the data are well known resonances. This is not the same case for the $J/\psi p$

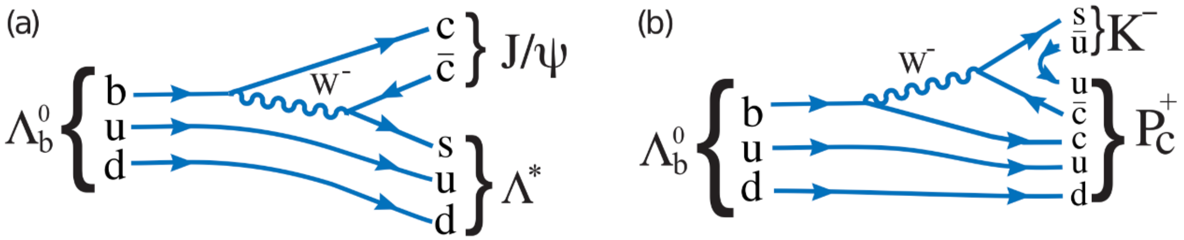

Figure 3.6: Intermediate decays of Λ_b^0. (a) Shows $\Lambda_b^0 \rightarrow J/\psi\Lambda^*$ and (b) shows $\Lambda_b^0 \rightarrow P_c^+K^-$. Both show the bottom quark undergoing a flavor changing process from $b \rightarrow c$ through a W$^-$ boson [43].

invariant mass distribution. There is a massive peak around 4.4 GeV/c^2 that cannot be explained by any known resonances. Without adding new additional states, the amplitude fit cannot reproduce the data. The addition of two Breit-Wigner amplitudes with masses of 4380 MeV/c^2 and 4450 MeV/c^2 and widths of 205 MeV/c^2 and 39 MeV/c^2 respectively, helped obtain a satisfactory fit to the data. The fits to the data can be seen in Figure 3.7. These states would strongly decay, have the minimal quark content of uudc$\bar{c}$, and each mass state would have a spin assignment of 3/2 and 5/2.

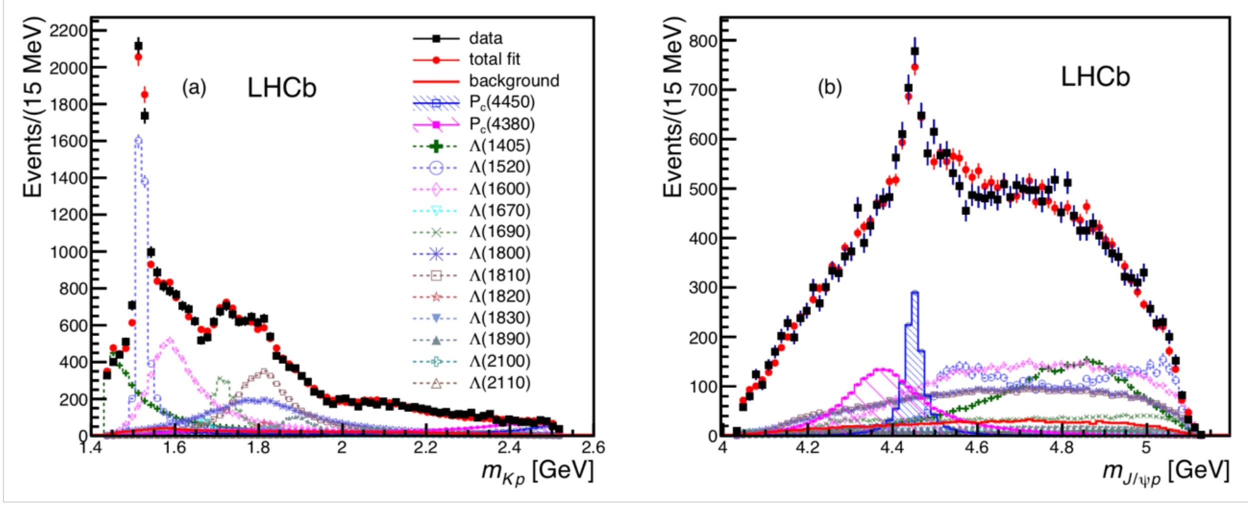

Figure 3.7: Invariant mass distributions for (a) Kp and (b) $J/\psi p$. The data is shown in solid black squares while the total fit is shown in solid red circles. The contributions from the P_c states are shown on the right in the blue and purple shaded peaks [43].

In 2019, LHCb followed up their 2015 discovery of the P_c states with an updated analysis of the same Λ_b^0 decay channels, but at a higher energy of $\sqrt{s} = 13$ TeV with increased statistics. This new analysis shed much more light on the nature of these pentaquarks. LHCb revealed a new, lower mass state, $P_c(4312)$, with a width of 9.8 MeV/c^2. The collaboration also resolved the previous $P_c(4440)^+$ into two distinct peaks, $P_c(4457)^+$ and $P_c(4450)^+$, with widths of 20.6 MeV/c^2 and 6.4 MeV/c^2, respectively. The previously observed $P_c(4380)$ peak is not apparent in the 2019 follow up analysis, and the fits do not confirm nor contradict its existence [44].

Possibly the most exciting finding from this 2019 P_c analysis is that the peaks of these resonance lie *just* below the mass threshold of $\Sigma_c^+\overline{D}^0$ and $\Sigma_c^+\overline{D}^{*0}$ ([udc][u$\bar{\text{c}}$]). The total mass of $\Sigma_c^+\overline{D}^0$ is 4317 MeV/c^2 and the total mass of $\Sigma_c^+\overline{D}^{*0}$ is 4460 MeV/c^2 This may give us some insight as to the internal structure of the P_c. The P_c having narrow widths, masses below the previously mentioned mass thresholds, and being within plausible hadron-hadron binding energies gives evidence of a baryon-meson bound state. A tightly bound 5 quark bag state being near these mass threshold would merely be a coincidence [45]. In order to properly determine the internal structure of these pentaquarks, more experimental and theoretical scrutiny is needed. The updated P_c distributions are shown in Figure 3.8.

There are questions that arise from the discoveries of these exotic states. How many more P_c states can we find? Does this extend into four quarks states? Or six quark states? Can we find pentaquarks in the *strange* sector using analogous decay channels?

3.3 Hidden Strangeness Pentaquarks

The discovery of the P_c states, coupled with the strangeness enhancement measured by ALICE even in pp collisions, significantly adds to the likelihood of observing a pentaquark in the strange sector. The observed P_c decay channel is $\text{P}_c^+ \rightarrow J/\psi p$. The analogous decay in the strange sector would be $\text{P}_s^+ \rightarrow \phi p$. This only changes the quark content of the pentaquark (P_c^+(uudc$\bar{\text{c}}$) $\rightarrow \text{P}_s^+$(uuds$\bar{\text{s}}$)), with J/ψ having quark content c$\bar{\text{c}}$ and ϕ having quark content s$\bar{\text{s}}$. The observed P_c masses all fell near the thresholds of $\Sigma_c^+\overline{D}^0$ or $\Sigma_c^+\overline{D}^{*0}$, which can direct a strange pentaquark search toward the

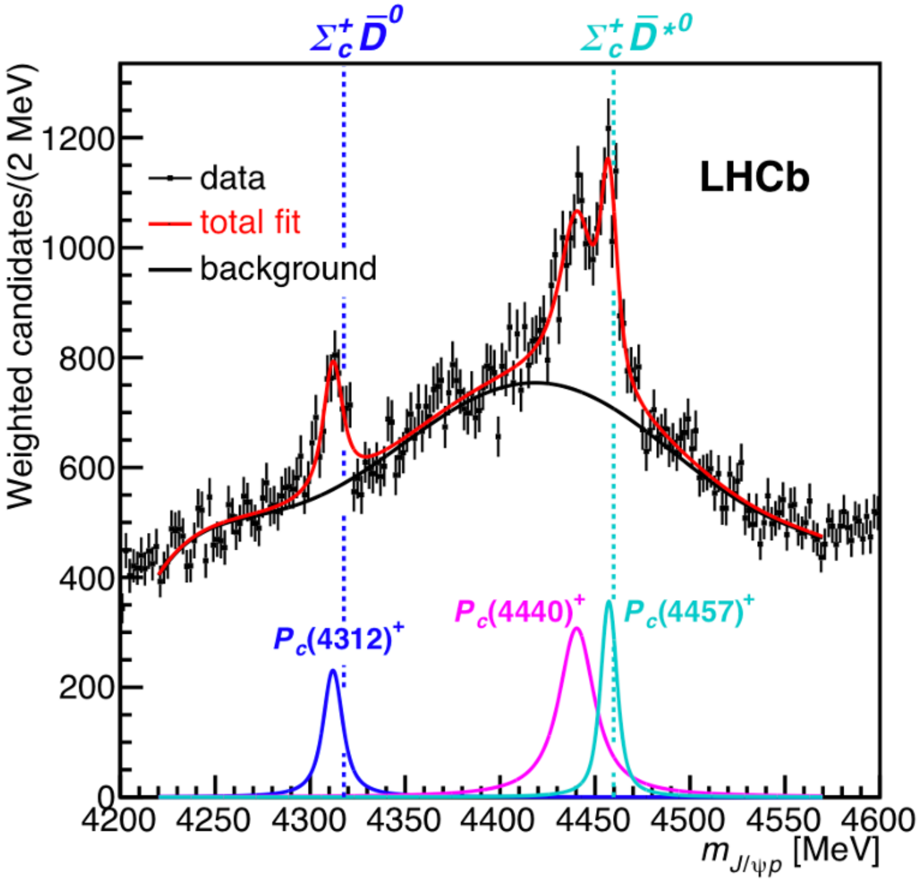

Figure 3.8: P_c^+ invariant mass distributions from LHCb (2019). New peak at 4312 MeV/c^2, and split peaks at 4440 MeV/c^2 and 4457 MeV/c^2. Mass thresholds for $\Sigma_c^+\overline{D}^0$ and $\Sigma_c^+\overline{D}^{*0}$ are superimposed [44].

threshold mass of ΣK, ΣK^*, $\Sigma^* K$, or even $\Sigma^* K^*$.

3.3.1 Predictions from Theory

As mentioned in Section 1.5, there have been theoretical models for how exotic states can form and what characteristics these particles may have for decades. While previous experimental evidence gives an excellent outlook on how to search for pentaquarks, theoretical predictions also help guide new experimental searches. While observations of the P_c would push the idea of a molecular hadron-hadron state of $\Sigma_c^+\overline{D}^0$ or $\Sigma_c^+\overline{D}^{*0}$, is it even possible to do this in the strange sector? Can

ΣK form a bound state? If so, what would the lifetime be? Theoretical models may have answers to these questions.

Not only are there are several models that predict Σ and K can form a bound state [47][49][50][51], but also what decay daughters the P_s could have [47][51], what the mass of the P_s would be [47][48][49][51], and what their widths would be [47][51]. While the analogous decay channel for a strange pentaquark is ϕp, these theoretical models have determined that several other decay channels may be open as well. A table of the potential decay channels with mass and width predictions is shown on Table 1. There are more open channels included in the theoretical models, but these channels are difficult to reconstruct with ALICE.

As an example, one particular decay channel is $\mathrm{P}_s \rightarrow \Sigma K$. $\mathrm{K}^{\pm}$ are directly detected by the ALICE detectors (ITS/TPC/TOF) and K^0 can be identified via its hadronic decay into $\pi^+\pi^-$. However, Σ is much harder to reconstruct. $\Sigma^+(\Sigma^-)$ decays into $p\pi^0$ or $n\pi^+(n\pi^-)$, which both contain a neutral hadron. The neutron does not decay inside the ALICE detector, making it difficult to detect. The π^0 has a $c\tau$ of 25.3 nm, which means it will decay very close to the primary vertex into $\gamma\gamma$, which are still neutral and very difficult to reconstruct. The ITS, TPC, and TOF are able to identify charged hadrons with greater ease than neutral particles, because the charged tracks are bent in the magnetic field. Any decay channel that includes π^0 or neutron is omitted from Table 1.

The mass threshold for a P_s bound state is given by the ΣK configuration at the top of the columns in Table 1. The mass prediction for any given decay channel lies below the mass threshold shown below.

- $M_{\Sigma} + M_K = 1682$ MeV/c^2
- $M_{\Sigma^*} + M_K = 1880$ MeV/c^2
- $M_{\Sigma} + M_{K^*} = 2081$ MeV/c^2
- $M_{\Sigma^*} + M_{K^*} = 2275$ MeV/c^2.

The states with multiple mass predictions tend to center around two values: 2065 MeV/c^2 and

J=1/2	ΣK		ΣK^*		$\Sigma^* K^*$	
S-wave	M_r	Γ_r	M_r	Γ_r	M_r	Γ_r
$N\phi$	-	-	2080.0	3.6	2237.0	30.0
ΛK	1668.0	1.3	2083.4	1.0	2261.5	20.0
ΛK^*	-	-	2056.6	0.2	2219.0	58.0
D-wave						
$N\phi$	-	-	2076.3	0.3	2254.4	0.006
ΛK	-	-	2076.3	0.4	2253.6	0.6
ΣK^*	-	-	2076.8	0.01	2253.3	0.8

J=3/2	ΣK^*		$\Sigma^* K$		$\Sigma^* K^*$	
S-wave	M_r	Γ_r	M_r	Γ_r	M_r	Γ_r
$N\phi$	2060.6	10.4	-	-	2270.5	0.03
ΛK^*	2046.1	15.0	-	-	2265.5	2.0
$\Sigma^* K$	2054.1	2.3	-	-	2263.6	3.7
D-wave						
$N\phi$	2061.0	0.2	-	-	2269.3	0.01
ΛK	2060.6	0.9	1871.6	0.08	2269.2	0.02
ΛK^*	2059.1	0.3	-	-	2269.1	0.05

Table 1: The resonance masses and decay widths (in MeV/c^2) for pentaquarks with J=1/2 (top) and J=3/2 (bottom) [47].

2255 MeV/c^2. For simplicity, we will refer to these two mass states as $P_s(2065)$ and $P_s(2255)$. Width predictions, i.e. lifetimes, do not coalesce around any values and range from extremely narrow (0.001 MeV/c^2) to wide (58.0 MeV/c^2). The majority of the width predictions are very small compared to the ALICE detector resolution and would not be able to be discerned. A larger width that is still within theoretical predictions of 20 MeV/c^2 is assumed.

3.3.2 Predictions from Thermal-FIST

The properties of pentaquarks, such as mass, width, lifetime, yield, and so on, can be estimated based on theoretical and experimental models. The decay channels are predicated on previous observations [43][44] and the estimated masses and widths are based on theoretical models [49][50]. For the estimated yield, the thermal model of particle production can help with its determination.

Thermal model predictions for pentaquark yields were obtained using Thermal-FIST, which is an open source, user friendly package within the HRG (Hadron Resonance Gas) models [69].

HRG models are statistical models that describe hadron interactions by resonance formation. This means that the thermodynamics of a gas of interacting hadrons can be approximated by a non-interacting gas of hadrons and resonances. This approach has been very successful in describing particle multiplicities in heavy ion collisions [70]. Calculations in this analysis are made using the Grand Canonical Ensemble, where baryon number, B, electric charge, Q, and strangeness, S, are conserved on average.

Thermal-FIST is able to analyze particle production in heavy ion collisions by performing thermal fits to input hadron yield data. The thermal fits are achieved by minimizing the value

$$\frac{\chi^2}{N_{\mathrm{dof}}} = \frac{1}{N_{\mathrm{dof}}} \sum_{i=1}^{N} \frac{\left(N_i^{\mathrm{exp}} - N_i^{\mathrm{HRG}}\right)^2}{\sigma_i^2} \tag{13}$$

where N_i^{exp} is the experimental hadron multiplicity, N_i^{HRG} is the calculated HRG hadron multiplicity, $\mathrm{N_{dof}}$ is the number of degrees of freedom (data points - fit parameters), and σ_i^2 is the sum if the squares of the statistical and systematic errors $((\sigma_i^{syst})^2 + (\sigma_i^{stat})^2)$. A thoroughly detailed description of Thermal-FIST and the source code can be found in [69] and [71].

The thermal fits employed by Thermal-FIST rely on hadron spectra and hadron yields. The hadron list that was used was the PDG2016+ hadronic spectrum, that has been shown to be a compromise between lists with too few and too many excited states. The PDG2016+ hadronic spectrum contains a total of 738 states, consisting of states with **** (well established states from experimental results), ***, **, and * (least experimental evidence) designations [52]. Hidden-strangeness pentaquarks are not on this list, so in order to obtain a yield prediction from Thermal-FIST, pentaquark states were locally added to the list. The pentaquark masses are set to 2065 and 2255 MeV/c^2, widths are set to 20 MeV/c^2, lifetimes on the order of 10^{-23}s, and so on. Since the branching ratios for each decay channel of the P_s is not known, all branching ratios are set to 100%. No feed down contributions will affect the yield of any P_s state since no known particles will decay into any P_s state. The main contribution to the predicted yield from thermal predictions will be the mass of the particle, as seen in Eq. 5 and described in Section 1.5.

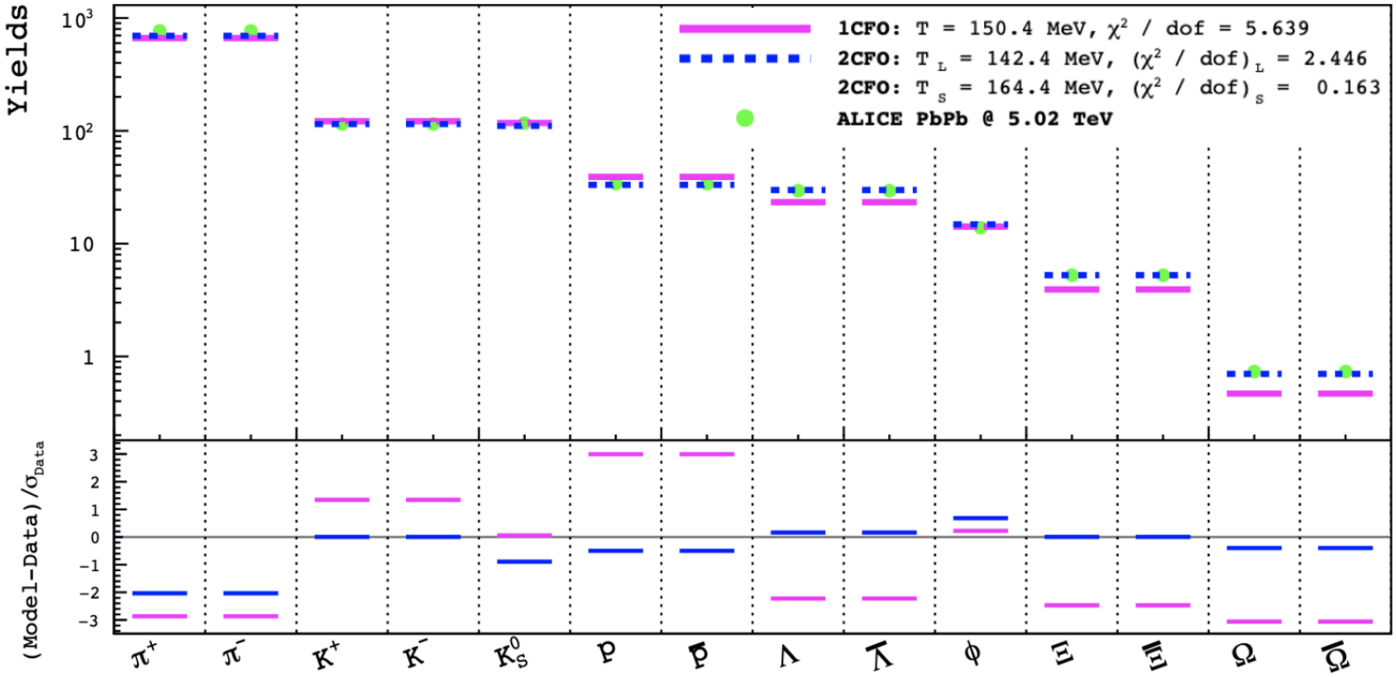

Figure 3.9: Yield calculations using Thermal FIST Grand Canonical Ensemble fits to ALICE Pb-Pb $\sqrt{s_{NN}} = 5.02$ TeV data at 0-10% centrality [72].

Yield data from ALICE for $\pi^{\pm}$, $K^{\pm}$, p, $\bar{p}$, Λ, $\bar{\Lambda}$, Ξ^-, $\bar{\Xi}^+$, Ω^-, $\bar{\Omega}^+$, K^0_S, and ϕ in minimum bias pp collisions at mid-rapidity ($|y|$ <0.5) $\sqrt{s} = 13$ TeV are input in Thermal-FIST. There are typically only 3 fit parameters used for yield calculations: the chemical freeze out temperature, T_{ch}, baryon chemical potential, μ_B, and system volume, V. For T_{ch} at ALICE in pp collisions, this value is fixed to 157 MeV. At the high collision energies of the LHC, μ_B is essentially zero and is fixed to zero for these calculations. V is allowed to vary. Fig. 3.9 shows Thermal FIST yield calculations compared to data (green circles) obtained by ALICE for 0-10% central Pb-Pb collisions at $\sqrt{s_{NN}} = 5.03$ TeV. The magenta lines are calculations based on 1 chemical freeze-out temperature for all quark flavors, while the blue dashed lines are calculations based on 2 chemical freeze-out temperatures, 1 for strange and 1 for light quarks. The bottom plot shows the deviation of each yield calculation from the experimental value.

For the P$_s$ states with a mass of 2065 MeV/c^2, the thermal model calculates a combined particle

+ antiparticle yield of 3.831 $\times 10^{-4}$. For the P_s states with a mass of 2255 MeV/c^2, the thermal model calculates a combined particle + antiparticle yield of 1.290 $\times 10^{-4}$.

4 Analysis Method

4.1 Invariant Mass Reconstruction

In order to study hidden strangeness pentaquark states, pentaquark candidates were measured in pp collisions at $\sqrt{s} = 13$ TeV by invariant mass reconstruction of their hadronic decays into ϕp, Σ^*K, ΛK, and ΛK* utilizing data collected at ALICE. Throughout this chapter, the detailed steps used in the P_s reconstruction will be described.

4.1.1 Data and Event Selection

The results presented in this analysis are obtained using the data from pp collisions at $\sqrt{s} = 13$ TeV recorded in 2015, 2016, 2017, and 2018. There are approximately two billion recorded events using the minimum bias trigger, which are collisions selected with as few constraints as possible. With hidden strangeness pentaquarks expected to be an exceedingly rare particle, using the data set with the highest statistics gives the best chance for a pentaquark signal to be observed with the ALICE detectors. Using a smaller pp system will give a much cleaner signal distribution with much less background as compared to the larger Pb-Pb system. In the event that a pentaquark signal is observed in pp collisions, then searching the Pb-Pb collision data set would be the next logical step. Event selection criteria used in this analysis are as follows:

- Minimum bias trigger selection. If a collision produces a response in the V0A or V0C detectors, it is considered part of the minimum bias data set.
- An event must have V_z, the z-position of the primary vertex, fall within ±10 cm of the center of the central barrel. This is to ensure that the collision occurred at the center of the detector and not outside the expected collision region. This also ensures that the tracks produced from a collision are within the acceptance of the central barrel detectors (ITS/TPC/TOF), even for larger pseudorapidities.
- Pile-up rejection. Pile-up events are events that contain particles or tracks from a different

event. They can be removed using enhanced spatial and temporal primary vertex cuts for the event.

4.1.2 Signal Reconstruction

The P_s signal was reconstructed using invariant mass analysis of decay daughters listed in Section 3.3.1. It should be noted that, for the purposes of this analysis, only P_s^+ and P_s^0 decays are shown, not the antiparticle decay. Each decay channel that is listed also has a corresponding anti-particle that decays in the exact same hadronic way but with the daughter particle's charge conjugate instead. Theoretical predictions used in this analysis do not specify if the predicted hidden strangeness pentaquark states have a net charge or are neutral, so both charge states are considered [47].

The charged states follow a decay process of:

$$\mathrm{P_s^+} \rightarrow \phi\mathrm{p} \tag{14}$$

$$\mathrm{P_s^+} \rightarrow \mathrm{K_S^0}\Sigma^{*+} \tag{15}$$

$$\mathrm{P_s^+} \rightarrow \mathrm{K^+}\Lambda \tag{16}$$

$$\mathrm{P_s^+} \rightarrow \mathrm{K^{*+}}\Lambda \tag{17}$$

The neutral states follow a decay process of:

$$\mathrm{P_s^0} \rightarrow \mathrm{K^+}\Sigma^{*-} \tag{18}$$

$$\mathrm{P_s^0} \rightarrow \mathrm{K_S^0}\Lambda \tag{19}$$

$$\mathrm{P_s^0} \rightarrow \mathrm{K^{*0}}\Lambda \tag{20}$$

It should be noted that many of the decay daughters in these decay channels, ϕ, $\Sigma^{*\pm}$, $\mathrm{K}^{*\pm}$, and

K^{*0}, are in fact resonances themselves. These particles have a lifetime on the order of a few fm/c, with the longest living resonance on the list, ϕ, having a lifetime of 46 fm/c. This is far below the spatial resolution of the ITS of about 100 μm. Because of their short lifetimes, these resonances essentially decay at the primary vertex just like the P_s, and thus need to be reconstructed using the same techniques. These resonances follow a decay process of:

$$\phi \rightarrow \mathrm{K}^+\mathrm{K}^- \tag{21}$$

$$\Sigma^{*\pm} \rightarrow \Lambda\pi^\pm \tag{22}$$

$$\mathrm{K}^{*\pm} \rightarrow \mathrm{K}^0\pi^\pm \tag{23}$$

$$\mathrm{K}^{*0} \rightarrow \mathrm{K}^+\pi^- \tag{24}$$

It should also be noted that both K_S^0 and Λ are electrically neutral particles and will not be directly detected by the TPC and TOF. These particles will need to decay and their decay daughters will be detected by the TPC and TOF. The average decay lengths for K_S^0 and Λ are 2.68 cm and 7.89 cm, respectively, which means that some of them may be able to decay while still inside the TPC. Using the exponential decay law, most of the K_S^0 and Λ particles will decay before or at their decay length, but approximately 36% will decay afterwards. These particles follow a decay process of:

$$\mathrm{K}^0_\mathrm{S} \rightarrow \pi^+\pi^- \tag{25}$$

$$\Lambda \rightarrow \mathrm{p}\pi^- \tag{26}$$

The complete decay for each charged channel would appear as:

$$\mathrm{P}_\mathrm{s}^+ \rightarrow \phi\mathrm{p} \rightarrow \mathrm{K}^+\mathrm{K}^-\mathrm{p} \tag{27}$$

$$\mathrm{P_s^+} \rightarrow \mathrm{K_S^0}\Sigma^{*+} \rightarrow \pi^+\pi^-\mathrm{p}\pi^-\pi^+ \tag{28}$$

$$\mathrm{P_s^+} \rightarrow \mathrm{K^+}\Lambda \rightarrow \mathrm{K^+p}\pi^- \tag{29}$$

$$\mathrm{P_s^+} \rightarrow \mathrm{K^{*+}}\Lambda \rightarrow \pi^+\pi^-\pi^+\mathrm{p}\pi^- \tag{30}$$

The complete decay for each neutral channel would appear as:

$$\mathrm{P_s^0} \rightarrow \mathrm{K^+}\Sigma^{*-} \rightarrow \mathrm{K^+p}\pi^-\pi^- \tag{31}$$

$$\mathrm{P_s^0} \rightarrow \mathrm{K_S^0}\Lambda \rightarrow \pi^+\pi^-\mathrm{p}\pi^- \tag{32}$$

$$\mathrm{P_s^0} \rightarrow \mathrm{K^{*0}}\Lambda \rightarrow \mathrm{K^+}\pi^-\mathrm{p}\pi^- \tag{33}$$

4.1.3 Primary Particle Selection

The cuts and selections used to identify the decay products of a hidden strangeness pentaquark have been determined so as to line up with other analyses of similar resonances. The charged particles that are able to be detected directly from the TPF and the TOF are charged pions, charged kaons, and (anti-)protons. Each of these particles will need to be identified as a primary particle in at least one of the seven different decay channels that are analyzed. The procedure to identify and use a pion, kaon, or proton for reconstruction is simpler than the process to identify a Λ or K_S^0 [32].

The primary track cut selection criteria can be seen in Table 2. Tracks are required to have a $p_{\mathrm{T}} > 0.150$ MeV/c because the strength of the magnetic field used at ALICE will cause the low transverse momentum particles to spiral and not reach the detectors [26]. Primary tracks are required to have at least one hit in the inner two layers of the ITS (SPD). Tracks are required to have a number of crossed rows in the TPC to be at least 70 out of 159 and the ratio of crossed rows over findable clusters to be at least 0.80. This is due to the limited efficiency of the TPC because not all tracks will give a signal as it passes through a row. This allows a better certainty of the properties of the measured track [26]. The DCA to PV (distance of closest approach to the

Track Cuts	**Selection Criteria**
p_{T}	> 0.150 MeV/c
Pseudorapidity	$\lvert\eta\rvert < 0.8$
Number of hits in the inner two layers of the ITS	≥ 1
Number of Crossed Rows in TPC	≥ 70
$\mathrm{N}_{\mathrm{crossed}}/\mathrm{N}_{\mathrm{findable}}$	≥ 0.80
DCA to PV in longitudinal direction	< 2 cm
PID of $\pi^{\pm}$ and $K^{\pm}$ using TPC	$< 2\ \sigma_{TPC}$
PID of (anti-)proton using TPC	$< 5\ \sigma_{TPC}$
PID of $\pi^{\pm}$, $K^{\pm}$, and (anti-)proton using TOF	$< 3\ \sigma_{TPC}$

Table 2: Criteria used to select Primary Tracks

.

primary vertex) in the longitudinal (z) direction is set to < 2 cm to ensure that the track is close enough to the primary vertex.

PID cuts for $\pi^{\pm}$ and $K^{\pm}$ in the TPC and TOF are both set to 2.0 and 3.0 σ, respectively. The PID cut for (anti-)protons is set to 5.0 σ to allow for more protons in the TPC, but set to 3.0 σ in the TOF just like the other primary particles in this analysis. The nσ is slightly increased in the lower momentum range for each particle to have a higher number of particles to use in this analysis.

4.1.4 V^0 Selection

A V^0 is a neutral, unstable baryon or meson that can decay into more stable, lighter oppositely charged hadrons which curve in opposite directions in a magnetic field which forms the shape of a "V" with their decay trajectories. Particles like Λ and K^0_S are considered V^0 particles since they have short lifetimes and are neutral. It should be noted that their lifetimes are not as short as resonance lifetimes. Resonances decay strongly, which leads to a short lifetime on the order of 10^{-23} s and conservation of quantum numbers like strangeness, S. V^0 particles, on the other hand, decay weakly, leading to longer lifetimes and lack of flavor conservation. V^0 particles are electrically neutral, which means they would normally not be directly detectable by ALICE detectors, but it is possible to detect their decay daughters ($\Lambda \rightarrow p\pi^-$ and $K_S^0 \rightarrow \pi^+\pi^-$) because they are charged and stable enough to hit the detectors.

Daughter Track Selection	**Selection Criteria**
Pseudorapidity	$\|\eta\| < 0.8$
Number of Crossed Rows in TPC	≥ 70
$\mathrm{N}_{\mathrm{crossed}}/\mathrm{N}_{\mathrm{findable}}$	≥ 0.80
PID of K^0_S and Λ Daughters using TPC	$< 5\ \sigma_{TPC}$
DCA to PV in xy plane	> 0.06 cm
V0 Selection	K^0_S (Λ) **Selection Criteria**
Pseudorapidity	$\|\eta\| < 0.8$
DCA Between Daughters	< 1 cm
DCA to PV	< 0.3 cm (< 0.4 cm)
Cosine of Pointing Angle	$> 0.97 (> 0.99)$
Transverse Decay Radius, r	$0.5 < \mathrm{r} < 200$ cm
Mass Tolerance	30 MeV/c^2 (6 MeV/c^2)

Table 3: Criteria used to select V^0 candidates.

Selection criteria and cuts used to select V^0 particles and their decay daughters can be seen in Table 3. The top section refers to the selection and cuts specifically for the daughter tracks of the V^0. Pseudorapidity, $\mathrm{N}_{crossedrows}$ and the ratio of $\mathrm{N}_{crossed}/\mathrm{N}_{findable}$ are the same criteria used for primary particles. The difference comes from the PID cuts for the TPC for the protons and pions have a loose cut of 5 σ_{TPC} as to allow more statistics in the V^0 reconstruction. Also, the decay daughters must have a DCA to the PV in the xy plane of greater than 0.06 cm to lend a greater probability that the track came from a V^0 and not the primary vertex.

A diagram of a V^0 decay can be seen in Fig. 4.1. V^0 particles decay away from the primary vertex, leading to a secondary vertex where the V^0 particle's daughters come from. The DCA between the decay daughters is set to be less than 1 cm in order to ensure that the daughters came from the same V^0. The simplest assumption is that the V^0 is at the midpoint of the DCA between the decay daughters. The DCA of the V^0 to the primary vertex is determined by extrapolating the reconstructed V^0 particle's momentum vector backward toward the primary vertex. If the trajectory is within a certain window, it is accepted. This trajectory backwards does not always lead directly back to the primary vertex. The angle between the displacement vector from the PV to the V^0 and the momentum vector of the V^0 is called the pointing angle. The smaller the angle, the more likely the V^0 particle originated at the primary vertex. The mass tolerance is the acceptable mass range for the V^0. Two decay daughter candidates can pass all the previous selection criteria and still not reconstruct into the proper V^0 mass.

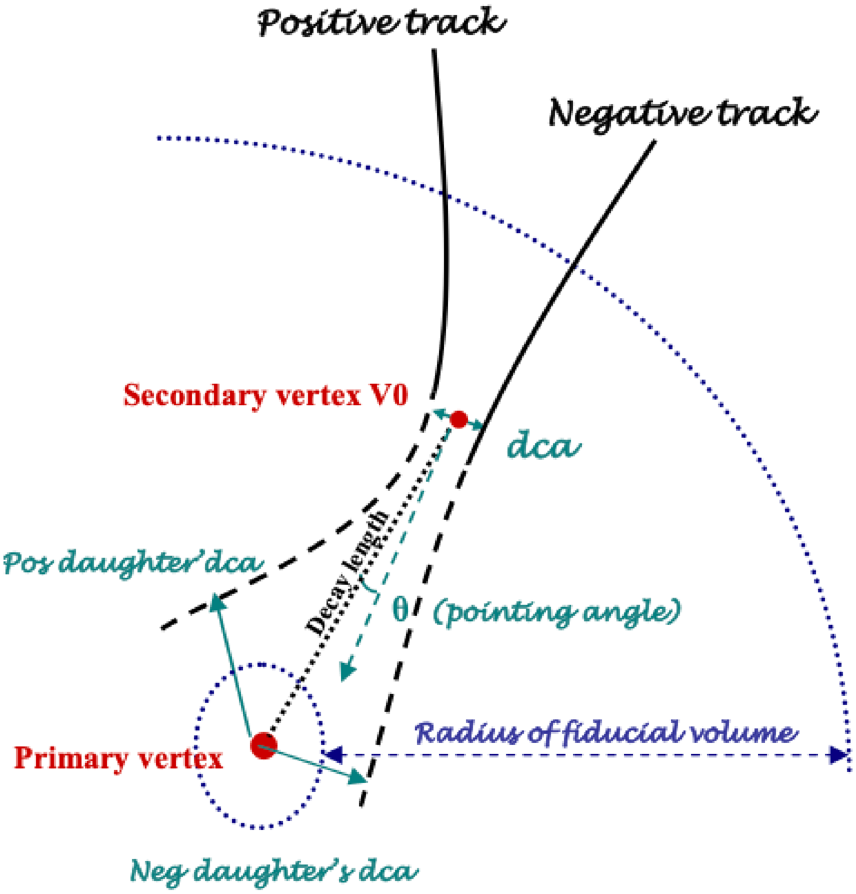

Figure 4.1: Topology of a V^0 decay [53].

4.1.5 Resonance Selection

One difficult aspect of the P_s is that not only is the P_s a resonance itself, but five of its decay channels in this analysis are also resonances themselves. As mentioned in Section 1.4, resonances are unstable, extremely short lived particles that decay strongly and conserve quantum numbers including quark content. As opposed to V^0 particles that decay weakly away from the primary vertex, resonances decay so quickly that they essentially decay at the primary vertex. This means that the decay daughters of a resonance appear to be formed during the collisions and originate at the primary vertex. This means that the track selection and topological cuts for resonance daughters are the exact same as for primary particles (see Table 2).

Resonance Selection	**Selection Criteria**
Pseudorapidity	$\|\eta\| < 0.8$
ϕ Mass, m_ϕ	$1.010 < m_\phi < 1.030$ GeV/c^2
$\Sigma^{*\pm}$ Mass, m_{Σ^*}	$1.346 < m_{\Sigma^*} < 1.427$ GeV/c^2
$K^{*\pm}$ and K^{*0} Mass, m_{K^*}	$0.841 < m_{K^*} < 0.943$ GeV/c^2

Table 4: Criteria used to select resonance candidates.

The pseudorapidity range for a resonance remains the same as all other particles in this section. Since the daughter track selection and cuts are the same and there is no secondary vertex, a mass tolerance for each resonance candidate can be set. As mentioned in Sec. 1.4, the lifetime of a resonance is related to the FWHM (full-width half-max, Γ) of the resonance. Namely, the longer lifetime a resonance has, the narrower the mass peak we would expect to observe. Conversely, the shorter the lifetime a resonance has, the wider the mass peak. This means that, for different resonances with different lifetimes, different mass tolerances need to be set. The standard range used for this analysis for Σ^* and K^* is the mass of the resonance $\pm\ \Gamma$. The Γ values for Σ^{*+} and Σ^{*-} are 36.2 MeV/c^2 and 39.4 MeV/c^2. The Γ values for K^{*+} and K^{*-} are both 51.4 MeV/c^2 and the Γ for K^{*0} is 47.3 MeV/c^2. With these resonances being rare and having wider widths, this comes with a considerable amount of background. For the ϕ meson, due to its small width of $\Gamma =$ 4.4 MeV/c^2 and lower background, the range that is used is the mass of $\phi \pm 2\Gamma$.

The selections and cuts for daughter resonances are very important, but one important aspect to remember is that the P_s state that is being reconstructed is also a resonance itself. The last few sections have gone over the ways to determine the selection for the daughters, but the only selection cut that is directly on the P_s itself is a cut on pseudorapidity, $|\eta| < 0.5$. Every decay daughter in every reconstruction can have a pseudorapidity of $|\eta| < 0.8$ in order to have higher statistics, but the P_s itself must reconstruct at mid-rapidity. Doing this enables the results to be easily compared to the Thermal FIST predictions that have input yields for particles over one unit of rapidity at mid-rapidity.

4.1.6 Invariant Mass Technique

When it comes to reconstruction of particles, the invariant mass plot is the most important tool. Not all particles can be directly detected by the ALICE detectors, but information such as mass, momentum, and possibly even quark content (depending on the decay type) can be carried by the particle's decay daughters. If the daughter particles can be sufficiently detected, then the mother particle can be reconstructed to determine some of its properties. The mass of a reconstructed particle can be found from the following derivation

$$E^2 = m^2 + \vec{p}^{\,2} \tag{34}$$

$$E^2 = (E_1 + E_2)^2 = E_1^2 + E_2^2 + 2E_1E_2 \tag{35}$$

$$M^2 + (\vec{p}_1 + \vec{p}_2)^2 = m_1^2 + \vec{p}_1^{\,2} + m_2^2 + \vec{p}_2^{\,2} + 2E_1E_2 \tag{36}$$

$$M^2 = m_1^2 + m_2^2 + 2(E_1E_2 - \vec{p}_1 \cdot \vec{p}_2), \tag{37}$$

where the subscripts 1 and 2 represent the two decay daughter particles, M is the mass of the mother particle to be reconstructed, E is the total energy of each daughter particle, and p is the momentum of each daughter particle. It should also be noted that natural units are used, setting the speed of light, c, equal to 1.

In collider experiments that accelerate particles to near the speed of light, the collisions produce particles that are highly relativistic. Most of the energy is carried in the momentum of the particles and in colliders the calculated momentum to be used is transverse momentum. With this information, equation 37 can be redefined to

$$M^2 = 2p_{T_1}p_{T_2}(cosh(\eta_1 - \eta_2) - cos(\phi_1 - \phi_2)) \tag{38}$$

where p_T is a daughter particle transverse momentum, η is the pseudorapidity for a daughter particle, and ϕ is the azimuthal angle for a daughter particle. Invariant mass plots are very important for the discovery of particles that have never been measured.

4.2 Combinatorial Background

The invariant mass plot is a great tool to access information about reconstructed particles that decay into daughters that can be detected. But not all daughter particle candidates will reconstruct to a mother particle. As shown in Fig. 4.2, the vast majority, if not all, daughter particles do not reconstruct into a mother particle, but into a smooth curve which is called the combinatorial background.

The combinatorial background is comprised of all the daughter particles that matched all the selection criteria and cuts but still do not reconstruct into a true particle. The P_s is a resonance, which means that it decays very close to the primary vertex. Distinguishing between a proton that comes from the P_S and a proton that is formed from the collision itself or from the decay of a different resonance is almost impossible. The same idea applies for the ϕ meson as well, as the kaons that are the daughters may come from any number of sources. This also applies to all of the decay daughters from each channel being analyzed in this dissertation. For this reason, a large background is expected for each invariant mass plot created.

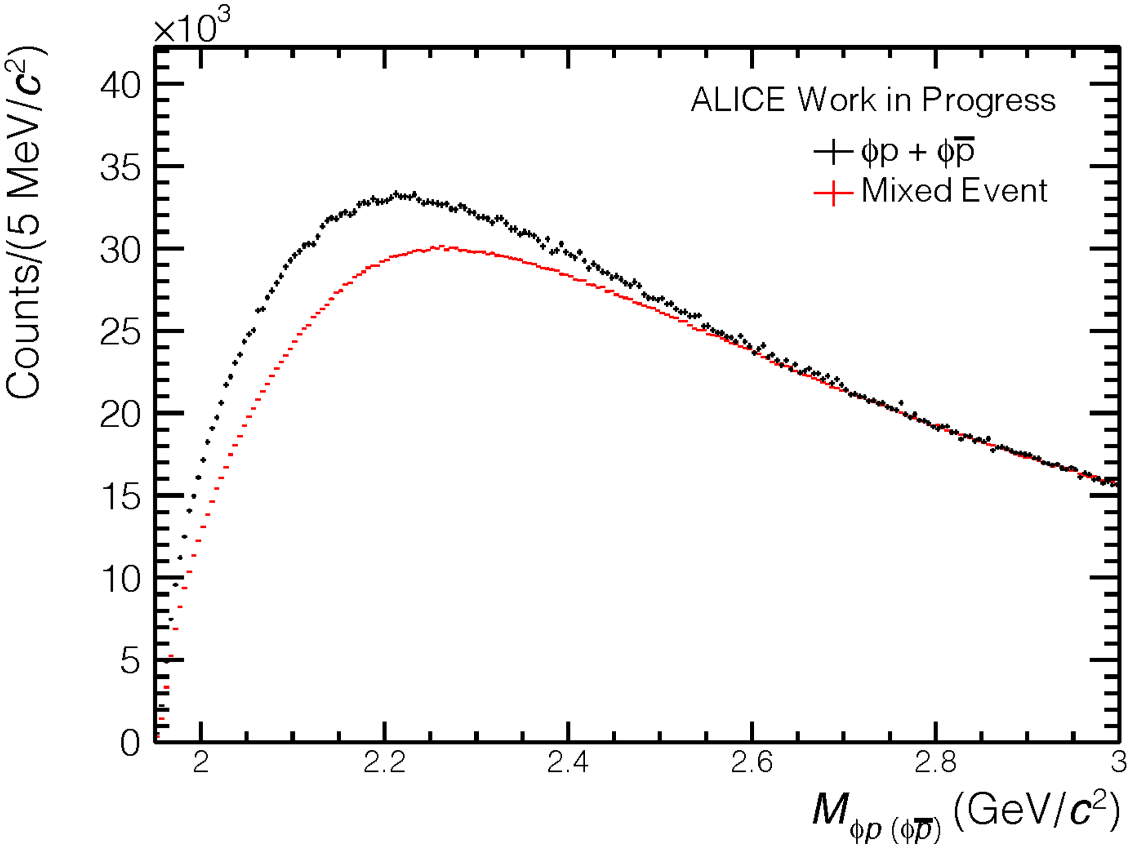

Figure 4.2: Invariant mass plot for $P_s \to \phi p$ in minimum bias pp $\sqrt{s} = 13$ TeV data. Black data points show the raw signal distribution while the red data point show the mixed-event background distribution normalized in the mass region of $2.8 < M_{P_s} < 2.83$ GeV/c^2.

If no apparent pentaquark signal is observed, a method to remove the combinatorial background is implemented to help resolve any pentaquark signal in the distribution. This is implemented to estimate the amount of background in the “raw signal”, which is shown in black in Fig. 4.2. One method to estimate the background is to create a “mixed-event” background, where one daughter candidate from one event is matched with the other daughter candidate from an entirely different event in order to reconstruct a pentaquark. This method allows for a background distribution to be created without any signal from a true pentaquark as well as without any sources of uncorrelated background.

The mixed-event background distribution was created by pairing uncorrelated decay daughters from 10 different events in pp collisions. Events that are selected for the mixing process have similar selection cuts to ensure that both daughters come from events with similar structure and minimize distortions due to different acceptances. The mixed-events must have a V_z within 1 cm from the initial event and the mixed-event must be within 5% of the multiplicity percentile of the initial event. The mixed-event distribution will be more likely to represent a true distribution of the daughter particles and less likely to represent a random distribution of particles simply by having the two events be similar to each other in multiplicity and position of V_z. The number of events used in event-mixing needs to be enough to be sufficient to show no correlation between the two daughter particles in question, but not large enough as to use a large amount of computational resources that would take large amounts of time and memory. The mixed-event background distribution for $P_s \rightarrow \phi$p can be seen in the red data points in Fig. 4.2.

The mixed-event background technique is used in this analysis, but another type of combinatorial background method that was considered is a "same-event" background distribution. As an example, this analysis is searching for a P_s that can be reconstructed from $\Sigma^{*-} + K^{+}$, or the anti-particle case of $\overline{\Sigma}^{*+} + K^{-}$. It should be reasonable to assume that reconstructing $\Sigma^{*-} + K^{-}$ or $\overline{\Sigma}^{*+} + K^{+}$ should not reconstruct into a P_s, but produce a distribution that does not contain any P_s states at all. One problem with this technique for this analysis is that the nature of the P_s is completely unknown, so this type of "background" may actually contain a P_s that is unknown at the time. The background distribution needs to be uncorrelated and that is not something that can be said about this same-event distribution at this time.

Also, it should be noted that this same-event distribution method would not work for all channels in this analysis. The raw signal is a combination of particle plus antiparticle, in order to increase potential signal statistics. Particles like the ϕ meson and K^0_S are both neutral and both their own antiparticles, so switching the charge of the other daughter particles just gives the signal distribution of the anti-P_s which is already accounted for in the raw signal. The mixed-event technique works for all decay channels in this analysis.

4.2.1 Background Subtraction

Once the combinatorial background has been properly estimated using the mixed-event technique, further steps are taken to extract any potential P_s signal. This process is done to remove as much of the contribution from the combinatorial background to the raw signal as possible in order to observe any peaks, if they exist, and determine their properties.

Due to the fact that the mixed-event technique uses 10 mixed events for every one initial event, the mixed-event distribution needs to be scaled down considerably. With the increased statistics on the mixed-event distribution, the entire background distribution will be well above the raw signal produced from the same event decay daughters. The mixed-event distribution needs to be normalized to the raw signal distribution in a mass range away from any expected signal, to make sure the normalization does not interfere with any potential signal extraction. The mixed-event distribution in Fig. 4.2 is normalized to match the integral of the raw signal in the mass region of $2.8 < M_{P_s} < 2.83$ GeV/c^2.

Once the mixed-event background distribution is normalized to the raw signal, it can be subtracted to leave what should only be correlated particles. It is clear to see in Fig. 4.2 that the raw signal and the mixed-event background do not have the same shape when normalized. After background subtraction, a considerable amount of "residual background" is observed, especially in the lower mass region.

4.2.2 Residual Background

Although background estimation techniques seek to remove all non-true pairs of decay daughters from the raw signal distribution, this is almost never the case. It is clear in this case that, after subtracting the mixed-event background, there is still a residual background that needs to be accounted for.

This residual background may occur for several reasons, one reason being that long range correlations between strange particles in the same event can not be captured while using the mixed-event method. A distribution with a residual background is common for many ALICE resonance

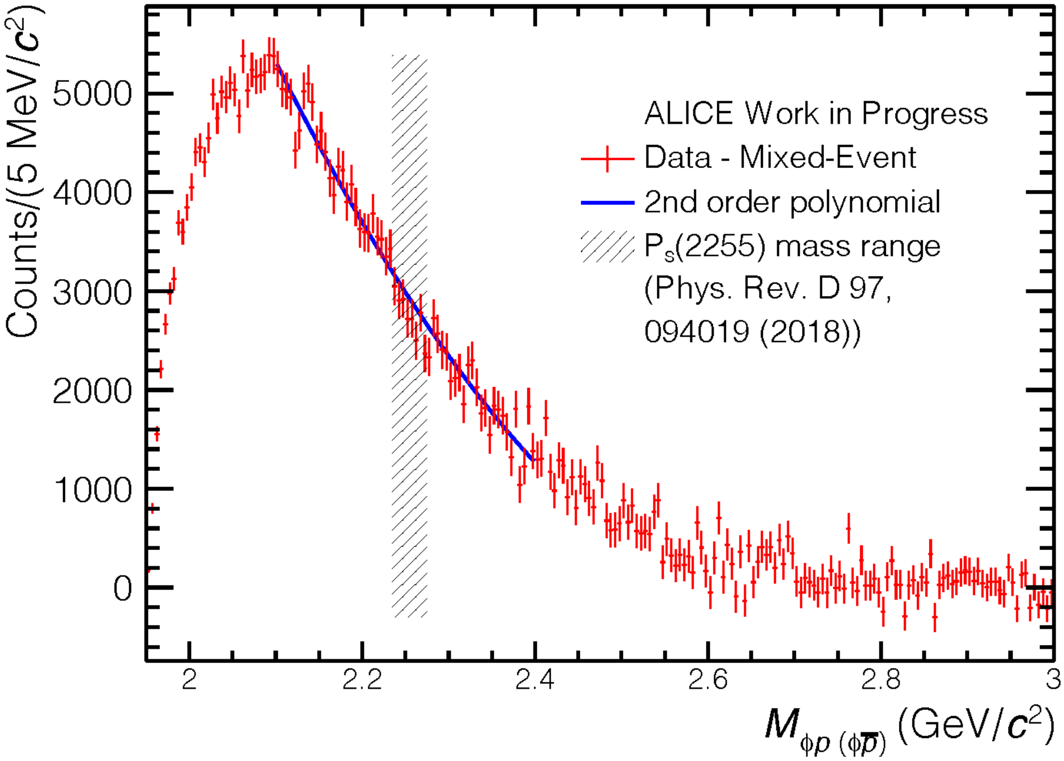

Figure 4.3: Residual background distribution for $P_s \rightarrow \phi p$ after mixed-event background subtraction. 2nd degree polynomial fit to range 2.1 - 2.4 GeV/c^2 is shown in blue, while the pentaquark mass range from theory in shown in the shaded region.

analyses [55][56][57]. It should be noted that not only is the normalization of the mixed-event background distribution sufficiently far away from any predicted mass peak, but it is also chosen to be in a range such that after subtraction the distribution will not have negative counts.

The residual background is typically described by the fit of a second degree polynomial in a range that is near the mass peak [56][57]. The residual background, minus the predicted P$_s$ signal region (M$_{P_s}$ ± 20 MeV/c^2), is fit with a second degree polynomial. The signal region is excluded to ensure that the polynomial fit only takes into account the background and not any of the actual signal if one exists. This excluded range is chosen to be equivalent to the hypothetical range of a P$_s$ signal that spans 2Γ (FWHM of 20 MeV/c^2 for a narrow resonance) and is centered at the theoretical mass prediction. Looking at Fig. 4.2, subtracting the red mixed-event distribution from the black raw signal produces the residual background distribution seen in Fig. 4.3. The blue curve is the second degree polynomial fit from 2.1 - 2.4 GeV/c^2.

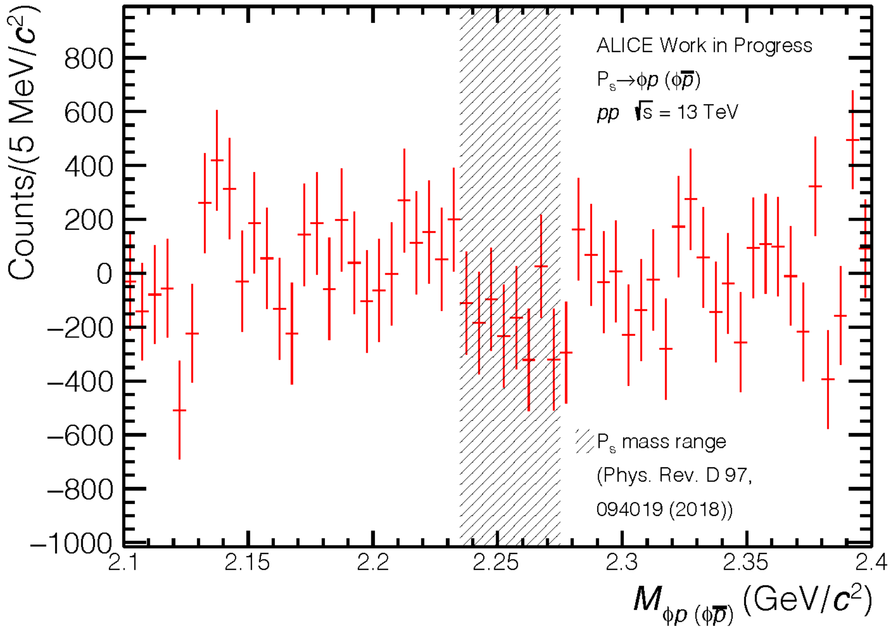

Figure 4.4: Invariant mass plot for $P_s \to \phi p$ after mixed-event and polynomial subtraction. The shaded region shows the predicted P_s mass range from theory [47]. Statistical errors are approximately ±200

.

After the second degree polynomial is selected and fit to the necessary range of the residual background, the polynomial can then be subtracted from the residual background, resulting in a distribution that only contains the signal with no background. The result of this subtraction can be seen in Fig. 4.4. The invariant mass plot without any background shows a flat distribution that is centered around zero in the range of 2.1 - 2.4 GeV/c^2. The shaded region indicates the expected signal range of the P_s from theoretical predictions [47]. No apparent pentaquark signal is observed for the $P_s \to \phi p$ channel. Fig. 4.4 also shows a bit of waviness in the distribution that center around zero and is mostly caught by the statistical errors. Based on raw yield estimates from Ch. 7.1.2, the spread counts including statistical errors from -600 to 600 only cover about 23% of the predicted pentaquark yield.

5 Data Corrections

ALICE and other detectors have shown amazing capabilities to identify particles that come from collisions and many of their properties with great precision. However, every experiment has limitations to its capabilities. As shown in Fig. 5.1, the ALICE detectors do not cover the entire span of possible particle tracks. Similarly, no one detector can completely cover the range of p_T used for this experiment.

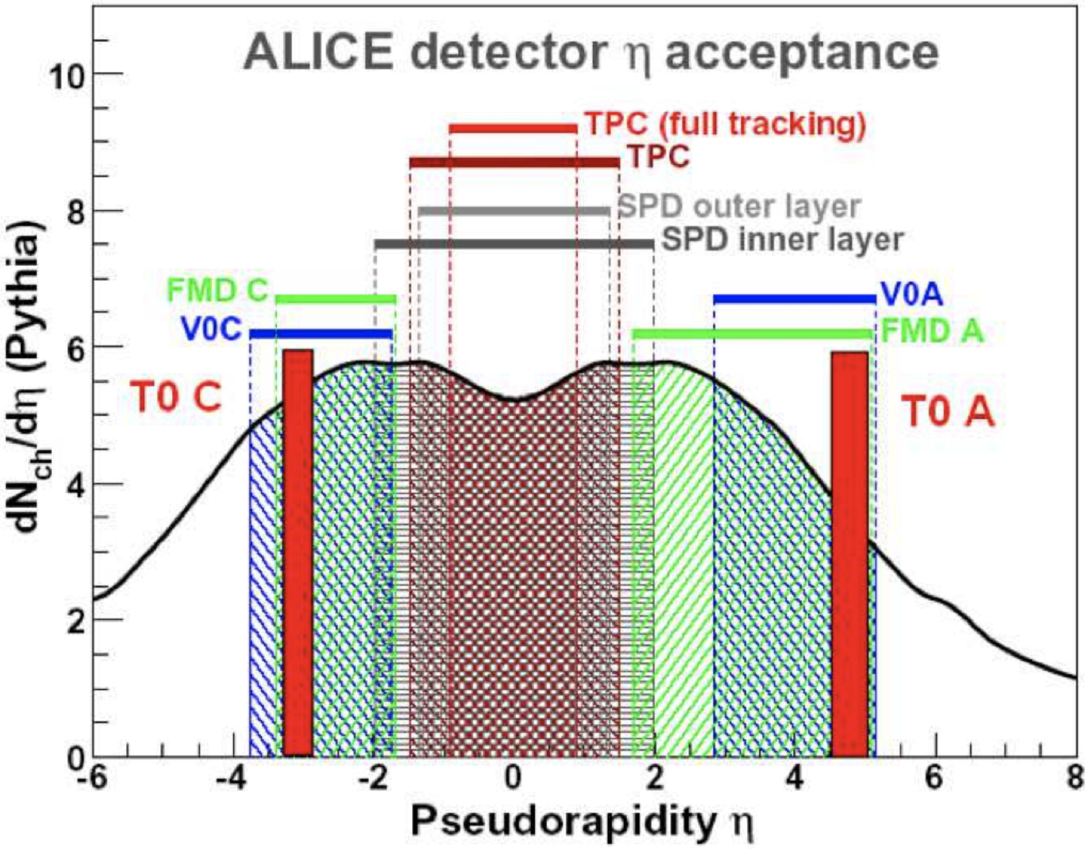

Figure 5.1: Acceptance coverages in pseudorapidity η for various ALICE detectors. Pythia event generator predictions for dN$_{ch}$/dη vs η in pp collisions at $\sqrt{s} = 14$ TeV [58].

Any total yield calculation will have to be corrected for the geometric limitations of the detectors. After a collision, there is a contingent of particle tracks that do not fall within the physical range of the detectors that need to be accounted for. This correction factor is known as "acceptance" and can be calculated using a Monte Carlo simulation study. This acceptance correction also takes into account rapidity cuts and the secondary decays of particles used to reconstruct the resonances used in this analysis.

Like any experiment, there is a possibility that not every particle in a collision can be tracked, properly identified, or reconstructed using the ALICE detectors, even if the number of produced particles is known. Another correction factor, known as "efficiency", is used to account for this reality and is calculated using a Monte Carlo simulation study. Both "acceptance" and "efficiency" are calculated at the same time. The product of "acceptance x efficiency" (a x ϵ) will be determined and used for this analysis.

5.1 Efficiency Corrections

5.1.1 Monte Carlo Set

In order to obtain numerical values for acceptance and efficiency, a Monte Carlo simulation needs to be performed. There are two primary event generators used by ALICE to simulate high energy collisions and their theoretical dynamics. Heavy Ion Jet Interaction Generator (HIJING) is an event generator typically used to simulate A+A collisions (Pb-Pb collisions at ALICE). The collision system used in this analysis is pp collisions, so instead of HIJING, the event generator that was used is called PYTHIA8. PHYTIA8 can be used to simulate hadron-hadron or lepton-lepton collisions with center of mass energies of 10 GeV $< \sqrt{s} <$ 100 TeV [65]. While PYTHIA8 is used to simulate events for physical experiments like the LHC, it still needs a set of parameters and variables in order to properly describe the existing models and data. Monash2013 provides a list of constraints for PYTHIA8 that effectively "tunes" the simulations to help match previous results obtained by the experimental setup [66].

The DPGSIM, which is an important piece of code used for simulations at ALICE, is a steering script from the ALICE software package that takes generator parameters like run number, collision energy, system size, detector configuration, and other parameters to set up a complete Monte Carlo simulation. The simulation also includes an option to have "injected" particles into a simulated event. Some particles, like rare resonances or even the P$_s$, are not produced in great enough numbers to have their properties studied. Injecting a particle into a simulated event will help increase the statistics needed to further study that particle's properties. P$_s$ states are generated with different masses (2.255 and 2.065 MeV/c^2), a width (Γ = 100 GeV/c^2), decay channels, and other properties that match the theoretical predictions. Each P$_s$ state and its anti-particle are injected into each simulated pp collisions to ensure that there are enough P$_s$ statistics for analysis.

A computer package known as GEANT3 (Geometry And Tracking) is used to model the ALICE detectors with realistic descriptions of detector interactions and responses. The Monte Carlo simulation for pp $\sqrt{s} = 13$ TeV data was constructed using the DPGSIM event generator with the PYTHIA8 Monash2013 package as well as the GEANT3 package. The injected pentaquarks were injected with a flat p_T distribution in the range $1 < p_T < 10$ GeV/c in order to increase statistics for higher p_T values. The pentaquarks were injected with a pseudorapidity of $|\eta| < 0.5$ to match the same acceptance window of the Thermal FIST input yields as well as the reconstructions from real data in this analysis. A sample of approximately 10 million minimum bias events were simulated to compute the corrections needed for this analysis.

The main purpose of the Monte Carlo simulation is to determine the acceptance and efficiency for the yields of the P$_s$ for each predicted decay channel. The acceptance and efficiency are calculated by determining the ratio of reconstructed pentaquarks in the simulation to generated pentaquarks in the simulation. This value needs to be determined in order to correct yield calculations to be able to make comparisons of the experimental yield as determined by ALICE to theoretical yield predictions.

5.1.2 Efficiency Correction Procedure

The fraction of generated pentaquarks that are reconstructed after passing through the Monte Carlo simulation outlined is the product of acceptance and efficiency. These injected pentaquarks are subject to the same track cuts, PID, topological cuts, and pair cuts used for the analysis with real data. The formula for acceptance x efficiency is simply put as

$$a \text{ x } \epsilon_{\text{rec}} = \frac{\text{reconstructed}}{\text{generated}} \tag{39}$$

where a x ϵ^{rec} is shorthand for acceptance x efficiency, “generated” is the number of pentaquarks that are injected into the simulation and “reconstructed” is the number of pentaquarks that the simulation was able to detect properly using the same cuts and selections used for real data. If every injected pentaquark is able to be reconstructed, then a x ϵ_{rec} would be 1, whereas if no injected pentaquarks are able to be detected, the a x ϵ_{rec} would be 0.

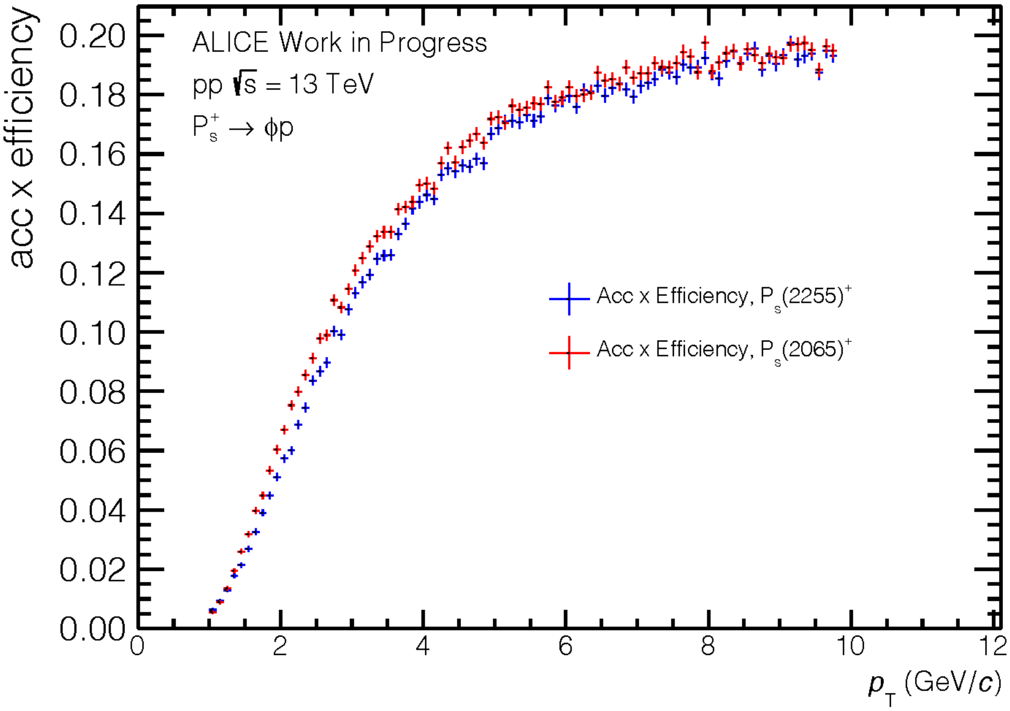

Figure 5.2: Acceptance x Efficiency for both $P_s(2065)$ in red and $P_s(2255)$ in blue as a function of p_T for $P_s \to \phi p$ for minimum bias pp at $\sqrt{s} = 13$ TeV using Monte Carlo simulations.

It is very important to understand how a x ϵ_{rec} changes as a function of p_T. Looking at Fig. 5.2, it can be seen that a x ϵ_{rec} increases starting from 0 at 1 GeV/c to a maximum near 0.20 at higher p_T for both $P_s(2065)$ and $P_s(2255)$. This plot also shows relatively small efficiency differences between the mass states but much larger efficiency differences between values of p_T, especially at lower p_T.

Fig. 5.3 shows an a x ϵ_{rec} plot projected onto the mass axis for $1.0 < p_T < 10.0$ GeV/c and fit with a linear polynomial. The linear polynomial seems to match the trend of the a x ϵ_{rec} very well. The constant of the polynomial, p0, can be interpreted as the mean value of a x ϵ_{rec}, while the slope, p1, represents the mass dependence of the a x ϵ_{rec}. Standard error propagation for division of a subset is used for the statistical uncertainties of the a x ϵ_{rec} distributions.

Comparing Fig. 5.2 to Fig. 5.3, it can be seen that a x ϵ_{rec} varies significantly with p_T while changing very little with mass. For this reason, establishing a p_T spectrum for the P_s is necessary in order to find a proper average a x ϵ_{rec}.

5.1.3 Acceptance Correction Procedure

Since no signal is observed from the invariant mass distributions, no p_T spectrum can be extracted from the data for the P_s. The MC generated pentaquarks were injected with a flat p_T spectrum, as seen in Fig. 5.5. This flat spectrum is not physical. Therefore, it is necessary to reweight the simulated pentaquarks with a realistic p_T spectrum. This spectrum will help with determining an accurate average a x ϵ_{rec} as well as help describe the yield from p_T ranges where the ALICE detector has no acceptance such as $0 < p_T < 1$ GeV/c.

There is no measured p_T spectrum for the P_s, the spectrum shape must be estimated from previously measured spectra from another particle species. The standard function used to determine the shape of a p_T spectrum for pp collisions at $\sqrt{s} = 13$ TeV is the Levy-Tsallis function, which

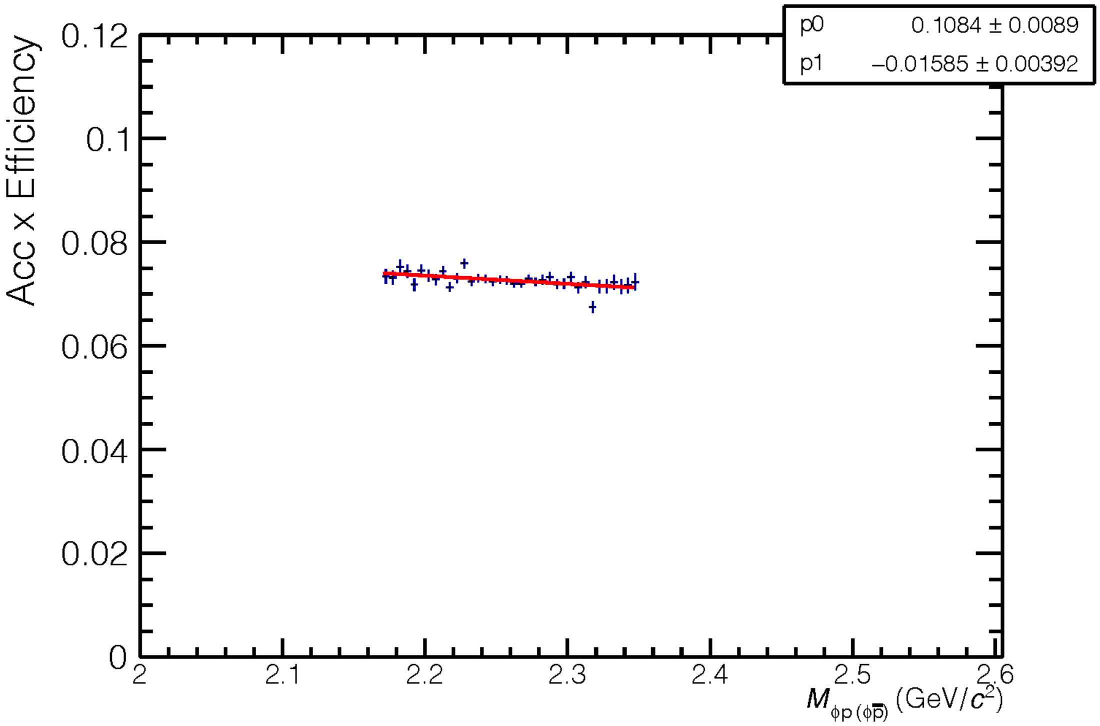

Figure 5.3: Acceptance x Efficiency as a function of Mass for pp collisions at $\sqrt{s}$ = 13 TeV, $1.0 < p_T < 10.0$ GeV/c

has the form

$$f(M, p_T, n, C, norm) = p_T \times \frac{norm(n-1)(n-2)}{nC(nC + M(n-2))}\left[1 + \frac{\sqrt{p_T^2 + M^2} - M}{nC}\right]^{-n} \tag{40}$$

where n and C are fitting parameters and $norm$ is the normalization constant [59].

As seen in Eq. 40, the Levy-Tsallis functional form is dependent on M, the mass of the particle. Particles with similar mass tend to have similar shaped p_T spectra. Choosing a known particle p_T spectrum for a particle that is close in mass, then scaling the mass parameter to the mass of the P_s will scale the p_T spectrum to a form that can be used for the P_s. The p_T spectrum for the $\Omega + \bar{\Omega}$ was chosen due to the mass of 1.672 GeV/c^2, it has a well studied p_T spectrum, and it contains strange quarks. The $\Omega + \bar{\Omega}$ p_T data (black points) and the Levy-Tsallis fit (blue) can be seen in Fig. 5.4 [60].

In order to scale this Levy-Tsallis fit for use with a pentaquark, the fitting parameters for the Ω distribution are fixed. The parameters n, C, and $norm$ are known from published results and fixed, while the mass term is changed and fixed to the pentaquark mass. This fit can be seen in Fig. 5.4 in magenta. This distribution is an estimate of the p_T spectrum for the P_s that will be used to reweight the generated and reconstructed pentaquarks from the Monte Carlo simulation.

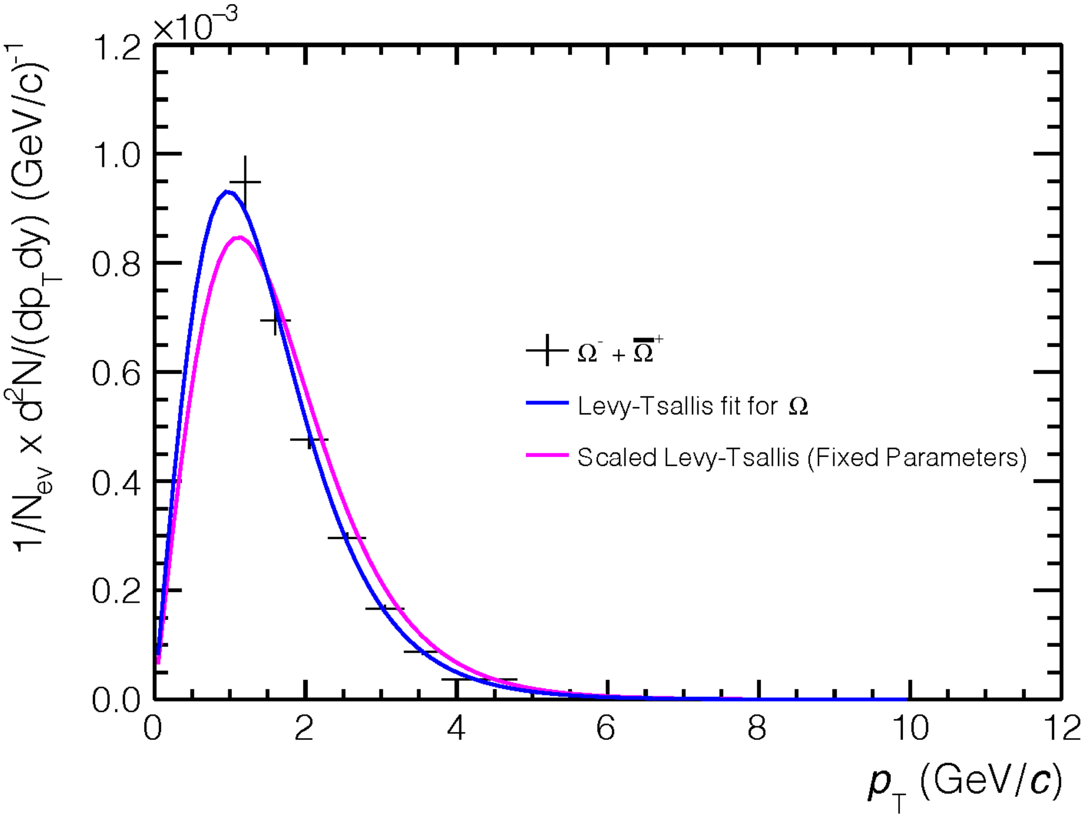

Figure 5.4: Levy-Tsallis fits for minimum bias p_T spectrum of $\Omega+\bar{\Omega}$ in blue and for the mass scaled P_s p_T spectrum in magenta [60].

As previously mentioned, the MC injected p_T spectrum for the P_s is a flat distribution from $1.0 < p_T < 10.0$ GeV/c. In order to get an accurate accounting of the full reweighted MC generated spectrum, the MC generated distribution was filled in for the p_T range of 0 - 1.0 GeV/c. The assumption was made that pentaquarks with $p_T < 1.0$ GeV/c will not be reconstructed. This will not affect the a x ϵ_{rec} vs p_T distribution seen in Fig. 5.2, but it will affect the average efficiency after reweighting, which will be explained later. Fig. 5.5 shows the MC generated pentaquarks in the open black circles and the MC reconstructed pentaquarks in the open red circles. Dividing the MC reconstructed by the MC generated creates the blue distribution seen in Fig. 5.2. Both of these distributions need to be reweighted by the scaled Levy-Tsallis fit seen in magenta in Fig. 5.4 and Fig. 5.5. This will give the generated and reconstructed distributions a more realistic shape that can be used to find an average a x ϵ_{rec} vs p_T.

Both the MC generated and the MC reconstructed pentaquarks were scaled by the same Levy-Tsallis function, so whether you construct the a x ϵ_{rec} vs p_T before or after reweighting does not matter, the resulting distribution will be the same. However, these distributions can be used to find an average a x ϵ_{rec} over a specific p_T range. This can be done with the equation

$$\langle\epsilon\rangle = \frac{\sum Reweighted\ \ MC\ \ Reconstructed}{\sum Reweighted\ \ MC\ \ Generated} \tag{41}$$

where $\langle\epsilon\rangle$ is the average a x ϵ_{rec} over a given range of p_T. Since we assumed that no pentaquarks could be reconstructed if $p_T < 1.0$ GeV/c, the full p_T range used to determine $\langle\epsilon\rangle$ is from 0 - 10 GeV/c. Even though we do not reconstruct any pentaquarks below 1.0 GeV/c, there are most certainly pentaquarks that are created within that p_T range. This is the reason for extending the MC generated p_T spectrum down to zero in Fig. 5.5, to get a proper accounting and scaling of the generated pentaquarks in this region.

Results for the $\langle\epsilon\rangle$ calculations can be seen in Fig. 5.6 as the red horizontal lines. For $P_s \to \phi p$ and a mass of 2255 MeV/c^2, the average efficiency for $0 < p_T < 10$ GeV/c is calculated to be ~3.96%. This value is in line with other ALICE analyses of exotic particles with strange quarks, such as the H-Dibaryon and $\overline{\Lambda n}$ [61]. Not all average efficiencies are on the order of a few percent, as particles like Σ^* and K^* are more rare than Λ and K so they have more total decay daughters to

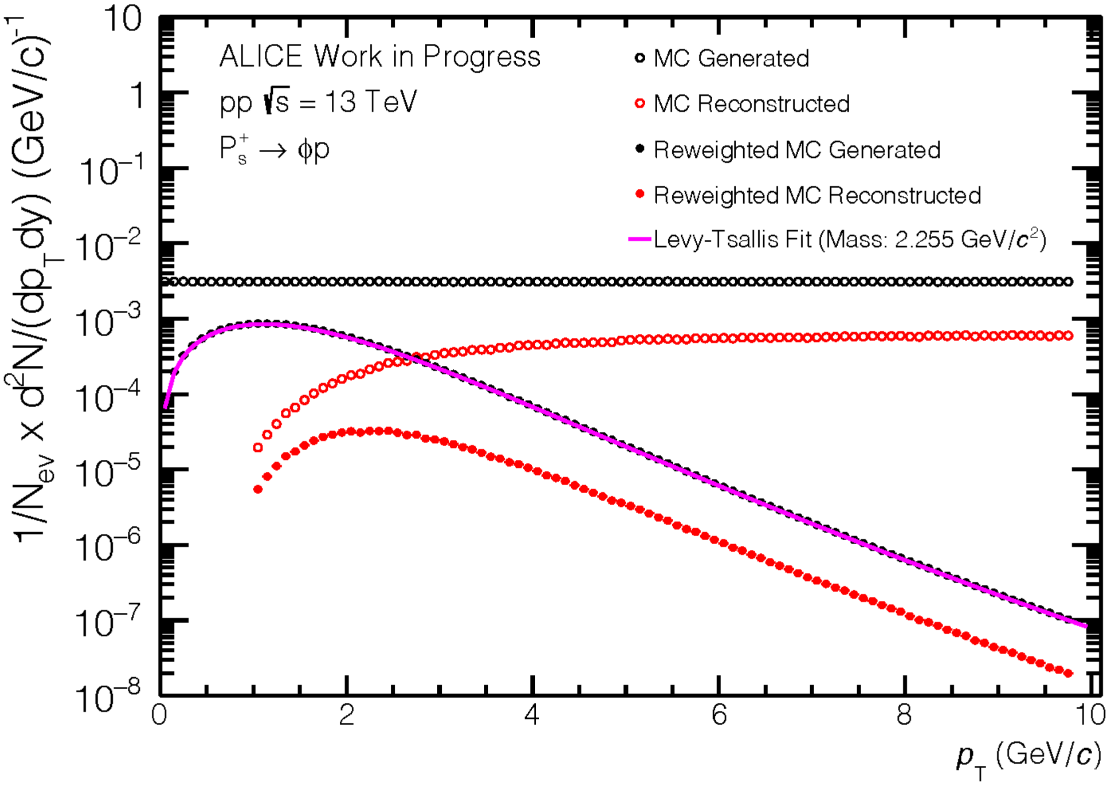

Figure 5.5: The injected (MC generated) P_s states are shown from 0 to 10 GeV/c in open black circles, and scaled by the Levy-Tsallis fit to form the reweighted MC generated distribution in closed black circles. The MC reconstructed P_s states in red open circles are also scaled to for the reweighted MC reconstructed distribution in closed red circles.

reconstruct, which will in turn give lower efficiencies. Fig. 5.6 also shows the efficiency distribution and average efficiency for $P_s \rightarrow K^{*+}\Lambda$, which is significantly lower at $\langle\epsilon\rangle = 0.2655\%$. The efficiencies for each decay channel with both analyzed masses can be seen in Table 5. These values will be used to correct the upper limits to the yields for each decay channel.

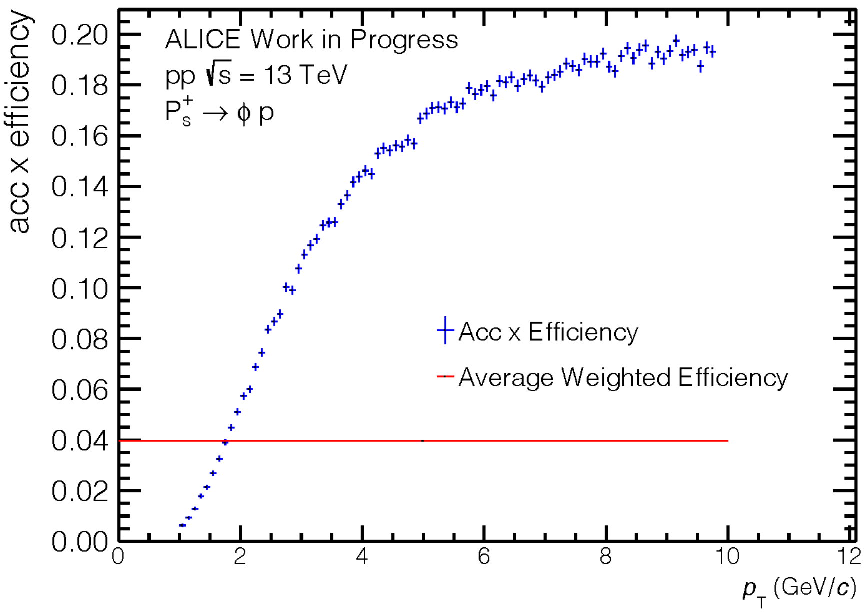

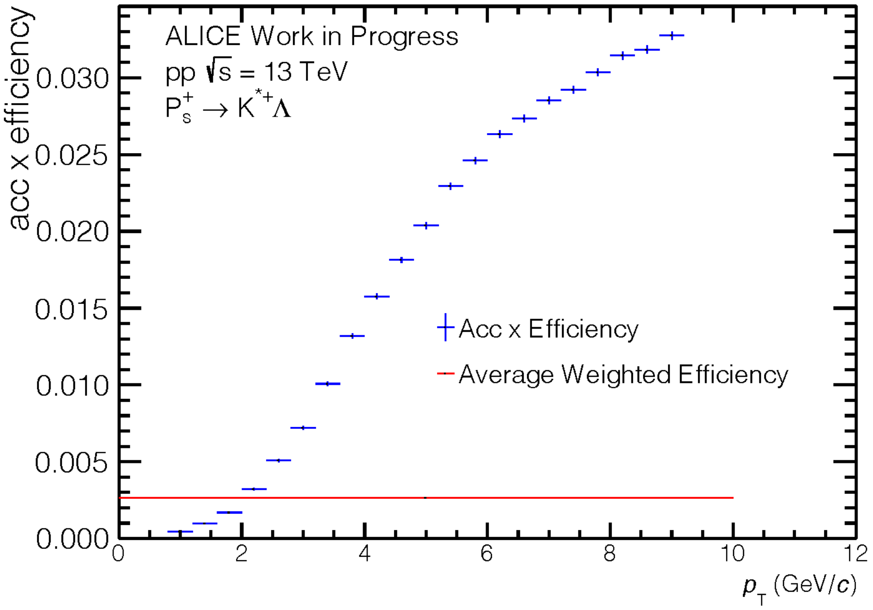

Figure 5.6: Acceptance x Efficiency vs p_T for (top) P$_s$(2255) → ϕp with the average efficiency, $\langle\epsilon\rangle$, shown in red and acceptance x efficiency vs p_T for (bottom) P$_s$(2255) → $K^{*+}\Lambda$ with the average efficiency in red.

Decay Channel	Avg. Eff. %(2255)	Avg. Eff. %(2065)
ϕp	3.9645	4.1848
$K^+\Sigma^{*-}$	2.2463	2.2753
$K_S^0\Sigma^{*+}$	0.8888	0.8987
$K^{*+}\Lambda$	0.2655	-
$K^{*0}\Lambda$	1.5386	-
$K^+\Lambda$	5.4062	5.2995
$K_S^0\Lambda$	1.8226	1.8053

Table 5: Average efficiencies for each channel at both masses of 2065 MeV/c^2 and 2255 MeV/c^2.

Using a Levy-Tsallis function to fit a p_T spectrum may be the standard, but to account for systematic uncertainties, other fit functions may be used. The Boltzmann function, described by the equation

$$\frac{d^2N}{dydp_T} = p_T\frac{dN}{dy}m_Te^{\frac{-m_T}{T}}, \tag{42}$$

where T is the temperature of the blackbody used to produce the observed spectra, and m_T is the transverse mass $\left(\sqrt{p_T^2+m^2}\right)$, can also be used. Another function that can be used for systematics is the m_T exponential function. This function is given by the form

$$12\pi \times p_T \times norm \times e^{\frac{-m_T}{T}}, \tag{43}$$

where $norm$ is the normalization constant and T is the freeze out temperature.

The last function that is used in this analysis for systematic uncertainties is the Boltzmann-Gibbs Blast-Wave function, which is described by the form

$$r \times m_T \times I_0\left(\frac{p_T\mathrm{sinh}(\mathrm{arctanh}(\beta_{\mathrm{max}}\mathrm{r}^{\mathrm{n}}))}{T}\right) \times K_1\left(\frac{m_T\mathrm{cosh}(\mathrm{arctanh}(\beta_{\mathrm{max}}\mathrm{r}^{\mathrm{n}}))}{T}\right) \tag{44}$$

where r is the radius, β_{max} is the magnitude of the velocity, T is the freeze out temperature and n is a parameter for the shape of the velocity profile. I_0 and K_1 are modified Bessel functions. By assuming that all particles move radially outward from the collision point with a common velocity profile, the Boltzmann-Gibbs Blast-Wave function attempts to recreate radial flow.

6 Error Analysis

Each experimental measurement in this analysis is associated with two different types of uncertainties: statistical uncertainties, which deal with procedures to estimate the uncertainty of calculations due to statistical limits and fit procedures, and systematic uncertainties, which deal with the procedures to estimate the uncertainty of calculations due to the specific procedure used in calculating values or fits.

6.1 Statistical Uncertainty

When searching for a rare particle, a large amount of statistics is needed, which makes the statistical uncertainties rather large. For a counting experiment such as this, the statistical uncertainties for each produced invariant mass plot follow as $\sigma_i = \sqrt{N}$, with σ_i being the uncertainty in a particular bin and N being the number of counts in that bin. As an example, if a bin contains 10,000 counts, then the statistical uncertainty would be $\sqrt{10,000} = 100$.

The mixed-event background distribution is constructed to have nearly 10 times more counts than the raw data invariant mass histograms. This leads to a statistical error of $\sqrt{10}$ times more per bin than the raw data histograms. After the mixed-event background is normalized to the raw data background, each data point in the mixed-event background is normalized by the same factor. This normalization factor is roughly 1/10, leading the total statistical error for each bin in the mixed-event background to be $\sqrt{10}/10$ times lower than the raw data statistical error.

When subtracting the mixed-event background from the raw data distribution, the bin contents subtract normally, but the errors follow the formula

$$\sigma_{Data-Mixed} = \sqrt{\sigma_{data}^2 + \sigma_{mixed}^2}. \tag{45}$$

The errors do not simply add or subtract, but are added in quadrature. The residual background fit also needs to be subtracted and its statistical errors accounted for. The error associated with the fit is taken care of with the Integral Error function in ROOT. The integral is computed by counting the value of each bin in the span of the fit, then the error of this total integral value is computed and divided by the bin width. This error is then propagated to each bin by summing in quadrature. These statistical errors are extremely important for attempting to observe a rare peak signal above background. Each pentaquark decay channel will have a different amount of statistics thus a different amount of statistical uncertainty after background is removed.

6.2 Systematic Uncertainty

In order to calculate systematic uncertainties, variation of possible permutations of the analysis need to be performed by using the exact same procedure to analyze the data, but changing a parameter of the analysis to see how that parameter affects the results. The variations can include changes to topological cuts, fitting procedures, signal extraction methods, as well as other variations. The process for calculating systematic uncertainties is as follows:

1. Use one set of parameters and cuts, with the lowest χ^2, for the analysis as the "default cut"
2. Calculate the deviation of the upper limit to the yield when one parameter is changed
3. In order to determine if the observed variation is due to systematic effects instead of statistical variation, a Barlow check is performed [54]
4. After considering all the different sources except the default cut, the total systematic uncertainty is the sum in quadrature of each systematic uncertainty.

The deviation from the default cut value represents the RMS caused by the selected parameter. The RMS is calculated with the equation

$$RMS = \sqrt{\frac{1}{N}\sum_{i=1}^{N}(X_i - Y)^2} \tag{46}$$

where N is the number of variations, Y is the default value, and X_i are the values from the different cut variations. For the *total* systematic uncertainty, all the maximum deviations are combined using the follow equation

$$SYS_{err} = \sqrt{\sum_{j} RMS_j^2} \tag{47}$$

where j is the number of systematic error sources.

The variations used in this analysis are as follows:

- As discussed in Section 2.4, the TPC is very good at identifying charged particles. Decay products of Λ and K_S^0 have a very loose 5σ cut for protons and pions, but the n_σ cuts for particles that are directly detected (charged pion, charged kaon, and (anti-)proton) can be a bit more flexible. These cuts can be set to match the standard cuts used in analyses for these particles. Also, these cuts can be tightened and loosened to compare to the default cuts. In order to determine the effect of the TPC $\mathrm{d}E/\mathrm{dx}$ selection for charged pions and charged kaons, the n_σ is varied from its initial default value of 2.0 to values of 1.5 and 2.5. The initial default value of n_σ for the protons of 5.0 is already significantly loose, so the tighter cut is set to a value of 3.0.

- Using the same idea for the TOF, the TOF can detect charged pions, charged kaons, and protons directly, without an overly loose cut. In order to determine the effect of the TOF selection for $\pi^{\pm}$, $K^{\pm}$, and protons, the n_σ is varied from its initial default value of 3.0 to 2.5 and 3.5.

- Values of the DCA from the primary vertex of the reconstructed primary particles were changed to determine its effect on the analysis. The initial cuts were designed to be loose to allow more reconstructed particles to be analyzed. Tightening this cut will reduce the amount of reconstructed particles, but it will also decrease the amount of misidentified reconstructed particles in the analysis. The Λ DCA cut is tightened from its initial default value of 0.4 cm to 0.2 cm, and the K_S^0 DCA cut is tightened from its initial default value of 0.3 cm to 0.15 cm.

- Values of the DCA of the daughter particles to their reconstructed mother particle were changed to determine its effect on the analysis. Tightening this cut will reduce the amount of reconstructed particles, but it will also decrease the amount of misidentified reconstructed particles in the analysis. The Λ daughter DCA cut and the K_S^0 daughter DCA cut are both tightened from their initial default value of 1.0 cm to 0.3 cm.

- The pointing angle is defined as the angle between a reconstructed particle displacement from the primary vertex and the direction of its momentum. If a particle is reconstructed, but it is determined that the direction the particle came from does not point toward the primary vertex, then we can infer that the particle did not originate from the primary vertex or the two daughter particle do not form a true mother particle. When the pointing angle is small, the cosine of this angle is 1, the closer the reconstructed particle is to coming from the primary vertex. The cosine of the pointing angle for the Λ is tightened from its initial default value of 0.99 to 0.995, while the cosine of the pointing angle for the K_S^0 is tightened from its initial default value of 0.97 to 0.995.

- Values of the DCA of the daughter particles to the xy plane were changed to determine its effect on the analysis. However, instead of decreasing the value of this DCA cut, this value is increased because it is set to a minimum distance away from the primary vertex. Increasing this DCA cut will cause candidates to need to be further away from the xy axis of the primary vertex in order to be used. Increasing the DCA of V^0 daughters to the xy plane value from its initial default value of 0.06 cm to 0.07 cm will decrease the number of candidates that can be identified as V^0 daughters.

- As previously mentioned, the unknown shape of the p_T spectrum can be modeled by different fit functions, which contributes to the systematic error. The default Levy-Tsallis fit was changed to Boltzmann, m_T exponential, and Boltzmann-Gibbs Blast Wave functions.

- The degree of the background polynomial when determining the estimated background function for the upper limit can be changed to observe its effect on the upper limit value. The 4th degree polynomial was chosen as the default due to having the best χ^2 value. Three polynomials were used to see the effect on the upper limit: 4th degree, 3rd degree, and 2nd degree.

6.3 Summary of Systematic Uncertainty Contributions

The following tables are a list of the sources of systematic uncertainty for the upper limit to the yield for each theoretical mass prediction for the P$_s$. The values listed in each table are calculated using fractional uncertainty, meaning each RMS value obtained from Eq. 46 is divided by the upper limit value obtained by the default cut and multiplied by 100. The total systematic uncertainty value shown at the bottom is not simply the sum each each systematic uncertainty, but the sum in quadrature of each systematic uncertainty, as described in Eq. 47. Entries with "N/A" denote that this cut does not apply to this channel. For example, the ϕp channel has no Λ or K^0_S particle in its decay, so topological cuts based on their decay topology are not applicable.

	P$_s$ (2065) Systematic Uncertainty (%)				
Source of Uncertainty	ϕp	$K^+\Sigma^{*-}$	$K^0_S\Sigma^{*+}$	$K^+\Lambda$	$K^0_S\Lambda$
Proton TPC n$_\sigma$	20.70	N/A	N/A	N/A	N/A
Kaon TPC n$_\sigma$	9.18	4.37	N/A	4.11	N/A
Pion TPC n$_\sigma$	N/A	1.68	3.28	N/A	N/A
Proton TOF n$_\sigma$	7.74	N/A	N/A	N/A	N/A
Kaon TOF n$_\sigma$	9.66	3.22	N/A	2.11	N/A
Pion TOF n$_\sigma$	N/A	1.68	2.18	N/A	N/A
Λ Daughter DCA	N/A	5.62	4.13	5.63	2.34
Λ DCA to PV	N/A	5.12	3.51	5.49	5.31
Λ Cosine of Pointing Angle	N/A	2.98	2.39	3.21	2.86
K^0_S Daughter DCA	N/A	N/A	6.11	N/A	2.79
K^0_S DCA to PV	N/A	N/A	5.02	N/A	4.92
K^0_S Cosine of Pointing Angle	N/A	N/A	2.82	N/A	1.04
DCA of V^0 daughters to PV xy axis	N/A	1.51	2.08	2.71	3.39
Background polynomial degree	2.47	1.70	1.95	0.60	2.14
p_T Shape Function	4.63	4.89	5.18	4.14	4.61
Total Systematic Uncertainty	26.33	11.47	12.49	10.85	10.59

Table 6: Systematic uncertainties for the upper limit for each P$_s$(2065) decay channel for minimum bias pp collisions at $\sqrt{s} = 13$ TeV.

Looking at both Table 6 and Table 7, it can be seen that the largest contribution to any systematic uncertainty is the proton TPC n$_\sigma$ cut being changed. The default TPC n$_\sigma$ cut used in this analysis for primary protons is a wide 5σ cut, and the varied nσ cut is 3σ. Going from a wide cut to a much smaller cut has a drastic affect on the upper limit to the yield. In contrast, the standard cut for both kaons and pions is 2σ with a varied cut of ± 0.5σ. It can also be seen that the higher mass P$_s$(2255) has a higher value for total systematic uncertainty than the lower mass P$_s$(2065) for each decay channel

Source of Uncertainty	P$_s$ (2255) Systematic Uncertainty (%)						
	ϕp	$K^+\Sigma^{*-}$	$K^0_S\Sigma^{*+}$	$K^{*+}\Lambda$	$K^{*0}\Lambda$	$K^+\Lambda$	$K^0_S\Lambda$
Proton TPC n$_\sigma$	24.00	N/A	N/A	N/A	N/A	N/A	N/A
Kaon TPC n$_\sigma$	9.60	4.64	N/A	N/A	5.17	4.60	N/A
Pion TPC n$_\sigma$	N/A	1.19	2.10	3.88	3.01	N/A	N/A
Proton TOF n$_\sigma$	9.39	N/A	N/A	N/A	N/A	N/A	N/A
Kaon TOF n$_\sigma$	2.32	2.83	N/A	N/A	4.56	4.11	N/A
Pion TOF n$_\sigma$	N/A	1.64	1.29	3.62	3.13	N/A	N/A
Λ Daughter DCA	N/A	6.89	5.82	7.16	8.06	6.08	2.18
Λ DCA to PV	N/A	7.17	3.42	5.36	6.50	6.30	2.65
Λ Cosine of Pointing Angle	N/A	5.39	1.59	6.55	5.16	3.01	2.60
K^0_S Daughter DCA	N/A	N/A	5.71	1.34	N/A	N/A	3.16
K^0_S DCA to PV	N/A	N/A	6.39	3.36	N/A	N/A	6.99
K^0_S Cosine of Pointing Angle	N/A	N/A	2.91	3.70	N/A	N/A	1.00
DCA of V^0 Daughters to PV xy axis	N/A	1.19	1.82	3.39	4.06	3.39	2.64
Background Polynomial Degree	1.00	0.93	0.12	1.77	1.98	0.23	0.31
p_T Shape Function	6.26	7.33	8.61	8.33	7.46	5.47	6.23
Total Systematic Uncertainty	27.59	14.75	14.61	16.18	16.62	15.50	11.14

Table 7: Systematic uncertainties for the upper limit for each P$_s$(2255) decay channel for minimum bias pp collisions at $\sqrt{s} = 13$ TeV.

7 Results

Through the techniques seen in Sec. 4.1.6, the invariant mass plots for seven different decay channels have been produced. The mass states that have been analyzed are $\mathrm{P}_s(2065)$ and $\mathrm{P}_s(2255)$. Each channel has an invariant mass distribution with a mixed-event background distribution that will be subtracted. This background subtracted distribution will then have a residual background that will need to be subtracted as well in order to extract a P_s signal. No signal was observed for any of the decay channels analyzed in this analysis, therefore an upper limit to the yield will be determined. The methodology describing how to obtain an upper limit to the yield for each channel is discussed in Sec. 7.2. The results of the upper limit to the yield calculations and their comparison to the thermal model of particle production is discussed in Sec. 7.3.

7.1 Invariant Mass Distributions

The raw invariant mass distributions for six of the seven channels are shown below with normalized mixed-event distributions. Each mixed-event distribution is normalized to the raw distribution in the range of $2.8 < M_{P_s} < 2.83$ GeV/c^2, except the $K_S^0\Lambda$ and the $K^+\Lambda$ channels, which are normalized at $2.35 < M_{P_s} < 2.38$ GeV/c^2. The range of the invariant mass plot for $K_S^0\Lambda$ and $K^+\Lambda$ does not extend as far as the other decay channels, due to the lower mass of the decay daughters. The distribution for $\mathrm{P}_s \to \phi p$ was already shown in Fig. 4.2 in Sec. 4.2 and will not be shown again in this section.

It is interesting to note that every mixed-event background distribution does not fully capture the shape of the raw invariant mass signal. It is also interesting to note that only one of the distributions, $K_S^0\Lambda$, shows any sort of peak behavior in its raw distribution. There are two small peak like structures around the masses of 1.690 GeV/c^2 and 1.820 GeV/c^2. These peaks are not in the mass range from theory that would allow us to think of them as pentaquark candidates, but they are most likely $\Xi(1690)^0$ and $\Xi(1820)^0$.

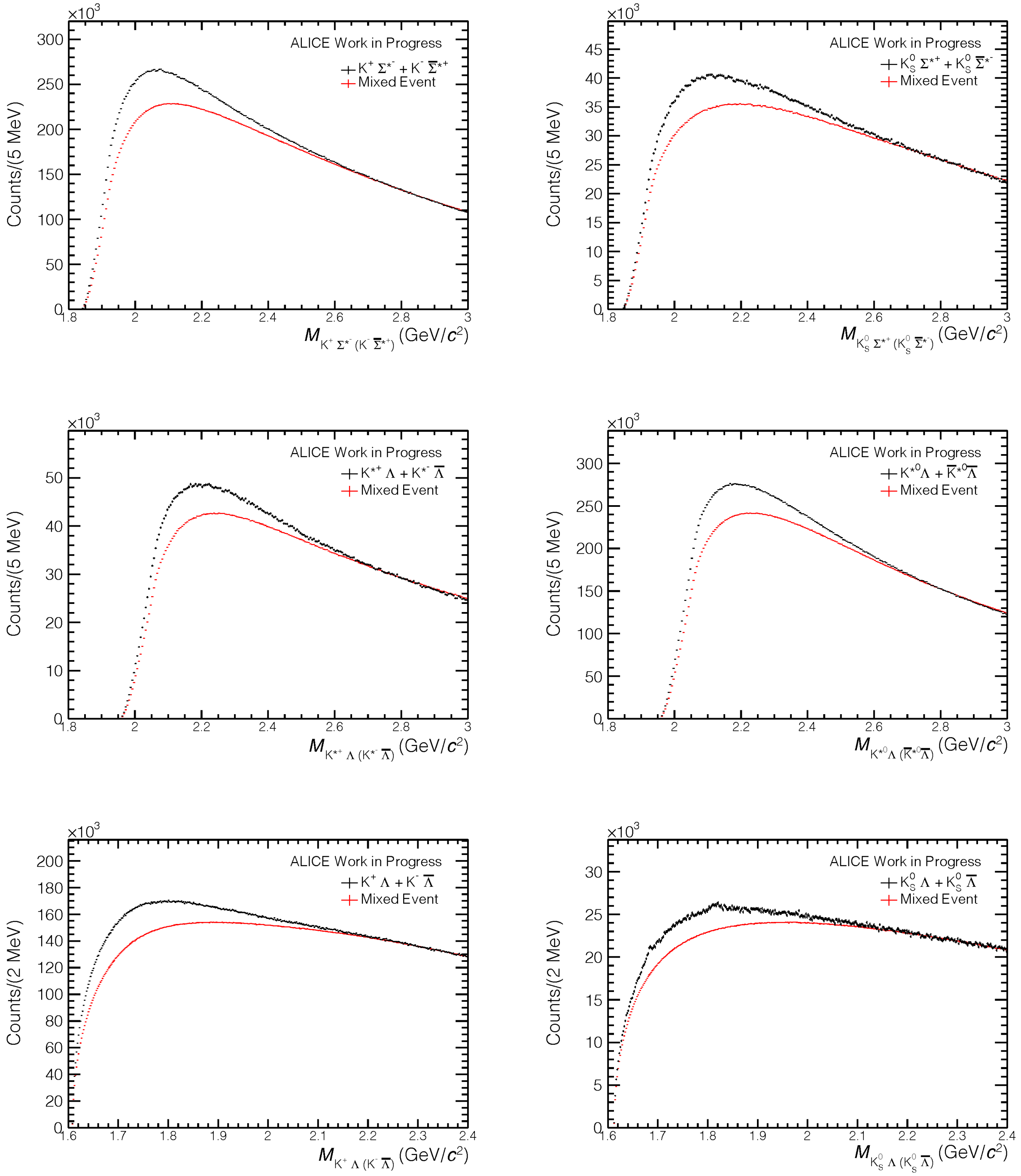

Figure 7.1: Invariant mass distributions for (top left) $K^+\Sigma^{*-}$, (top right) $K_S^0\Sigma^{*+}$, (middle left) $K^{*+}\Lambda$, (middle right) $K^{*0}\Lambda$, (bottom left) $K^+\Lambda$, and (bottom right) $K_S^0\Lambda$ from minimum bias pp collisions at $\sqrt{s} = 13$ TeV. Each distribution has its mixed-event background in red.

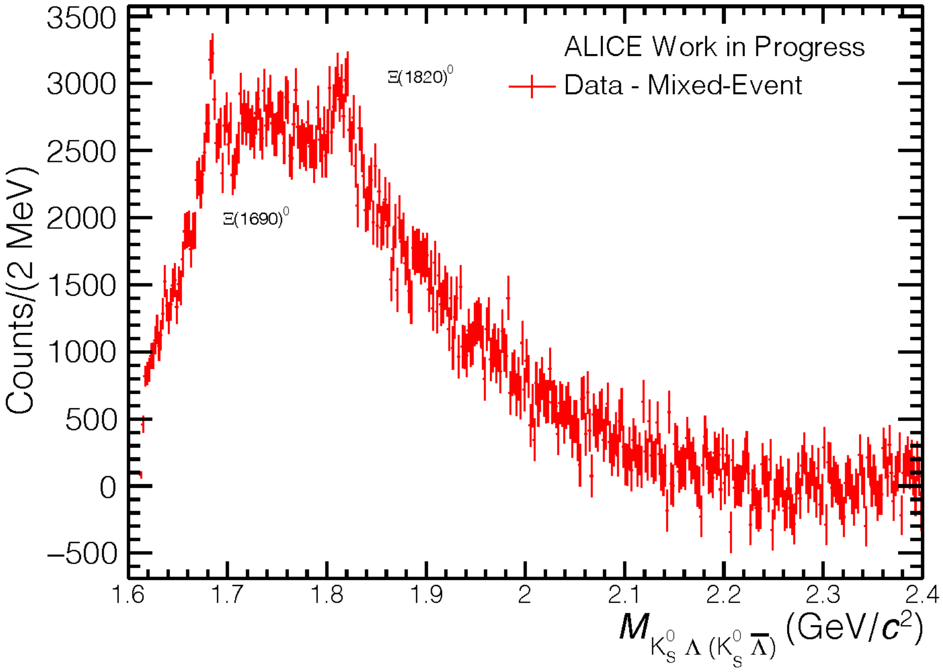

Figure 7.2: $K^0_S\Lambda$ signal is mixed-event background subtracted. Prominent peaks at 1690 and 1820 GeV/c^2 are seen.

Using the background subtraction techniques outlined in Sec. 4.2, these two peaks can be isolated as a check to see how well the techniques work. Subtracting the mixed-event background from the $K^0_S\Lambda$ raw signal distribution makes the peaks at 1690 and 1820 even more prominent and easier to see. This can be seen in Fig 7.2. Even though there is still a considerable amount of residual background leftover after mixed-event subtraction, the peaks are still very visible. Subtracting out the residual background separately for each peak leaves us with the distributions seen in Fig. 7.3. The peaks are still very visible and well above background fluctuations and statistical errors.

Although examining the peaks for more information about these particles is not the aim of this work, these states will prove interesting in the future as Ξ(1820)^0 has only briefly been studied by ALICE [5] with very little known about its properties. Even less is known about Ξ(1690)^0.

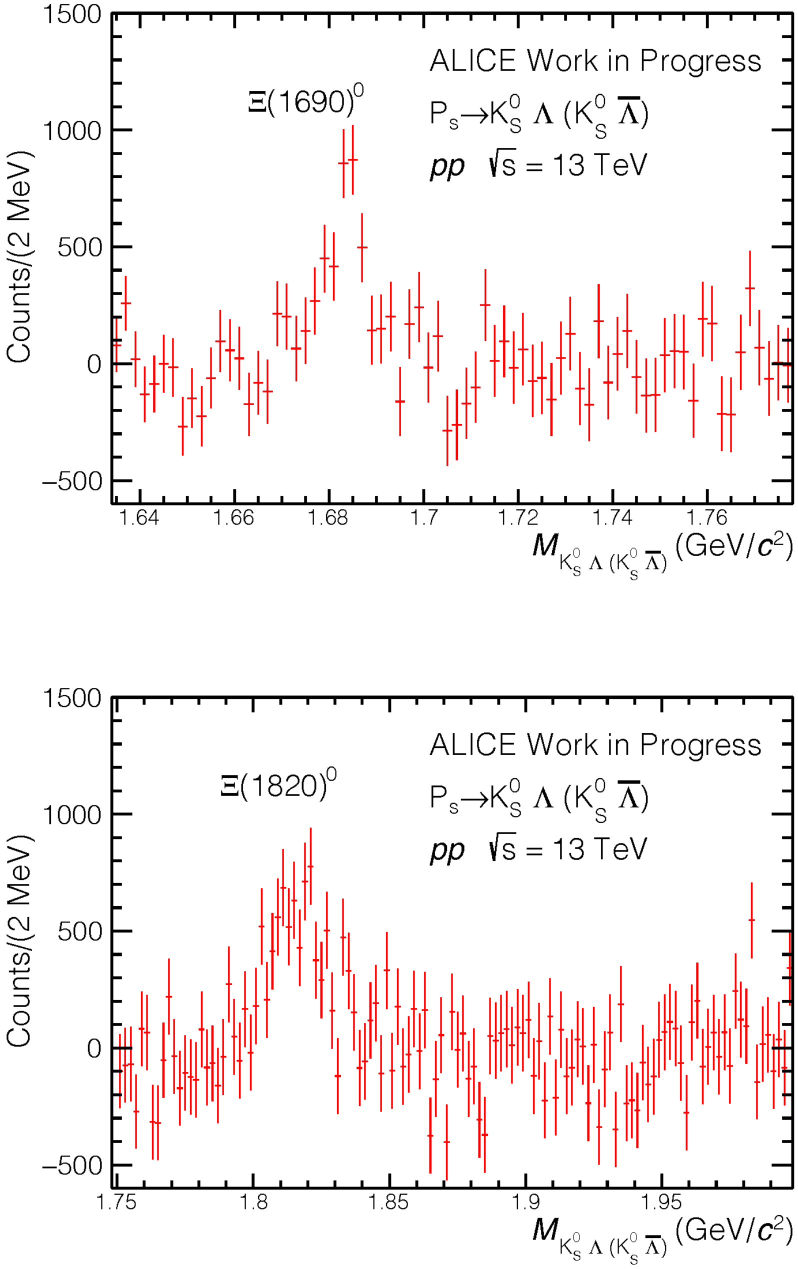

Figure 7.3: (top) The mass peak of $\Xi(1690)^0$ is visible and (bottom) the mass peak of $\Xi(1820)^0$ is visible in the invariant mass reconstruction of $K^0_S\Lambda$ in minimum bias pp collisions at $\sqrt{s} = 13$ TeV.

7.1.1 $\mathbf{P}_s$ Mass = 2065 MeV/c^2

The predictions for a P_s mass are centered around two different masses, 2065 and 2255 GeV/c^2. The invariant mass plots for the 2065 GeV/c^2 mass estimate are presented in this section.

The mass of 2065 GeV/c^2 is close to the kinematic limits for many of these decay channels, with the $K^{*0}\Lambda$ and $K^{*+}\Lambda$ channels having a combined daughter rest mass of 2011 MeV/c^2 and 2007 MeV/c^2, respectively [38]. The K^{*0} and K^{*+} both have widths (Γ) of greater than 40 MeV/c^2, leaving very little room from the kinematic limit, to the mass prediction of the P_s. The transition from the sharp rise in the invariant mass from kinematic limit to where it stabilizes is a difficult function to fit. Due to these facts, the channels $\mathrm{P}_s \rightarrow K^{*0}\Lambda$ and $\mathrm{P}_s \rightarrow K^{*+}\Lambda$ are not analyzed for the 2065 mass prediction.

Following along with the attempted signal extraction for the rest of the decay channels, using the invariant mass distributions and the mixed-event background distributions seen in Fig. 7.1, the background is subtracted from the data. The distribution of the data minus the background can be seen in red on each panel of Fig 7.4. A shaded blue region is added to show where the mass of the predicted pentaquark should be. A blue line indicates a second degree polynomial that will be used as an estimate of the residual background in the region of the pentaquark. The residual background fit is to span at least 4Γ above and below the mass estimate to make sure it encompasses a significant enough region outside the peak area, to capture the behavior of the background ($\Gamma = FWHM = 20\ MeV/c^2$ for this analysis). A span of 5Γ is used if the range encompassed does not pass the distribution maximum. The blue shaded region is not taken into account while fitting the polynomial, as to not bias any potential signal. The "upward" trend from the kinematic limit to the maximum tends to not show second order polynomial behavior.

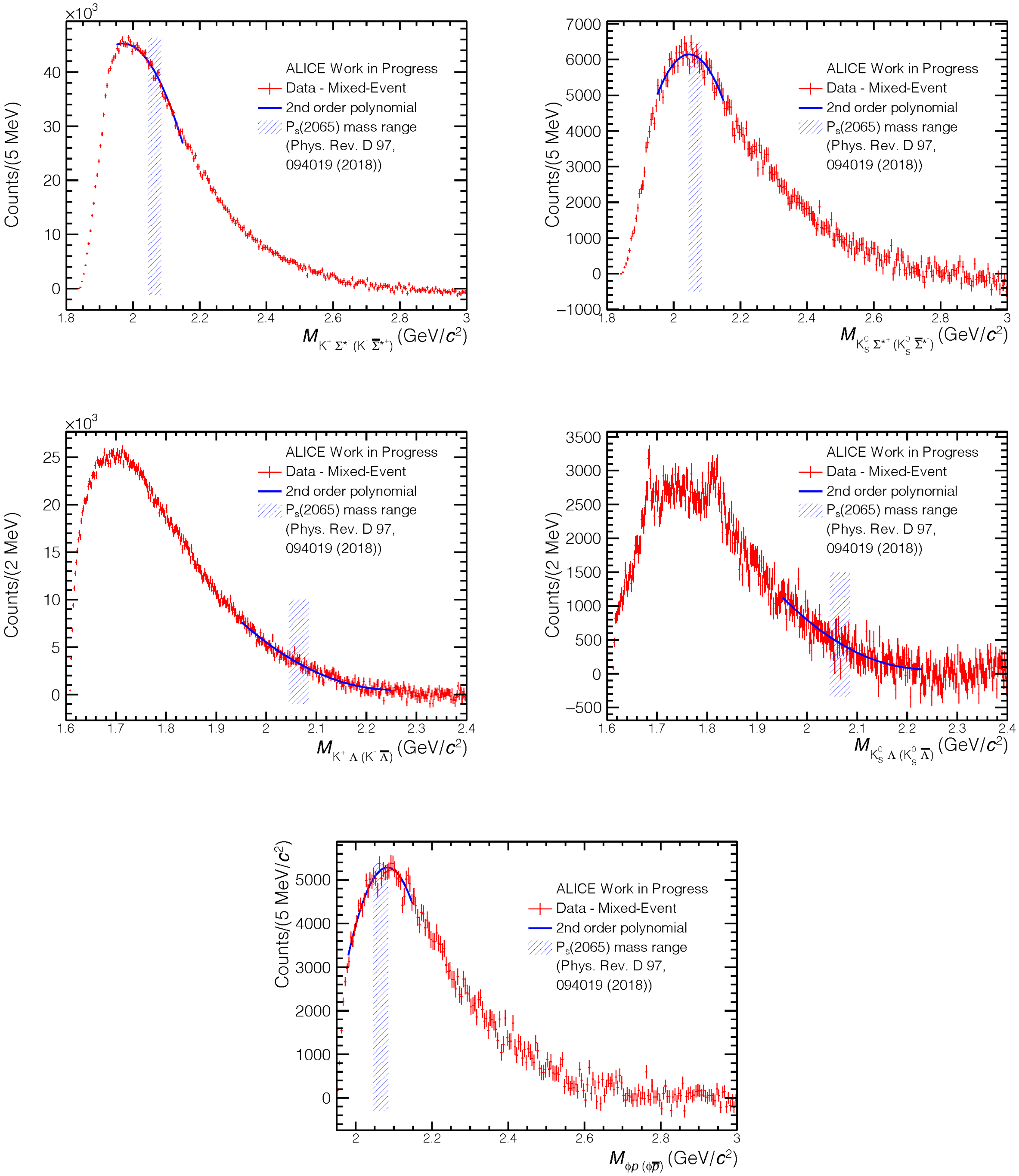

Figure 7.4: Mixed-Event background subtracted distributions for (top left) $K^{+}\Sigma^{*-}$, (top right) $K^{0}_{S}\Sigma^{*+}$, (middle left) $K^{+}\Lambda$, (middle right) $K^{0}_{S}\Lambda$, and (bottom) ϕp. Second degree polynomial fits are shown in blue for each distribution and a shaded blue region indicates the mass prediction region from theory [47].

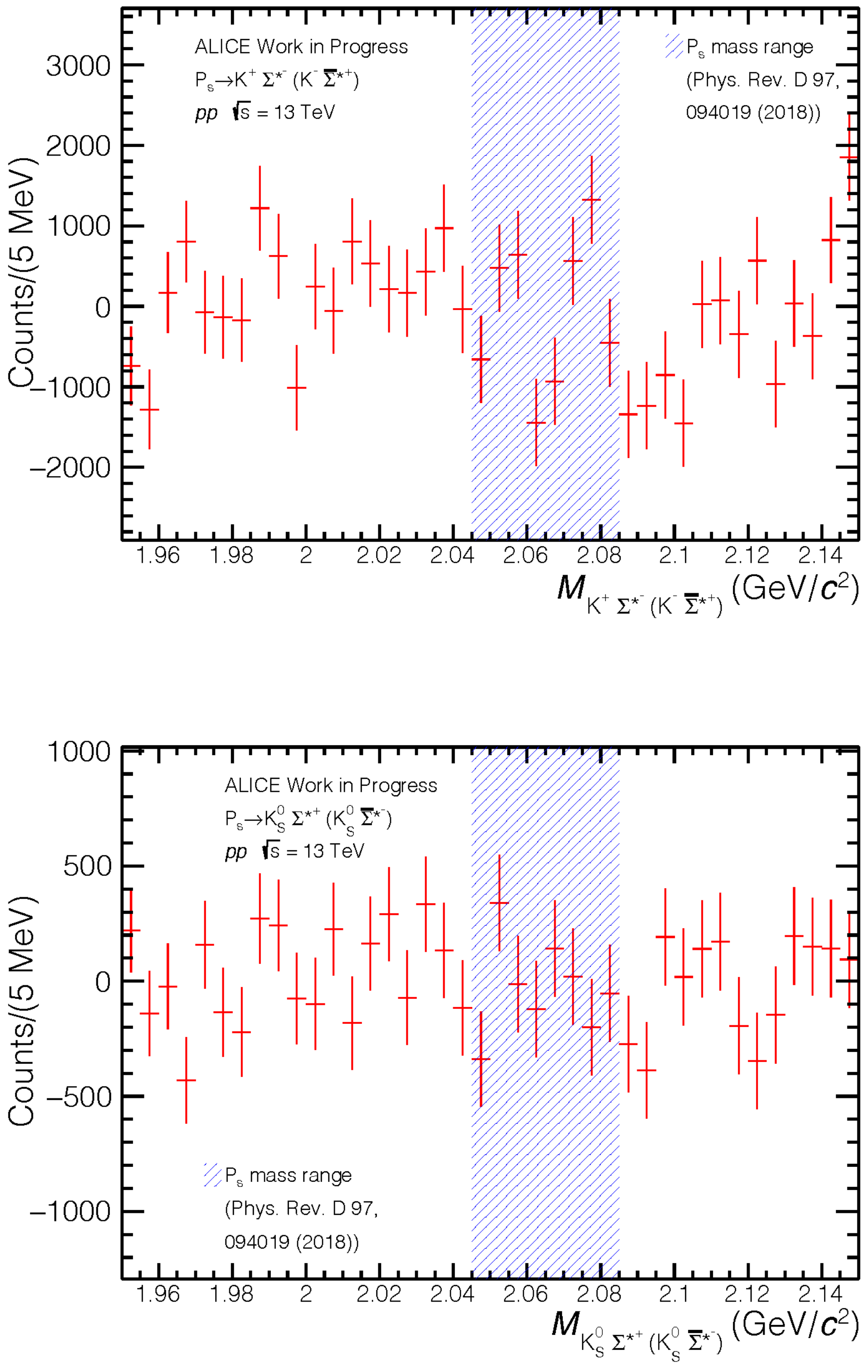

Figure 7.5: Residual background subtracted distributions for (top) $K^+\Sigma^{*-}$ and (bottom) $K^0_S\Sigma^{*+}$. The shaded blue region indicates the mass prediction region from theory [47]. No apparent peaks are observed.

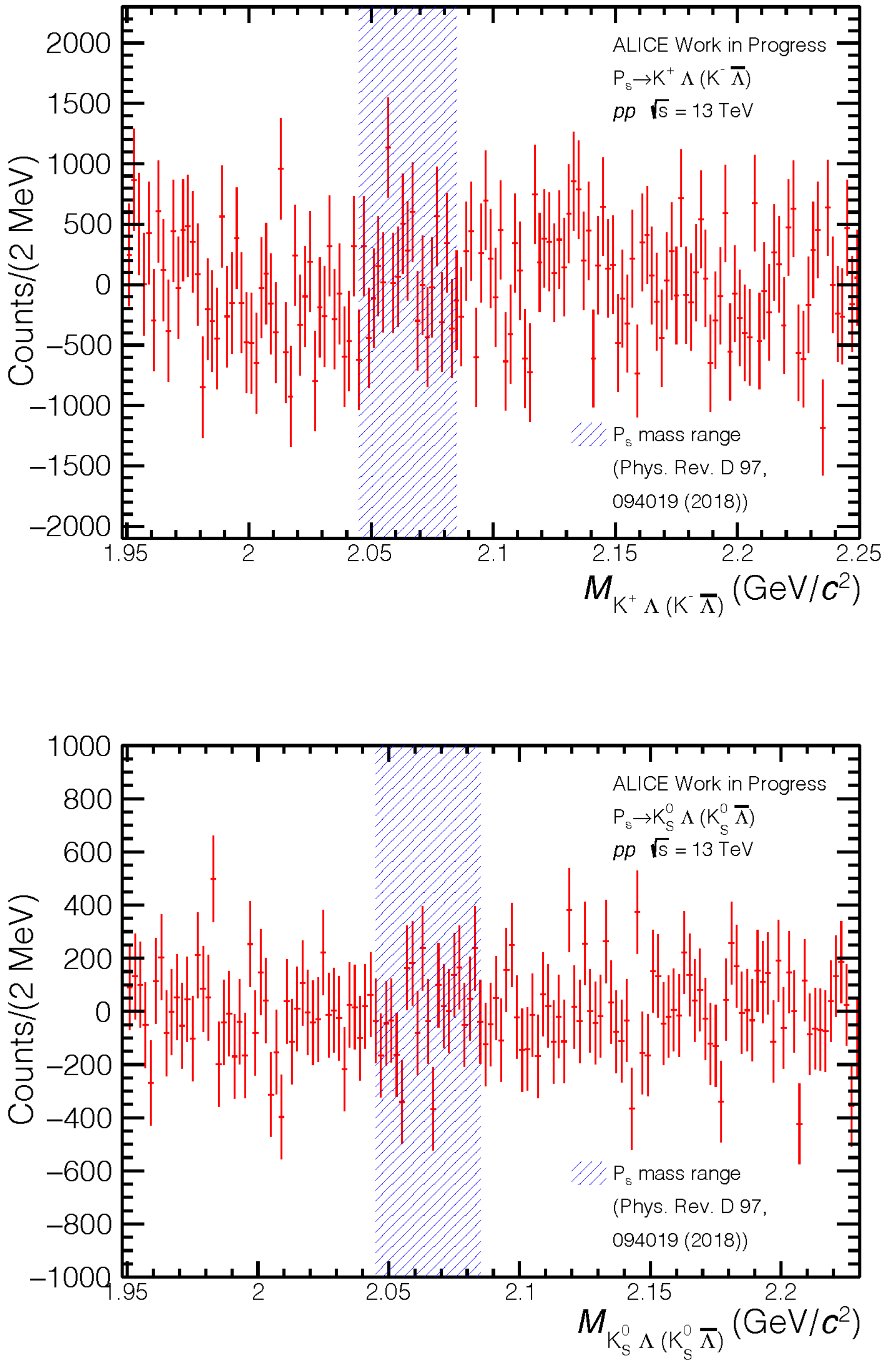

Figure 7.6: Residual background subtracted distributions for (top) $K^+\Lambda$ and (bottom) $K_S^0\Lambda$. The shaded blue region indicates the mass prediction region from theory [47]. No apparent peaks are observed.

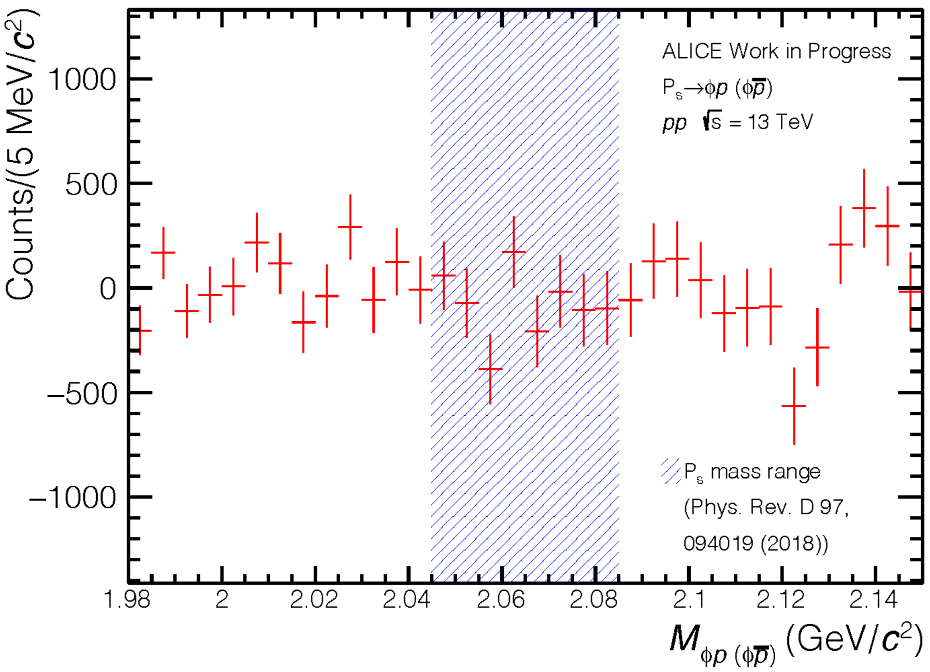

Figure 7.7: Residual background subtracted distribution for ϕp. The shaded blue region indicates the mass prediction region from theory [47]. No apparent peak is observed.

The residual background subtracted distributions are shown in Fig. 7.5, Fig. 7.6, and Fig. 7.7. The blue shaded region indicates the mass estimate from theory [47]. The background subtracted distributions in red center around zero with no peaked behavior well above background similar to what is observed in Fig 7.3. No $P_s(2065)$ peaks are observed for any of the decay channels in this analysis.

The amount of pentaquarks expected in this analysis based on Thermal FIST depends on a few factors. Different mass states will have different yield predictions. Efficiency and branching ratios of decay daughters for a P_s are driven by which particular decay channel the P_s follows. As an example, the expected number of $P_s(2065)$ candidates that we should see from the ϕp channel is determined by

$$N_{(P_s(2065))} = \underbrace{2.01 \cdot 10^9}_{\text{events}} \cdot \underbrace{0.0418}_{\text{efficiency}} \cdot \underbrace{0.491}_{\text{B.R. of } \phi} \cdot \underbrace{3.8318 \cdot 10^{-4}}_{\text{dN/dy from FIST}} \cdot \underbrace{1}_{\text{dy}} \approx 15,800. \tag{48}$$

The number of events is the number of collisions analyzed, the efficiency is shown in Table 5, the branching ratio is determined by the BR of the decay daughters, the dN/dy is the estimated yield prediction from Thermal FIST, and dy is the rapidity range of the reconstructed P$_s$ states, which is 1. Although the branching ratio of the P$_s$ itself is unknown and set to 100% for this analysis, the branching ratios of the decay daughters can be taken from the Particle Data Booklet [38].

It should be noted that decay channels with multiple decay daughters with branching ratios will have their branching ratios multiplied together. For example, for P$_s \rightarrow \Lambda K^0_S$, the Λ has a branching ratio of 63.9% and the K^0_S has a branching ratio of 69.2%, giving a total branching ratio of 44.2%. This is important because, although the P$_s$ decays into a particle than can be reconstructed, like a Λ, it only decays into the anticipated daughters used for reconstruction in this analysis, $p + \pi^-$, 63.9% of the time. This means that roughly 36% of Λ particles are decaying in a way that will not be seen in this analysis, but are still present in the collision. This Λ may have come from a P$_s$ which cannot be detected in this analysis.

The raw amounts of pentaquark candidates expected in the invariant mass plots for each decay channel are shown in Table 8. Channels that have rarer decay daughters tend to have lower efficiencies, which would reduce the amount of expected pentaquarks in the invariant mass plots.

	Events	a x ϵ_{rec}	B.R.	dN/dy	Total Counts
ϕp	2.016×10^9	0.0418	0.491	3.83184×10^{-4}	15,854
$K^+\Sigma^{*-}$	2.016×10^9	0.0227	0.556	3.83184×10^{-4}	9,749
$K^0_S\Sigma^{*+}$	2.016×10^9	0.0089	0.442	3.83184×10^{-4}	3,038
$K^+\Lambda$	2.016×10^9	0.0529	0.639	3.83184×10^{-4}	26,112
$K^0_S\Lambda$	2.016×10^9	0.0180	0.442	3.83184×10^{-4}	6,146

Table 8: Criteria used to determine the amount of raw P$_s$(2065) candidates expected in the invariant mass distribution for each channel.

The raw amount of each channel can be compared to the statistical error bars to see how likely the observation of a signal should be if the thermal model yield prediction is accurate. After residual backgrounds subtraction, the ϕp channel in particular has a spread in statistical errors from around -700 to 600, which is about 8% of the expected total signal of 15,854. The $K^+\Sigma^{*-}$ channel has spread in statistical errors from around -2000 to 2000, which is about 41% of the expected total signal, so a narrow peak consisting of 9,749 pentaquarks may still be visible but not as visible as other channels.

7.1.2 P$_s$ Mass = 2255 MeV/c^2

The first mass prediction of 2065 MeV/c^2 did not produce any observable peaks in the invariant mass distributions. The second mass prediction, though heavier, is far enough away from the kinematic limit of each decay channel that the background estimation methods are more in line with the data.

As mentioned before, the invariant mass plots for the P$_s$(2255) $\rightarrow \phi p$ have already been shown in a previous chapter, so they will not be presented again. The ϕp plots follow the same trends as the rest of the channels presented in this chapter. However, since the 2255 MeV/c^2 prediction is well enough away from the kinematic limit of K^{*0} and K^{*+}, these two channels will be analyzed in this section.

Fig. 7.8 shows the mixed-event background subtracted invariant mass plots for each decay channel. The gray shaded region indicates the mass region for the P$_s$ from theory while the blue line is the polynomial fit near the signal region to estimate the residual background. This fit spans 5Γ above and below the shaded region, to ensure that the fit encompasses the behavior of the background. The gray signal shaded region is not taken into account while fitting the polynomial, as to not bias any potential signal. This mass region is on the "downward" trend of the distribution for each channel, making the residual background fit to the distribution much cleaner.

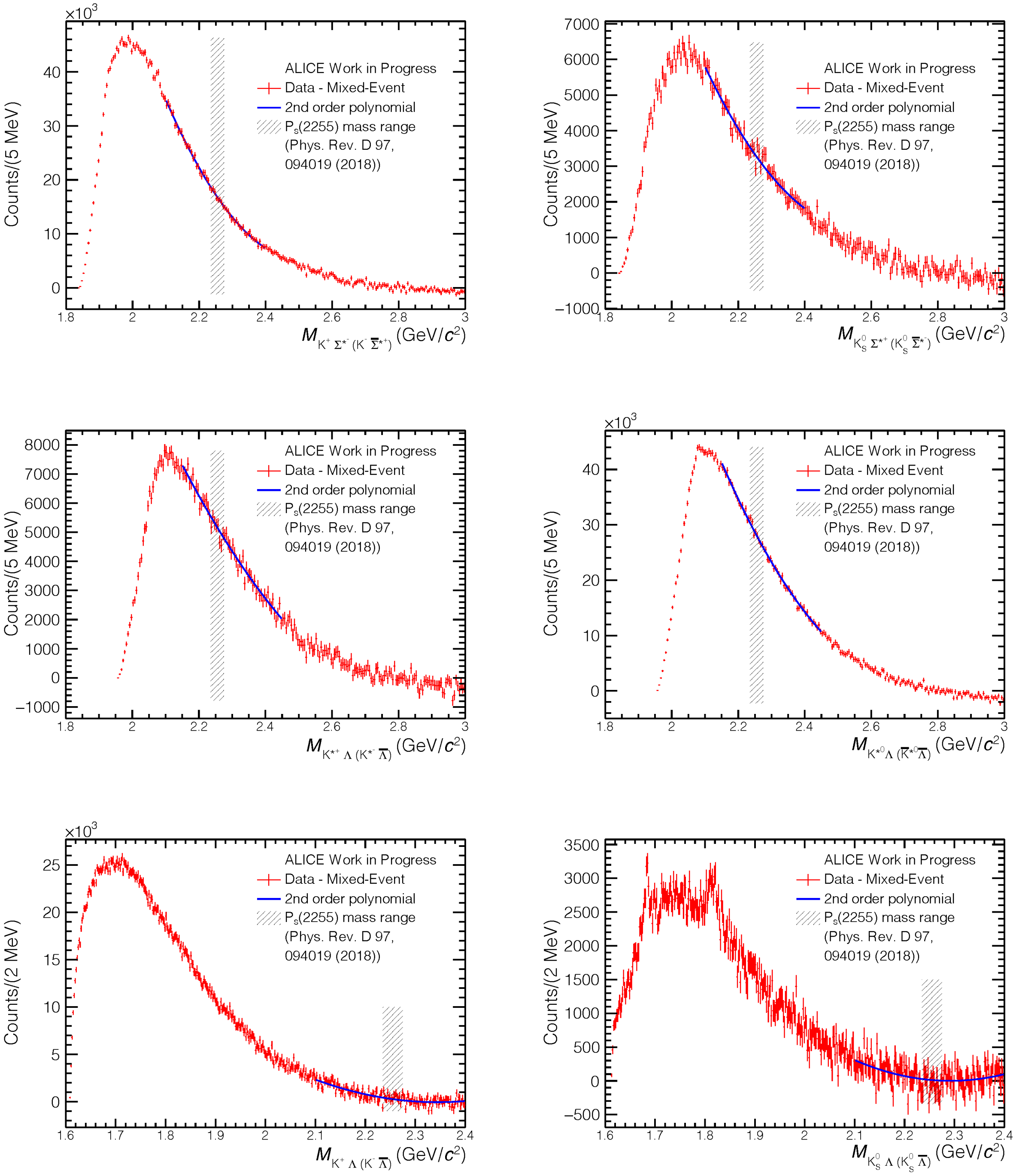

Figure 7.8: Mixed-Event background subtracted distributions for (top left) (top left) $K^+\Sigma^{*-}$, (top right) $K^0_S\Sigma^{*+}$, (middle left) $K^{*+}\Lambda$, (middle right) $K^{*0}\Lambda$, (bottom left) $K^+\Lambda$, and (bottom right) $K^0_S\Lambda$. Second degree polynomial fits are shown in blue for each distribution and a shaded gray region indicates the mass prediction region from theory [47].

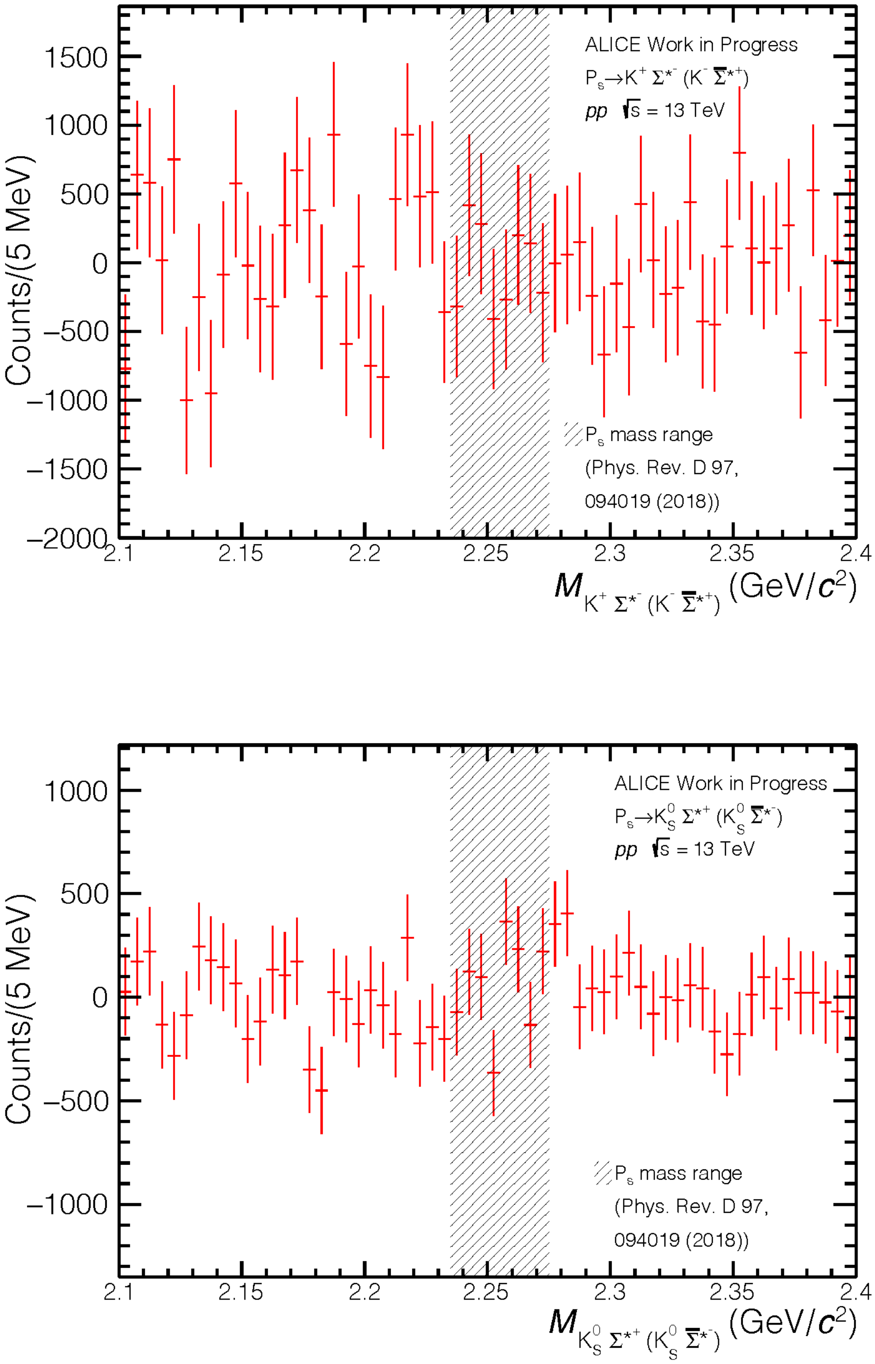

Figure 7.9: Residual background subtracted distributions for (top) $K^+\Sigma^{*-}$ and (bottom) $K^0_S\Sigma^{*+}$. The shaded gray band indicates the mass prediction region from theory [47]. No apparent peaks are observable for any channel.

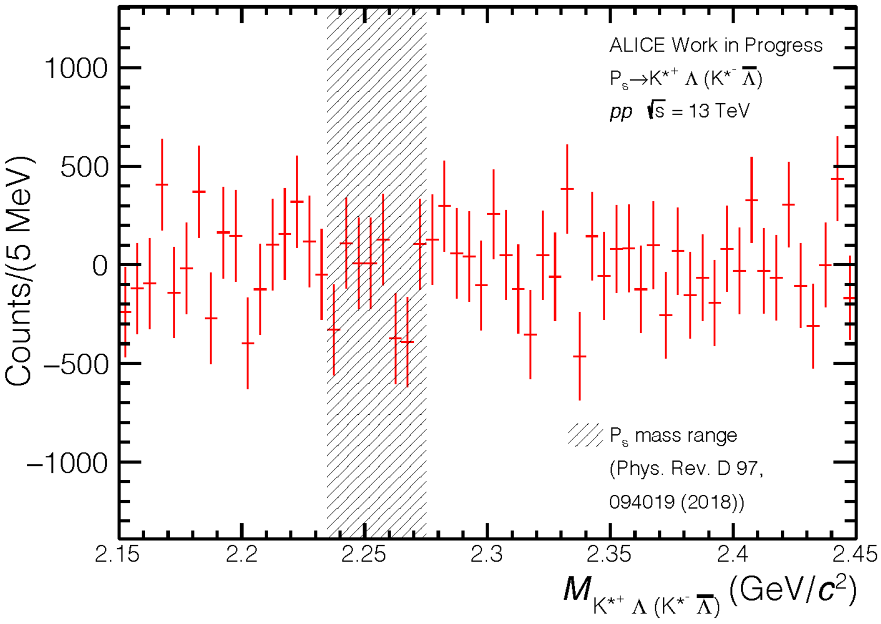

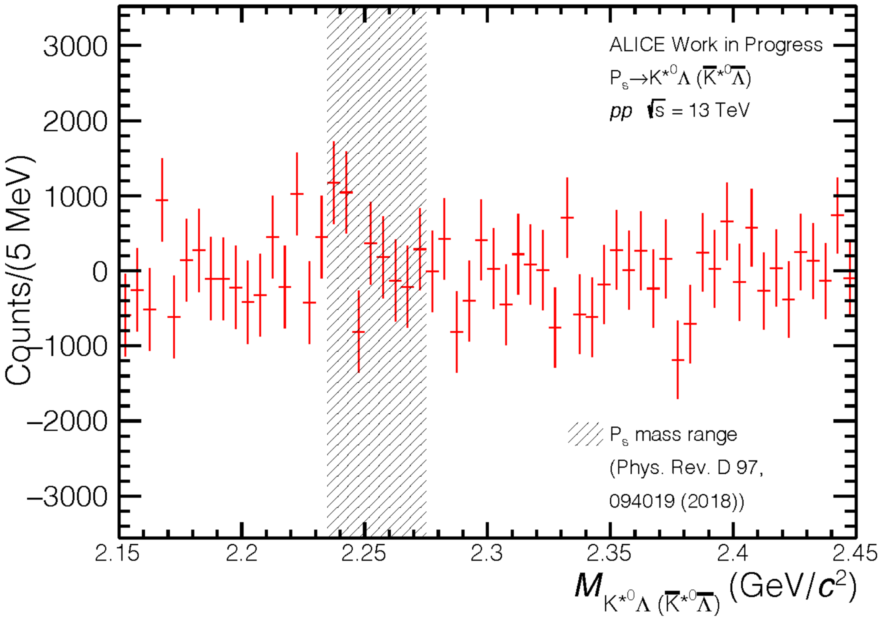

Figure 7.10: Residual background subtracted distributions for (top) $K^{*+}\Lambda$ and (bottom) $K^{*0}\Lambda$. The shaded gray band indicates the mass prediction region from theory [47]. No apparent peaks are observable for any channel.

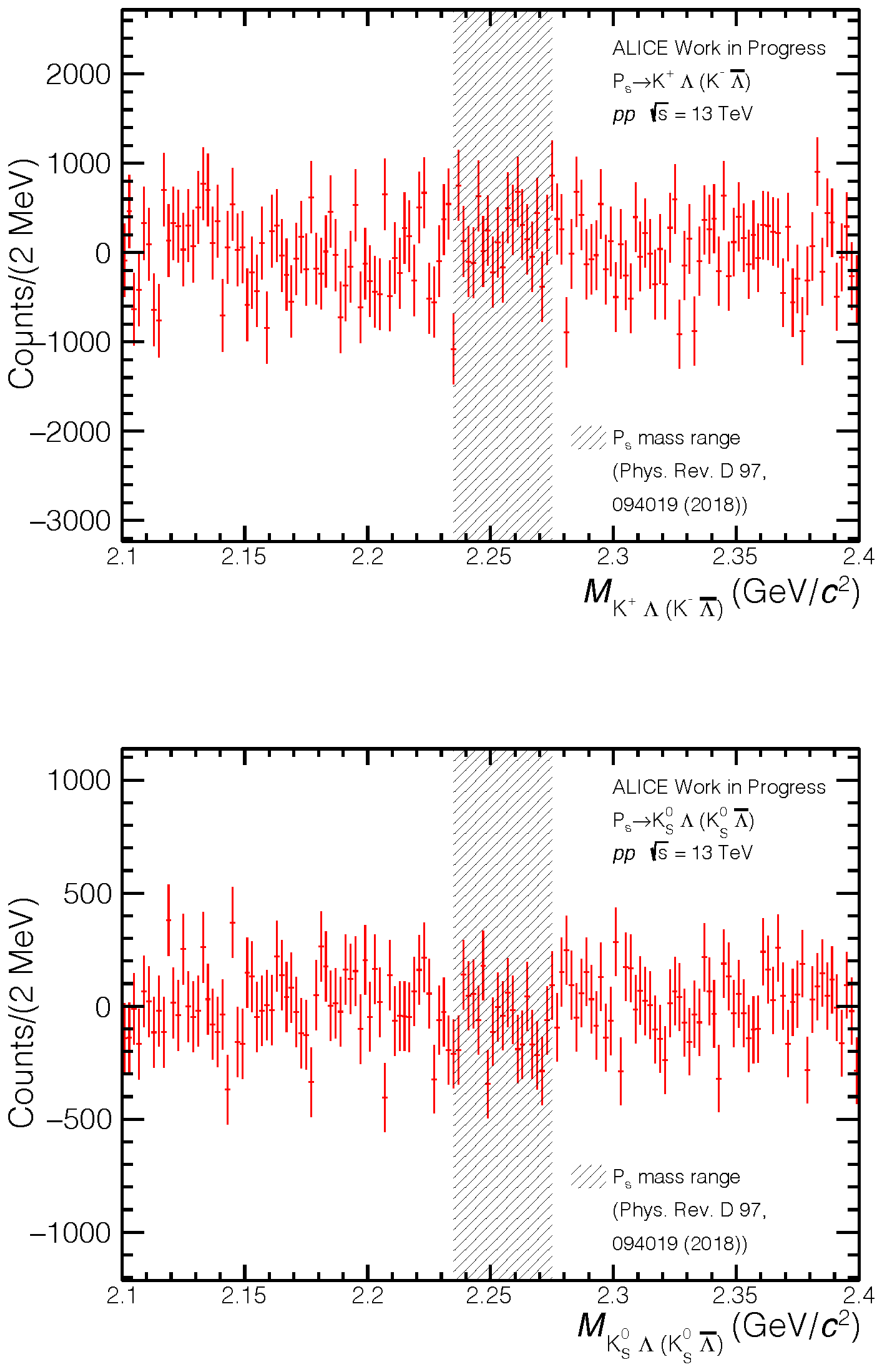

Figure 7.11: Residual background subtracted distributions for (top) $K^+\Lambda$ and (bottom) $K^0_S\Lambda$. The shaded gray band indicates the mass prediction region from theory [47]. No apparent peaks are observable for any channel.

	Events	a x ϵ_{rec}	B.R.	dN/dy	Total Counts
ϕp	2.016×10^{9}	0.0396	0.491	1.2902×10^{-4}	5,057
$K^{+}\Sigma^{*-}$	2.016×10^{9}	0.0224	0.556	1.2902×10^{-4}	3,239
$K^{0}_{S}\Sigma^{*+}$	2.016×10^{9}	0.0088	0.442	1.2902×10^{-4}	1,011
$K^{*+}\Lambda$	2.016×10^{9}	0.00265	0.639	1.2902×10^{-4}	440
$K^{*0}\Lambda$	2.016×10^{9}	0.0153	0.442	1.2902×10^{-4}	1,785
$K^{+}\Lambda$	2.016×10^{9}	0.0540	0.639	1.2902×10^{-4}	8,975
$K^{0}_{S}\Lambda$	2.016×10^{9}	0.0182	0.442	1.2902×10^{-4}	2,092

Table 9: Criteria used to determine the amount of raw $\mathrm{P}_s(2255)$ candidates expected in the invariant mass distribution for each channel.

Similar to the background subtracted invariant mass plots for the lower $\mathrm{P}_s(2065)$ mass state, the $\mathrm{P}_s(2255)$ mass state also shows no observable peaks for any decay channels in this analysis. Looking at Table 9, the total counts are significantly lower than that of Table 8, mostly due to a lower yield prediction for particles with a higher mass. The channel $K^{*+}\Lambda$ has statistical errors that are around 90% of the total expected count, which means that a signal for this channel at this mass would likely not be able to be observed. The multiple reconstructions needed to form a K^{*+} drastically reduce its efficiency, as previously mentioned. Increasing the statistics would increase both the expected signal as well as the statistical errors, but the signal would increase linearly, while the statistical errors increase at a slower rate, as outlined in Sec. 6.1. This would favor the extremely simple idea that increasing the statistics used in a search for new particles increases the chance of observing a peak. Although no signal is observed in the invariant mass plots for this search, an upper limit to the yield can be determined for each pentaquark mass and each decay channel.

7.2 Calculations for the Upper Limit to the Yield

Since no signal peak was observed, an upper limit to the yield must be determined. The upper limit corresponds to the value at which a detection of a signal would be measured. If the number of counts in the signal is greater than a certain threshold (the upper limit), then the signal should be detected. The actual yield of the particle must be below this upper limit if no signal was observed.

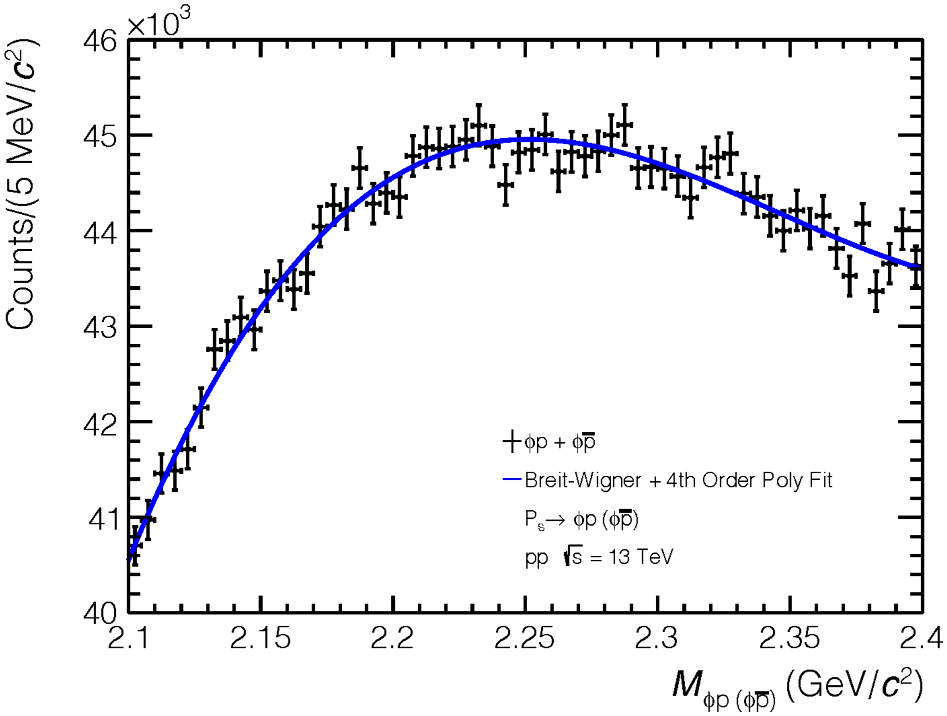

Figure 7.12: Invariant mass distribution of $\mathrm{P}_s \to \phi p$ with a blue fit of a Breit-Wigner distribution on top of a 4th degree polynomial.

In order to calculate an upper limit to the yield of a P_s, we need to determine confidence limits for both a background model and the signal+background model of the data. The profile likelihood ratio test is used to test a hypothesized value of μ against alternative values. It is obtained with the formula:

$$\lambda(\mu) = \frac{L(\mu, \hat{\hat{\theta}})}{L(\hat{\mu}, \hat{\theta})}, \tag{49}$$

where μ is the parameter of interest to be varied (number of signal counts in this case), $\hat{\hat{\theta}}$ is the value of θ (nuisance parameter) that maximizes L for the assumed value of μ, which makes $\hat{\hat{\theta}}$ a function of μ itself. $\hat{\mu}$ and $\hat{\theta}$ are the true maximum likelihood estimators for each parameter [73].

The profile likelihood ratio is then used to determine the log-likelihood ratio as the function

$$t = -2\ \mathrm{ln}\lambda(\mu) \approx 1 - \alpha \tag{50}$$

From this equation, a confidence level can be obtained for a specified test [73]. Finding the confidence level for both the background distribution and the signal+background distribution can be done using these equations. The confidence level for both of these models will need to be determined in order to obtain the confidence level of the signal.

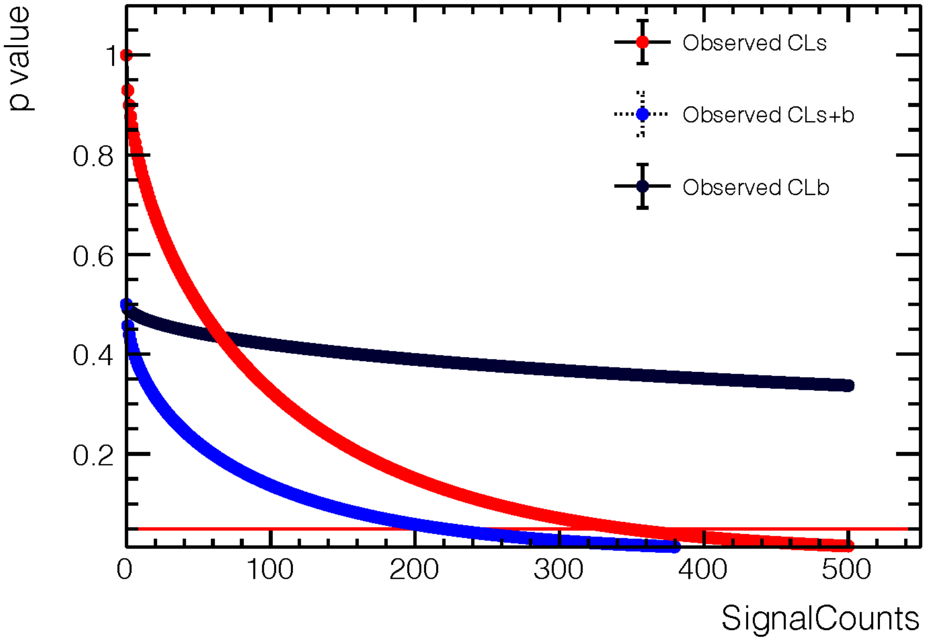

Figure 7.13: Confidence levels for the signal (red circles), the signal+background (blue circles), and the background only (black circles) as a function of signal counts. The red horizontal line at 0.05 indicates the threshold where an upper limit can be established at 95% confidence level.

Fig. 7.12 shows the data from the ϕp channel that is fit with a function comprised of a 4th degree polynomial for background estimation with a Breit-Wigner distribution centered at 2.255 GeV/c^2

and a width of 0.020 GeV/c^2 for signal estimation. The fit shows no peak, as expected, which indicates that the background is dominating and any peak would be very small. The confidence level of just the background model (CL$_b$) can be calculated as well as the confidence level of the signal+background model (CL$_{s+b}$). The confidence level of the signal can be obtained by CL$_s$ = CL$_{s+b}$/CL$_b$. This can be shown as a distribution by performing this calculation for each value of μ, or increasing the number of counts in the signal. By increasing the number of signal counts, the p-value of the CL$_s$ drops. Once the value of CL$_s$ reaches 0.05, corresponding to a 95% confidence level, this value for signal counts can be denoted as the upper limit with a 95% confidence level. These calculations are performed using the RooStats macro StandardHypoTestInvDemo.C [74]. The behavior of the confidence levels as well as when CL$_s$ crosses 0.05 for P$_s$(2255) $\rightarrow \phi p$ can be seen in Fig. 7.13. The upper limit is calculated to be 327 signal counts for the data in the ϕp channel. This indicates that the actual amount of signal counts in the data must have been lower than 327.

7.3 Yield Comparison to Thermal Model

The upper limit calculations was performed for each channel at each mass. Table 10 shows the raw upper limit calculated by the RooStats macro and the corrected upper limit for each channel and each mass. Comparing the upper limit of the yield from this search to the predictions made by the thermal model using Thermal FIST can help lend credence to whether the thermal model can accurately predict the yields of multiquark states as it currently stands.

As mentioned in Sec. 3.3.2, the data from ALICE that was input into Thermal FIST calculations are for $\pi^{\pm}$, $K^{\pm}$, p, $\bar{p}$, Λ, $\bar{\Lambda}$, Ξ^-, $\bar{\Xi}^+$, Ω^-, $\bar{\Omega}^+$, K^0_S, and ϕ in minimum bias pp collisions at mid-rapidity ($|y|$ <0.5) at $\sqrt{s}$ = 13 TeV. In order to compare these results to the Thermal FIST predictions, the results need to be in the same format as the predictions. While these results have the same collision system and energy, as well as acceptance range and centrality, they are not yet normalized by the number of events nor corrected for efficiency or branching ratio. The equation for correction of the upper limit calculation is as follows:

	UL$_{raw}$ (2065)	UL$_{corrected}$ (2065)	$\frac{\text{UL}_{corrected}}{\text{Thermal Model}}$ (2065)	UL$_{raw}$ (2255)	UL$_{corrected}$ (2255)	$\frac{\text{UL}_{corrected}}{\text{Thermal Model}}$ (2255)
ϕp	237	5.73×10^{-6}	66.8	327	8.35×10^{-6}	15.4
$K^{+}\Sigma^{*-}$	395	1.54×10^{-5}	24.7	503	1.99×10^{-5}	6.4
$K_{S}^{0}\Sigma^{*+}$	494	7.10×10^{-5}	5.4	410	5.96×10^{-5}	2.1
$K^{*+}\Lambda$	-	-	-	295	1.25×10^{-4}	1.0
$K^{*0}\Lambda$	-	-	-	363	1.83×10^{-5}	7.0
$K^{+}\Lambda$	5525	8.09×10^{-5}	4.7	4009	5.75×10^{-5}	2.2
$K_{S}^{0}\Lambda$	1203	7.47×10^{-5}	5.1	910	5.60×10^{-5}	2.3

Table 10: The raw and corrected upper limits at a 95% confidence level for each channel and each mass state. UL$_{corrected}$ is calculated by using Eq. 51. The ratios of the corrected upper limits to the thermal model yield predictions are also shown.

$$UL_{corrected} = \frac{UL_{raw}}{N_{events} \times efficiency \times B.R. \times dy} \tag{51}$$

The number of events, efficiency, and branching ratios have already been discussed previously and can be seen in Table 8 for P$_s$(2065) and in Table 9 for P$_s$(2255). The total rapidity range is set to 1 as $|y| < 0.5$, which means $dy = (0.5\text{-}(\text{-}0.5)) = 1$. The same rapidity range was used for the invariant mass reconstruction of each P$_s$ state, for the yields input into Thermal FIST, and for the P$_s$ Monte Carlo simulation, to ensure that all of the data is compatible in acceptance. The raw upper limit value is normalized by the number of events, giving the number of pentaquarks per event. Then this value is also divided by the efficiency. The idea of a yield per event is to find out how many pentaquarks are produced in each collision per rapidity window, regardless if the ALICE detector is able to reconstruct it or not. Dividing by the efficiency helps correct for all the pentaquarks that are produced in the collision but were missed by the detector or unable to be properly reconstructed. Also dividing by the branching ratio of the daughters corrects for the daughter decay channels that are not reconstructed by this analysis. The corrected upper limits for each channel and mass can be seen in Table 10.

The corrected upper limits are plotted in Fig. 7.14 along with the predictions for the yield from

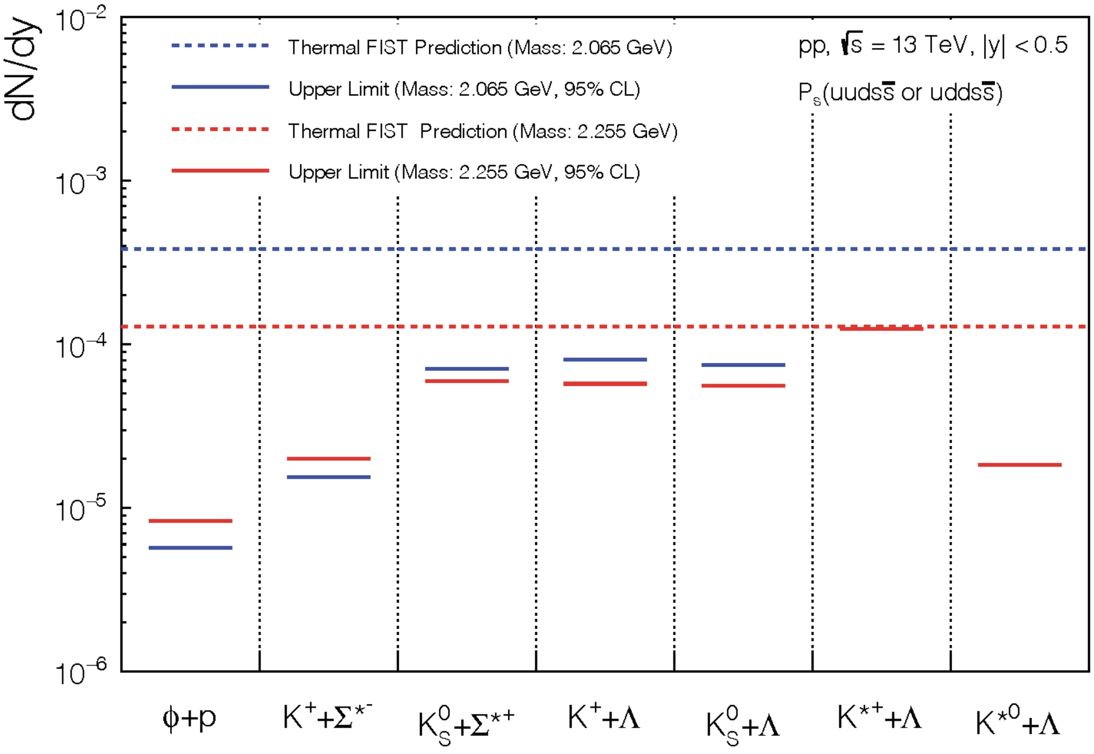

Figure 7.14: Upper Limit of the P_s yield per unit rapidity at mid rapidity in minimum bias pp collisions at $\sqrt{s} = 13$ TeV for each decay channel and two different masses, 2065 MeV/c^2 (blue solid) and 2255 MeV/c^2 (red solid). The blue and red dashed lines are the thermal model predictions from Thermal FIST of the $P_s(2065)$ and $P_s(2255)$ yields, respectively. The raw upper limit calculations have been corrected for efficiency and branching ratio.

Thermal FIST. The blue lines correspond to yields concerning $P_s(2065)$ and the red lines correspond to the yields concerning $P_s(2255)$. The red and blue dashed lines represent the predictions from Thermal FIST for the mass estimates of 2065 and 2255 respectively. These lines are the same for each channel because they are a function of the mass of the particle, which is channel independent in this analysis. The solid lines represent the upper limits to the yields calculated in this analysis. The upper limit represents the highest possible value for the yield in this analysis, meaning the yield must be at this value or below. What is evident about these lines is that the vast majority of them are well below the Thermal FIST prediction. The upper limit for $P_s(2065) \to \phi p$ is ~66 times lower than the thermal model prediction while the value for $P_s(2255) \to K^{*+}\Lambda$ is right at the thermal model prediction. This is most likely driven by the very low efficiency of the K^{*+} reconstruction. The rest of the ratios to the thermal model for each channel and each mass can be seen on Table 10.

Fig. 7.14 indicates that the thermal model does not accurately account for the yields of hidden-strangeness pentaquark states in minimum bias pp collisions at mid-rapidity at $\sqrt{s} = 13$ TeV. A significant upper limit can be set for almost all channels in this analysis at both mass estimates. Table 11 shows the yield upper limits from Fig. 7.14 along with the systematic errors. It should be noted that the $P_s \to K^{*+}\Lambda$ and $P_s \to K^{*0}\Lambda$ channels are not included in the $P_s(2065)$ upper limit section.

Increased statistics can help elucidate whether any hidden-strangeness pentaquark peaks are able to be observed in this invariant mass region. With the recent upgrades to the ALICE ITS and ALICE TPC, as well as LHC Run 3 being in full swing, better particle identification and increased statistics may be able to shed more light on hidden-strangeness pentaquark production in pp, p-Pb, and Pb-Pb.

	Upper Limit ± Syst. (2065)	Upper Limit ± Syst. (2255)
ϕp	$(5.73 \pm 1.50) \times 10^{-6}$	$(8.35 \pm 2.30) \times 10^{-6}$
$K^+\Sigma^{*-}$	$(1.54 \pm 0.17) \times 10^{-5}$	$(1.99 \pm 0.29) \times 10^{-5}$
$K^0_S\Sigma^{*+}$	$(7.10 \pm 0.88) \times 10^{-5}$	$(5.96 \pm 0.87) \times 10^{-5}$
$K^{*+}\Lambda$	-	$(1.25 \pm 0.20) \times 10^{-4}$
$K^{*0}\Lambda$	-	$(1.83 \pm 0.30) \times 10^{-5}$
$K^+\Lambda$	$(8.09 \pm 0.87) \times 10^{-5}$	$(5.75 \pm 0.89) \times 10^{-5}$
$K^0_S\Lambda$	$(7.47 \pm 0.79) \times 10^{-5}$	$(5.60 \pm 0.62) \times 10^{-5}$

Table 11: Upper limits calculations for each channel and each mass with systematic uncertainties

8 Conclusion and Further Discussion

This work presents the results of the search for hidden-strangeness pentaquarks with ALICE in minimum bias pp collisions at $\sqrt{s} = 13$ TeV. Following in the footsteps of the LHCb discovery of hidden-charm pentaquarks, similar decay channels are searched through invariant mass analysis. While a signal was observed for pentaquarks in the charm sector, no such signal is observed in any analyzed channel in the strange sector. Significant upper limits to the yields for each decay channel are set, that are below the predictions made from the thermal model of particle production in a heavy-ion collision.

One key question that opens up after not observing a pentaquark signal in the strange sector is: Why are exotic particles (tetraquarks and pentaquarks) able to be observed in the charm sector, but not the strange sector? Several pentaquark states have been observed in the charm sector, as discussed in 3.2. Several tetraquarks as well have been observed at LHCb, most with hidden-charm just like the pentaquarks, but some also have open charm [15]. The thing that all these exotic states have in common is that they contain at least one charm quark. Is it possible that the heavy mass of the charm quark allows for four or five quark bound states to occur and that the lower mass of the strange quark is not enough to bind four or five quarks? Perhaps the heavier charm quark allows for a larger binding energy between quarks that the smaller strange quarks are unable to allow.

LHCb has in fact observed exotic tetraquark and pentaquark states that contain a strange quark, but they also always contain at least one charm quark. In 2021, LHCb observed tetraquark candidate $Z_{cs}(4000)$ through the invariant mass reconstruction of $J/\psi K^+$ pairs, which gives this state the quark content of $c\bar{c}u\bar{s}$, which is similar in nature to the charm pentaquarks that also have hidden charm [62]. In July of 2022, LHCb observed another pentaquark, $\mathrm{P}^{\Lambda}_{\psi s}(4338)$, but this one contains a strange quark. Through the invariant mass reconstruction of $J/\psi\Lambda$ pairs, a signal was observed with a mass of ~4338 MeV/c^2, a width of about 7 MeV/c^2 and a quark content of $udsc\bar{c}$. While it is encouraging to see that these observations confirm that strange quarks can be contained in tetraquark and pentaquark states, this encouragement is tempered by the fact that each state also contains one or more charm quarks as well. This seems to point to the fact that the formation or binding mechanism is tied to the charm quark, possibly its mass. This idea needs further investigation and experimentation. The invariant mass plots and projected fits to the data for the $Z_{cs}(4000)$ and $\mathrm{P}^{\Lambda}_{\psi s}(4338)$ can be seen in Fig. 8.1 [62][63].

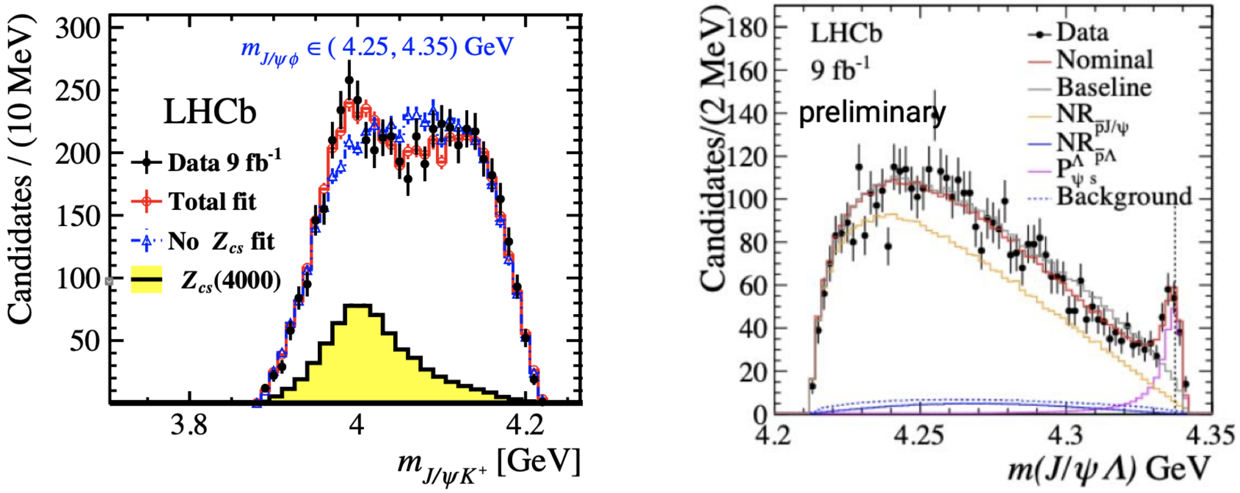

Figure 8.1: Invariant mass plot of $Z_{cs}(4000)$ with projected fits (left) and $\mathrm{P}^{\Lambda}_{\psi s}(4338)$ (right) with fits [62][63].

The upper limits set in this work for each decay channel are below thermal model predictions. The thermal model of particle production describes many particle yields very well, especially in Pb-Pb collisions. Fig. 8.2 shows the comparison of light particles, light nuclei, and exotica measured at ALICE in Pb-Pb collisions. What is very apparent from the plot is that the thermal model describes the production of light particles, even strange particles, very well. Even the nuclei (^{3}He and $^{4}\overline{\mathrm{He}}$) and hyper-nuclei ($^{3}_{\Lambda}$H), a nucleus containing a strange baryon) are very well described by thermal fits. The glaring takeaway from Fig. 8.2 is that the exotic dibaryon states of Λn and $\Lambda\Lambda$ do not match up with thermal model predictions at all. Not only was there no observation of a dibaryon state in either case, but the upper limits to the yields were set 25 times below the thermal model prediction. This number can be compared to the factor 66 that is established in this analysis for $P_s(2065) \to \phi p$. Production mechanisms for nuclei may be different than for multiquark states. Perhaps nuclei are able to form later during the hadronic phase through coalescence when a multiquark system may not form.

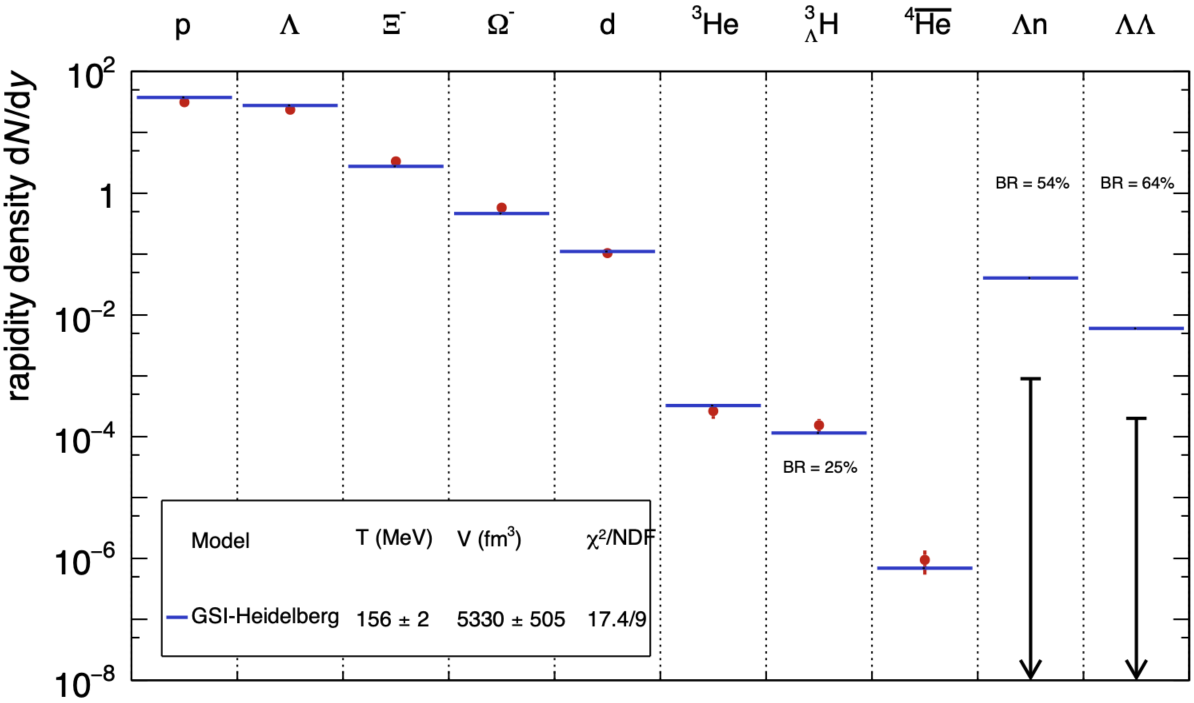

Figure 8.2: Comparison of production yields, dN/dy, for various light particles, light nuclei, and exotica with thermal model predictions. The red dots show the observed ALICE data. Upper limits are shown for Λn and $\Lambda\Lambda$ [64].

As mentioned in 1.6, larger collisions systems like Pb-Pb have a larger volume for particle production than pp collisions. The increase in particle production allows for the use of a Grand Canonical Ensemble where certain quantities are conserved on average. With pp being such a small system compared to the Pb-Pb collision system (2 colliding nucleons vs. 416 colliding nucleons), there is a question of whether a QGP truly forms in a pp collision at all. Perhaps in the absence of QGP formation, there are fewer mechanisms that encourage multiquark state production. As shown in Fig. 8.2, the thermal model makes very good predictions for Pb-Pb collisions, but perhaps production mechanisms in pp are very different for multiquark particle production in the light quark sector. The thermal model may not be a good prediction for pp collisions, especially with higher mass multiquark states.

Recent femtoscopic studies from ALICE of the correlations between hadrons have shown

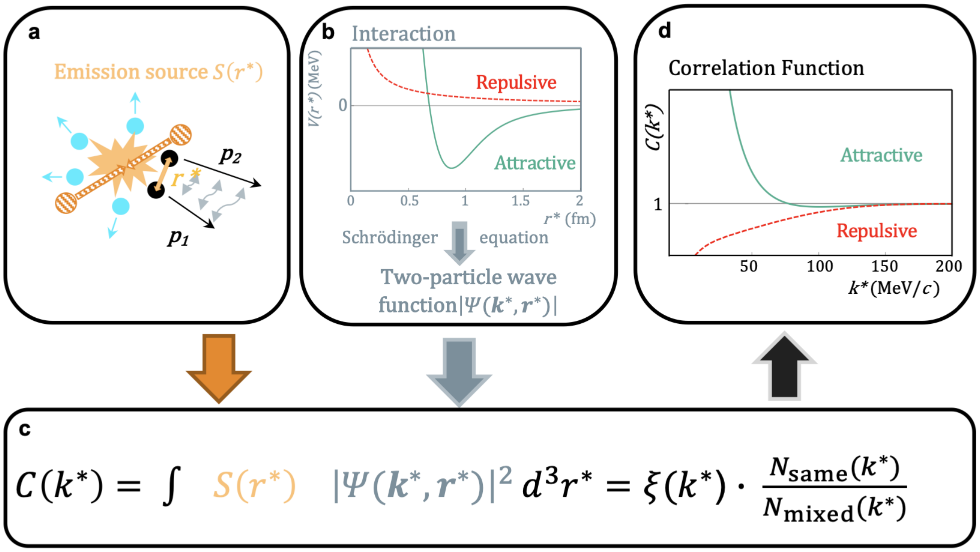

Figure 8.3: A schematic representation of the correlation method. (a) shows a particle source from the collision of two protons. (b) shows an example of repulsive and attractive potentials between two hadrons. Given a certain potential, a two particle wave function can be obtained. (c) shows the equations for the correlation function. (d) shows a sketch of a resulting correlation function and how to interpret the shape [68].

attractive potentials that may suggest a bound state is possible [67] [68]. Femtoscopy aims to measure two-particle short range correlations as a function of the relative momentum, k^*, between the two particles. While pp collisions provide a particle source of size ∼1 fm, Pb-Pb collisions can provide a source with a size greater than 3 fm. This is significant because, with a smaller system size and a smaller phase space in an ultra-relativistic collision, Kp scattering interactions can not be fully accessed because of coupled channels. While the final measured state may be Kp, the initial state may have been $\overline{K}^0 n$ or $\pi\Sigma$, which affect the Kp correlation. Theoretical predictions have estimated that the strength of the coupled channels is significantly reduced when the source size is greater than 3 fm. This ALICE study has measured closer to 9 fm in central Pb-Pb collisions. Fig. 8.4 shows the $K^- p \otimes K^+ \bar{p}$ correlations with model predictions as well for three different centrality bins in Pb-Pb collisions at $\sqrt{s_{NN}} = 5.02$ TeV [67].

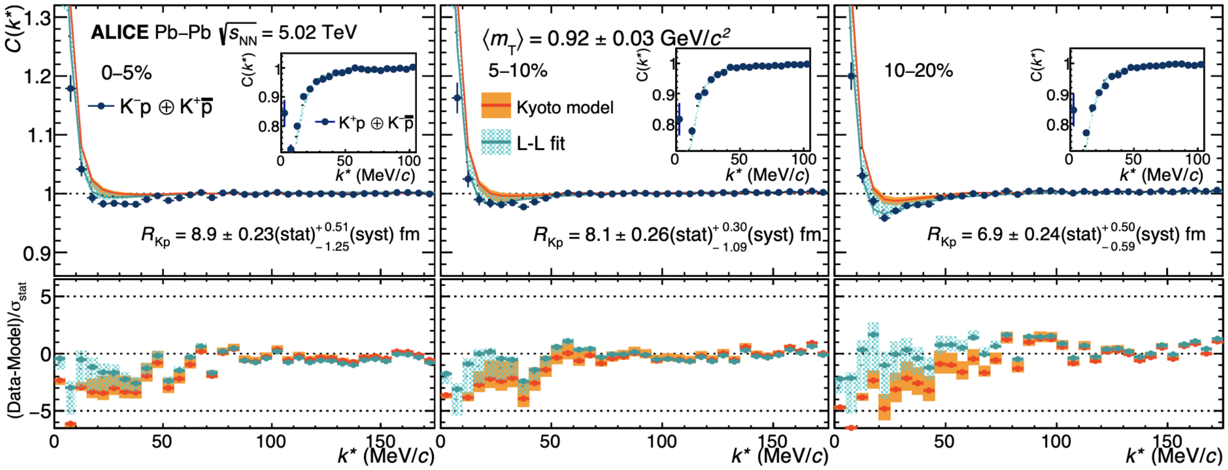

Figure 8.4: The $K^-p \otimes K^+\bar{p}$ correlation functions for three different centrality classes in $\sqrt{s_{NN}} = 5.02$ TeV Pb-Pb collisions. Data points are shown along with two different model calculations in the top boxes. Bottom boxes show the difference between the data and the models normalized by the statistical uncertainty of the data [67].

What is shown in the upper plots is that, for low relative momentum between the proton and kaon, the correlation value goes above 1, which indicates an attractive potential between the two particles. This attractive potential may correspond to the ability of these two particles to form a bound state, which could be a potential pentaquark. The upper plots also have a smaller box that shows the $K^+p \otimes K^-\bar{p}$ correlations, which are like sign particles. These plots show an anti-correlation at low relative momentum, indicating a repulsive potential between the particles, which makes them unlikely to form a bound state [67].

Femtoscopic studies can go beyond baryon-meson correlations into baryon-baryon correlations as well. ALICE has also conducted femtoscopic measurements of $p - \Xi$ and $p - \Omega$ correlations in $\sqrt{s} = 13$ TeV pp collisions [68]. The correlation functions, as well as several theoretical predictions can be seen in Fig. 8.5. The data points for both $p{-}\Xi$ and $p{-}\Omega$ show a sharp increase at low relative momentum, indicating an attractive potential. The green band shows the theoretical prediction for the correlation for each pair of particles when only Coulomb interactions are taken into account,

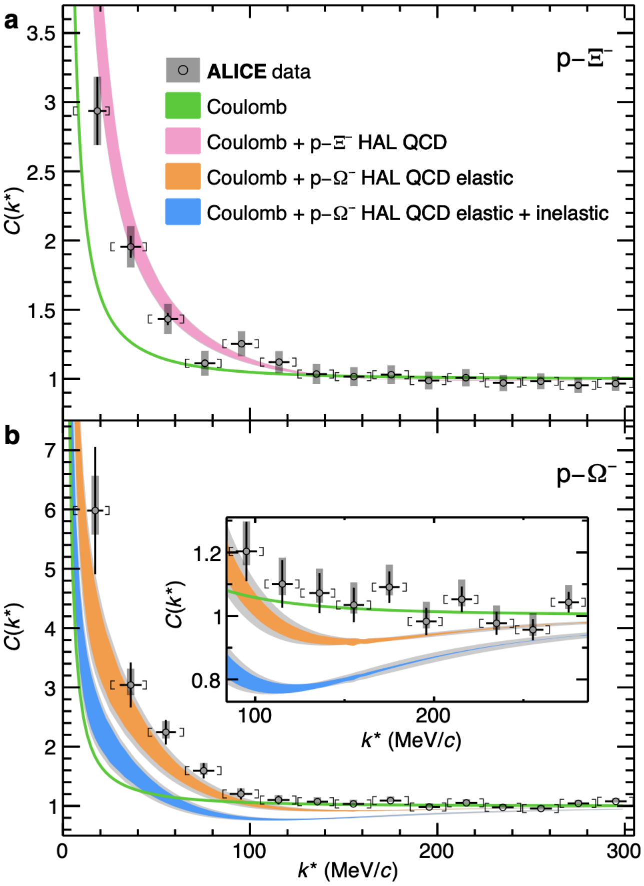

Figure 8.5: The $p-\Xi$ (top) and $p-\Omega$ (bottom) correlation functions in $\sqrt{s} = 13$ TeV pp collisions as a function of k^*. The green bands represent theoretical calculations with only Coulomb interactions taken into account, while the pink, blue, and orange bands take strong and Coulomb interactions into account [68].

while the other colored bands take Coulomb as well as strong interactions into account. The green bands do not represent the data as well as the pink, blue, and orange do. This indicates that the attractive potentials between both $p-\Xi$ and $p-\Omega$ are not just due to the charges that they possess, but the actual quarks and gluons within the hadrons contribute to the attraction, which may lead to a bound state.

All of these correlations show that particles with strangeness have the potential to form exotic bound multiquark states, although there has been no such state observed in the light sector. This analysis focused on looking for pentaquarks in pp collisions because of the large data set and smaller background, but it may be possible that the mechanism to form pentaquarks is enhanced in a heavier collision system like Pb-Pb. Some dibaryon (or hexaquark) channels have been searched at ALICE [61], but there are channels with newer evidence of a bound state, like $p - \Xi$ and $p - \Omega$, that can be searched in pp as well as Pb-Pb [68]. There are plenty of avenues still open for the long awaited discovery of new light exotic bound states and Run 3 at the LHC with increased statistics and luminosity may represent the best chance at a discovery.

This study definitively answers the question of whether strange pentaquarks are produced in pp collisions at a rate predicted by thermal models. The answer is ‘no’, which combined with the lack of signal in the H-Dibaryon channel significantly constrains the anticipated production mechanism for multiquark states in the light/strange sector. Its potential impact on the formation of hyper matter in dense stellar objects will have to be evaluated and complemented with similar studies in heavy ion collisions at various collision energies.

Bibliography

[1] E. Kolb and M. Turner, "The early universe," Addison-Wesley, Redwood City, 1990.

[2] TheAstronomyBum, "The History of the Universe," WikiMedia Commons, Public Domain, CC0 1.0.

[3] D. Griffiths, "Introduction to Elementary Particles," John Wiley & Sons, 49-52, 2008.

[4] MissMJ, "Standard Model of Elementary Particles," WikiMedia Commons, CC-BY-3.0.

[5] C. Myers, "Investigation Of Chiral Symmetry Restoration Using Ξ(1820) Reconstruction From p-p, p-Pb, and Pb-Pb Collisions at ALICE," PhD Thesis, University of Houston , August 2020.

[6] M. Płoskoń, "Heavy-ion collisions - hot QCD in a lab," arXiv:1808.01411v1, 2018.

[7] S. Bethke, "Experimental Tests of Asymptotic Freedom," Progress in Particle and Nuclear Physics, 58(2):351-386, 2007.

[8] C. Markert, "What do we learn from resonance production in heavy ion collisions?," J. Phys. G: Nucl. Part. Phys. 31 S169, 2005.

[9] Harp, "Breit-Wigner", WikiMedia Commons, Public Domain

[10] S. Olsen, "Exotic particles with four or more quarks," Physics Today 67, 9, 56 (2014).

[11] J. P. Adler, J. M. Richard, P. Taxil, "Do narrow heavy multiquark states exist?," Phys. Rev. D 25, 2370, 1982.

[12] C. Gignoux, B. Silvestre-Brac, J.M.Richard, "Possibility of stable multiquark baryons," Physics Letters B, Volume 193, Issues 2–3, 16 July 1987, Pages 323-326.

[13] R. Jaffe, "Perhaps a Stable Dihyperon," Phys. Rev. Lett. 38 (1977) 195-198.

[14] S. K. Choi et al. (Belle Collaboration), "Observation of a Narrow Charmoniumlike State in Exclusive $B^{\pm} \to K^{\pm}\pi^{+}\pi^{-}J/\psi$ Decays," Phys. Rev. Lett. 38 (1977) 195-198.

[15] R. Aaij et al. (LHCb Collaboration), “Observation of an exotic narrow doubly charmed tetraquark,” arXiv:2109.01038v2, 2021.

[16] S. Cho, et al. (ExHIC Collaboration), “Exotic hadrons from heavy ion collisions,” Progress in Particle and Nuclear Physics, Volume 95, Pages 279-322, 2017.

[17] A. Andronic, P. Braun-Munzinger, J. Stachel, et al. “Hadron production in central nucleus–nucleus collisions at chemical freeze-out” Nuclear Physics A, Volume 772, Issues 3–4, Pages 167-199, 2006.

[18] A. Andronic, P. Braun-Munzinger, K. Redlich, et al. “Decoding the phase structure of QCD via particle production at high energy,” Nature 561, 321–330 (2018).

[19] J. Rafelski and B. Muller. Erratum: “Strangeness Production in the Quark-Gluon Plasma,” [phys. rev. lett. 48, 1066 (1982)]. Physical Review Letters, 56(21):2334, 1986.

[20] ALICE Collaboration, “Multi-strange Baryon Production at Mid-rapidity in Pb-Pb Collisions at $\sqrt{S_{NN}} = 2.76$ TeV,” Physics Letters B, 728:216-227, 2014.

[21] A. Tounsi, K. Redlich, “Strangeness Enhancement and Canonical Suppression,” arXiv:hepph/0111159, 2001.

[22] ALICE Collaboration, “Definition of the ALICE coordinate system and basic rules for Sub-detector components numbering”, ALICE-INT-2003-038 (2003).

[23] The ALICE Collaboration, “Performance of the ALICE Experiment at the CERN LHC,” International Journal of Modern Physics A, 29(24):1430044, Sep 2014.

[24] https://public-archive.web.cern.ch/en/lhc/Facts-en.html

[25] https://home.cern/science/experiments/alice

[26] ALICE Collaboration, K. Aamodt et al., “The ALICE experiment at the CERN LHC,” JINST, 3, S08002 (2008).

[27] J.Alme, et al., “The ALICE TPC, a large 3-dimensional tracking device with fast readout for ultra-high multiplicity events,” Nuclear Instruments and Methods in Physics Research Section A: Accelerators, Spectrometers, Detectors and Associated Equipment, Volume 622,

Issue 1, 1 October 2010, Pages 316-367

[28] C. Lippmann, “Performance of the ALICE Time Projection Chamber,” Physics Procedia., 37, 434-441, 2012.

[29] J.A. Lien, D. Roehrich, H. Helstrup, and K. Ullaland, “Time projection chambers (TPC) in heavy ion experiments,” Eur Phys J C 33, s01, s1017–s1019 (2004)

[30] A. Kalweit, “Production of Light Flavor Hadrons and Anti-nuclei at the LHC,” Ph.D. Dissertation, Darmstadt, Tech. U., 2012.

[31] W. Blum, W. Riegler, and L. Rolandi. “Particle Detection with Drift Chambers,” Springer Science & Business Media, 29-407, 2008.

[32] ALICE Collaboration, “Production of charged pions, kaons and (anti-)protons in Pb-Pb and inelastic pp collisions at $\sqrt{s_{NN}} = 5.02$ TeV,” Phys. Rev. C, 101, 4 (2020).

[33] W. Huisman, “D-tagged jet measurements in the ALICE experiment,” Bachelor Thesis, Utrecht University, Institute for Subatomic Physics, June 2017.

[34] R. Preghenella, “10 years of operation of the MRPC TOF detector of ALICE, results and perspectives,” 10th International Workshop on Ring Imaging Cherenkov Detectors, Istituto Nazionale di Fisica Nucleare Sezione di Bologna, August 2018.

[35] C. Lippmann, “Particle Identification”, Nucl. Instrum. Meth. A, 666, 148-172 (2012).

[36] The ALICE collaboration, “Performance of the ALICE VZERO system”, JINST 8 P10016, 2013.

[37] D. Dominguez, https://cds.cern.ch/images/OPEN-PHO-EXP-2015-009-2

[38] M. Tanabashi, et al. (Particle Data Group), “Review of Particle Physics,” Phys. Rev. D 98, 030001, 2018.

[39] T. Nakano et al., “Evidence for a Narrow S = ±1 Baryon Resonance in Photoproduction from the Neutron,” Phys. Rev. Lett. 91, 012002, 2003.

[40] W.-M. Yao et al. (Particle Data Group), J. Phys. G 33, 1 (2006)

[41] C. Alt et al. (NA49 Collaboration), "Evidence for an Exotic S=-2, Q=-2 Baryon Resonance in Proton-Proton Collisions at the CERN SPS " Phys. Rev. Lett. 92, 042003

[42] ALICE Collaboration, "Production of $\Sigma(1385)^{\pm}$ and $\Xi(1530)^{0}$ in proton–proton collisions at $\sqrt{s}$= 7 TeV", The European Physical Journal C volume 75, Article number: 1 (2015)

[43] R. Aaij et al. (LHCb Collaboration), "Observation of $J/\psi p$ Resonances Consistent with Pentaquark States in $\Lambda_b^0 \to J/\psi K^- p$ Decays," Phys. Rev. Lett. 115, 072001, 2015.

[44] R. Aaij et al. (LHCb Collaboration), "Observation of a Narrow Pentaquark State, $P_c(4312)^+$, and of the Two-Peak Structure of the $P_c(4450)^+$" Phys. Rev. Lett. 122, 222001, 2019.

[45] E. Hiyama, A. Hosaka, M. Oka, and J. Richard, "Quark model estimate of hidden-charm pentaquark resonances" Phys. Rev. C 98, 045208, 2018.

[46] A. G. Knospe, Sissa: "New Results on Soft Particle Production in Heavy-ion Collisions with ALICE," PoS, page 217, 2018.

[47] H. Huang, J. Ping, "P_c-like pentaquarks hidden in the strange sector" Phys. Rev. D 97, 094019, 2018.

[48] R. Lebed, "Do the P_c^+ pentaquarks have strange siblings?" Phys. Rev. D 92, 114030, 2015.

[49] J. He, "Nucleon resonances N(1875) and N(2100) as strange partners of the LHCb pentaquarks" Phys. Rev. D 95, 074031 , 2017.

[50] J. He, H. Huang, D. Chen, X. Zhu, "Hidden-strange molecular states and the Nϕ bound states via a QCD van der Waals force" Phys. Rev. D 98, 094019 , 2018.

[51] Y. Lin, C. Shen, B. Zou, X. Zhu, "Decay behavior of the strange and beauty partners of P_c hadronic molecules" Nuclear Physics A, Volume 980, December 2018, Pages 21-31.

[52] P. Alba, V. Mantovani Sarti, J. Noronha-Hostler, P. Parotto, I. Portillo-Vazquez, C. Ratti, J. M. Stafford, "Influence of hadronic resonances on the chemical freeze-out in heavy-ion collisions," Phys. Rev. C 101, 054905 – Published 15 May 2020

[53] H. Ricaud, “Lambda and K^0_S in LHC pp collisions,” https://indico.in2p3.fr/event/1883/contributions/21837/attachments/17789/21772/ricaud_AF_Soft.pdf

[54] R. Barlow, “Systematic Errors: Facts and Fiction,” arXiv:hep-ex/0207026v1, 2002.

[55] ALICE Collaboration, “$\Sigma(1385)^{\pm}$ resonance production in Pb-Pb collisions at $\sqrt{s_{NN}} = 5.02$ TeV”, arXiv:2205.13998 [nucl-ex] (2022).

[56] ALICE Collaboration, “Production of $K^*(892)$ and $\phi(1020)$ in pp and Pb-Pb collisions at $\sqrt{s_{NN}} = 5.02$ TeV”, arXiv:2106.13113 [nucl-ex] (2021).

[57] ALICE Collaboration, “Production of $\Sigma(1385)^{\pm}$ and $\Xi(1530)^0$ in p-Pb collisions at $\sqrt{s_{NN}} = 5.02$ TeV”, arXiv:1701.07797 [nucl-ex] (2017).

[58] T. Nayak, B. Sinha, “ Search and study of Quark Gluon Plasma at the CERN-LHC”, arXiv:0904.3428v1 [nucl-ex], (2009).

[59] C. Tsallis, “Possible generalization of Boltzmann-Gibbs statistics”, J Stat Phys 52, 479-497, 1988

[60] ALICE Collaboration, “Production of light-flavor hadrons in pp collisions at $\sqrt{s} = 7$ and $\sqrt{s} = 13$ TeV”, The European Physical Journal C volume 81, Article number: 256 (2021)

[61] ALICE Collaboration, “Search for weakly decaying $\overline{\Lambda n}$ and $\Lambda\Lambda$ exotic bound states in central Pb-Pb collisions at $\sqrt{s_{NN}} = 2.76$ TeV”, Physics Letters B, Volume 752, Pages 267-277, 2016

[62] LHCb Collaboration, “Observation of New Resonances Decaying to $J/\psi K^+$ and $J/\psi\phi$”, Phys. Rev. Lett. 127, 082001 (2021)

[63] LHCb Collaboration, E. S. Norella, C. Chen, “Particle Zoo 2.0: New Tetra- and Pentaquarks at LHCb”, CERN Seminar, 2022

[64] B. Donigus, ALICE Collaboration, “ Highlights of the production of (anti-)(hyper-)nuclei and exotica with ALICE at the LHC”, J. Phys.: Conf. Ser. 1271 012001, 2019

[65] T. Sjostrand, et. al., “An introduction to PYTHIA 8.2”, Computer Physics Communications Volume 191, 2015

[66] P. Skands, S. Carrazza, and J. Rojo, “Tuning PYTHIA 8.1: the Monash 2013 tune”, The European Physical Journal C volume 74, Article number: 3024 (2014)

[67] ALICE Collaboration, “Kaon–proton strong interaction at low relative momentum via femtoscopy in Pb–Pb collisions at the LHC”, Physics Letters B, Volume 822, 136708, 2021

[68] ALICE Collaboration, “Unveiling the strong interaction among hadrons at the LHC”, Nature volume 588, pages 232–238 (2020)

[69] V. Vovchenko, H. Stoecker, “Thermal-FIST: A package for heavy-ion collisions and hadronic equation of state”, Computer Physics Communications, Volume 244, November 2019, Pages 295-310

[70] G. Kadam, S. Pawar, “Hadron Resonance Gas EoS and the Fluidity of Matter Produced in HIC”, Advances in High Energy Physics, vol. 2019, Article ID 6795041, 11 pages, 2019

[71] V. Vovchenko, H. Stoecker, “Thermal-FIST,” https://github.com/vlvovch/Thermal-FIST, 2022

[72] F. Flor, G. Olinger, R. Bellwied “Flavour and energy dependence of chemical freeze-out temperatures in relativistic heavy ion collisions from RHIC-BES to LHC energies,” Physics Letters B Volume 814, 10 March 2021, 136098

[73] G. Ranucci, “The profile likelihood ratio and the look elsewhere effect in high energy physics”, Nuclear Instruments and Methods in Physics Research Section A: Accelerators, Spectrometers, Detectors and Associated Equipment, Volume 661, Issue 1, Pages 77-85, 2012

[74] L. Moneta, “StandardHypoTestInvDemo.C File Reference,” https://root.cern.ch/doc/v608/StandardHypoTestInvDemo_8C.html, 2022